The Dissertation Committee for Mignon Denise Fitzpatrick
Certifies that this is the approved version of the following dissertation:

Investigating Sociomicrobiology by Integrating Micro 3D Printing with Quantitative Analytical Techniques

Committee:

Jason B. Shear, Supervisor

Jennifer S. Brodbelt

Sean T. Roberts

Eric V. Anslyn

David W. Hoffman

Investigating Sociomicrobiology by Integrating Micro 3D Printing with Quantitative Analytical Techniques

by

Mignon Denise Fitzpatrick

Dissertation

Presented to the Faculty of the Graduate School
of the University of Texas at Austin
in Partial Fulfillment
of the Requirements
for the Degree of

Doctor of Philosophy

The University of Texas at Austin
December 2018

Dedication

I would like to dedicate this dissertation to Ann Crane, who taught me French, patience, perseverance, and is still trying to hammer self-worth into my head. She is an epic human being, and an inspiration.

Acknowledgements

First, I would like to thank my advisor, Dr. Jason Shear, for allowing me to complete the work necessary to earn this Ph.D. in Chemistry. Secondly, I would like to thank my committee members, Drs. Jenny Brodbelt, Sean Roberts, Eric Anslyn and David Hoffman. Thank you to all the Shear lab members past and present, who have contributed directly to my success in this endeavor. In particular, I'd like to thank Drs. Eric Ritschdorff and Jodi Connell for their guidance, and Allison Myers for all her help and friendship, without which this dissertation would not have been able to be completed. Thank you also to Dr. Janine Elliott and Olja Simoska for their help with Project Beam a Laser through the Wall, and for all of Olja's help with setting up the new lab optical tables. In addition, I'd like to thank Tim Hooper for his constant support and contribution to keeping our instrumentation running and our sanity intact. Thank you also to Dwight Romanovicz, Julie Hayes, and Anna Webb in the core facility for all their help and patience. I'd also like to thank Steven Moore for helping us keep the lab from falling apart and Cory Konieczny for doing the same, in addition to helping us complete the enormously challenging building move. Thank you to Betsy Hamblen, and my therapist Dr. Bradbury, for their kindness and support. Finally, thank you to all my friends and family, especially my parents who have been here though it all, Michael and Maureen Fitzpatrick.

Investigating Sociomicrobiology by Integrating Micro 3D Printing with Quantitative Analytical Techniques

by

Mignon Denise Fitzpatrick, Ph.D.
The University of Texas at Austin, 2018

SUPERVISOR: Jason B. Shear

Antibiotic resistant polymicrobial infections have become a source of great concern in recent years both in clinical settings as well as in basic and medical research. Incidence of resistance and increased virulence, which typically emerge within small, dense cellular ensembles on picoliter scales, is on the rise and scientists are just beginning to understand the complexity of these dangerous bacterial populations. To that end, the research in this dissertation has sought to analyze the complex social interactions of micro 3D (μ3D) printed bacterial colonies with a variety of analytical techniques. Through characterization of the μ3D printed hydrogels themselves, and by pairing this technology with fluorescence and confocal microscopy, electrochemical studies, and mass spectrometry, important insights regarding the sociomicrobiology of these bacterial communities emerge. The Shear lab has previously employed μ3D printing of bacterial aggregates to study microbial populations in environments that reproduce attributes associated with complex spatiotemporal *in vivo* conditions to a much greater extent than

traditional culture techniques. Combining this technology with advanced imaging approaches has enabled a detailed investigation into properties of intra- and inter-species cooperation, including factors that influence antibiotic resistance and virulence. The goal of the work presented here is to integrate quantitative and qualitative analytical techniques with μ3D printing technology to enable novel approaches for studying interactions, both within and between small bacterial aggregates in complex microbial environments. This information will be vital in the next steps toward designing better and more efficient strategies for combatting complex pathogenic communities that exist within polymicrobial infection environments.

Table of Contents

List of Tables

List of Figures

Chapter 1: Introduction

Incidence of multi-drug resistant polymicrobial infections is on the rise. Cases that could previously be treated with one or multiple types of antibiotics are becoming much more difficult to cure. Many of these cases involve patients with lowered immune systems, such as those affected by cystic fibrosis, or those with the types of chronic wounds commonly found in diabetics and burn victims [1]–[3]. Within these infection environments, scientists have found that bacteria tend to self-organize into small, dense, complex social communities called *biofilms* that work together as a whole to create an effect greater than the sum of its parts. These biofilms can range in size from hundreds of thousands of cells encased in a polysaccharide matrix to less than a hundred, and frequently these aggregates can have a great impact on various stages of a bacterial infection [4]–[7]. In addition, different species frequently exist in such aggregates within an infection site, either concurrently or in a stepwise progression [8]–[10]. Microbial interactions, both within, and between species, can be modulated by direct cell to cell contact, chemical signaling such as quorum sensing (QS), and a host of other factors [11]–[14]. Historically, studying inter- and intra-aggregate communication has been difficult in an *in vitro* environment, due to the lack of ability to control spatial organization and replicate typical colony sizes and densities found *in vivo* [15].

With the development of micro three dimensional (μ3D) printing of hydrogels, it has become possible to create physically confining but chemically permeable structures of arbitrary shape on the microscale, such as those shown in Figure 1.1[16]–[18]. These structures can be fabricated within seconds around a particular single cell of interest, creating monoclonal populations of defined sizes, at densities much higher than those observed in plate and flask culture, and that mimic *in vivo* aggregate characteristics more

effectively. It has already been shown that small populations trapped within these biocompatible structures can be used to study antibiotic resistance, cellular communication, biogeography within a colony, and various other attributes that emerge on microscopic scales [19]–[22].

Moving forward, it is necessary not only to expand the applications of analytical tools employed in these studies, but to also further our understanding of the attributes of the printed structures themselves in order to more appropriately tailor their properties to meet the requirements of specific problem sets. Employing techniques such as fluorescence and confocal microscopy, electrochemistry, and mass spectrometry can yield important insights about the sociomicrobiology and biogeography of these aggregates within infection sites. In addition, analyzing hydrogel precursor solutions and physical properties of resultant structures (e.g. characteristics such as melting point and pore size) will enable the development of environments that better model those encountered *in vivo*. Thus, the work presented in this dissertation reflects a contribution to the characterization of the hydrogel structures, and an investigation into the social interactions of the cells contained within them, in an effort to further understand the complex nature of bacterial communities.

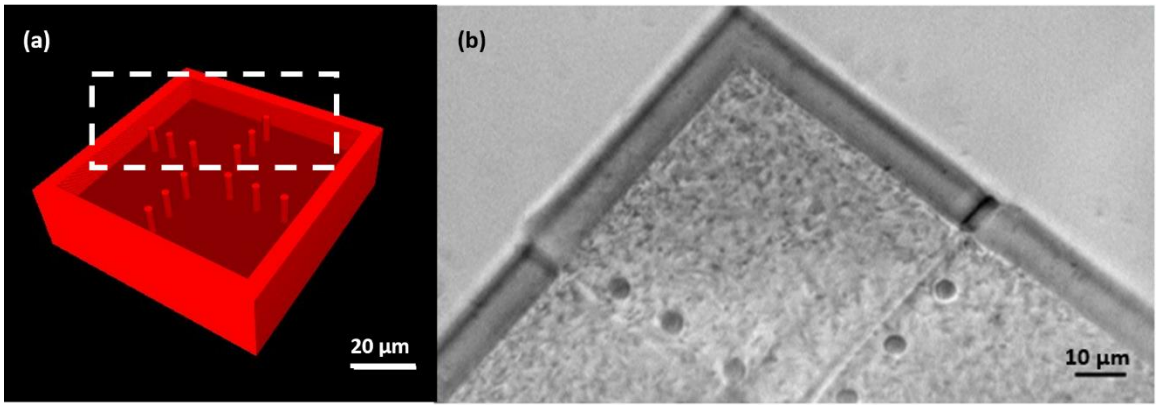

Figure 1.1: µ3D structure (a) rendered as a 3D model (without roof) and (b) printed as a protein structure filled with bacteria (bright field image). White dashed line indicates the portion of the model corresponding to the bright field image.

SOCIOMICROBIOLOGY

Bacteria are social organisms that develop intricately connected communities using a complex network of social cues [9], [11], [13], [14]. A primary means of communication used by various gram negative microbes, such as *Pseudomonas aeruginosa*, is a type of extracellular signaling known as quorum sensing (QS) [12], [23]–[26]. In QS, various small diffusible molecules called *autoinducers*, are produced constitutively by cells, which can diffuse across the membrane of the cells from which they are released, as well as those of nearby cells. Many bacterial genes require threshold levels of these signals in order to be transcribed. Autoinduction loops arise when the cell density rises to a level sufficient for a critical density to be reached with respect to the concentration of signaling molecules within the local environment. This causes a spike in production of QS molecules, which further increases extracellular concentrations[23]. The effects of this process are key to aggregation, attachment and the development of biofilms and bacterial communities[23], [27]. In addition, they are responsible for changes in gene expression which can lead to cooperative effects within the colony that result in increased antibiotic resistance and

virulence within a population[28], [29]. Figure 1.2 (a) illustrates the activation of an autoinduction feedback loop, resulting in changes in genetic expression (yellow to green) upon reaching a threshold density. In addition, the increasing cell density itself often serves to mediate cooperative activity based on cell to cell contact which can similarly affect phenotype, as shown in Figure 1.2 (b).

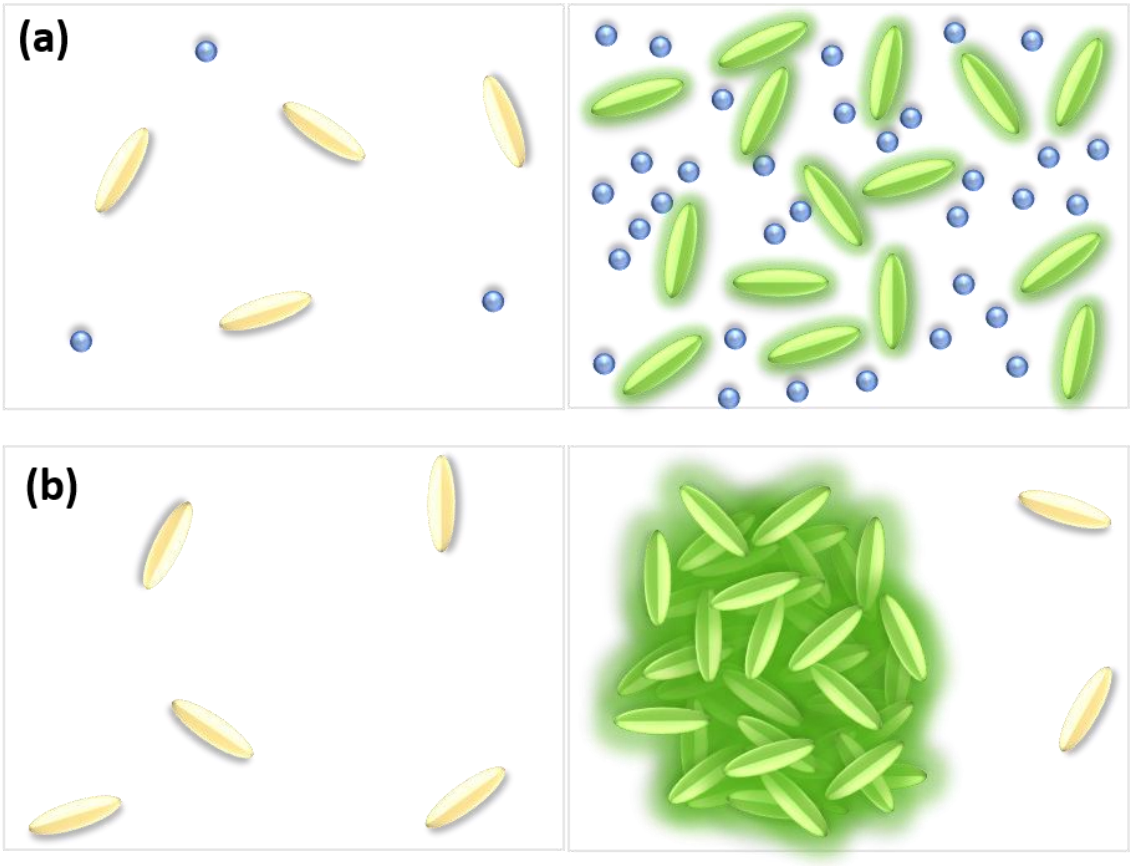

Figure 1.2: Bacterial communication, and subsequent change in gene expression, is mediated through the release and uptake of chemical signals (a) and direct contact with other cells (b). Blue dots represent QS molecules, while yellow cells in all panels represent planktonic, or unassociated, cells which are non-cooperative. Green cells in all panels indicate that either chemical signaling (a) or physical cues (b) have initiated a change in genetic expression associated with cooperation as a unit.

Factors contributing to spatial organization and biogeography within cooperating microcolonies such as density can vary across populations and species [10], [30], [31]. *P. aeruginosa* tends to form distributed small dense aggregates in environments such as the sputum excreted by the lungs of cystic fibrosis patients, Figure 1.3 (a) [32], [33]. Polymicrobial communities can also self-organize, such as the cooperative layers of *Snodgrassella alvi* and *Gilliamella apicola*, in which *Gilliamella* can only establish on the wall of the bee ileum if a micrometer thick layer of *Snodgrassella* is already present, Figure 1.3 (b) [34].

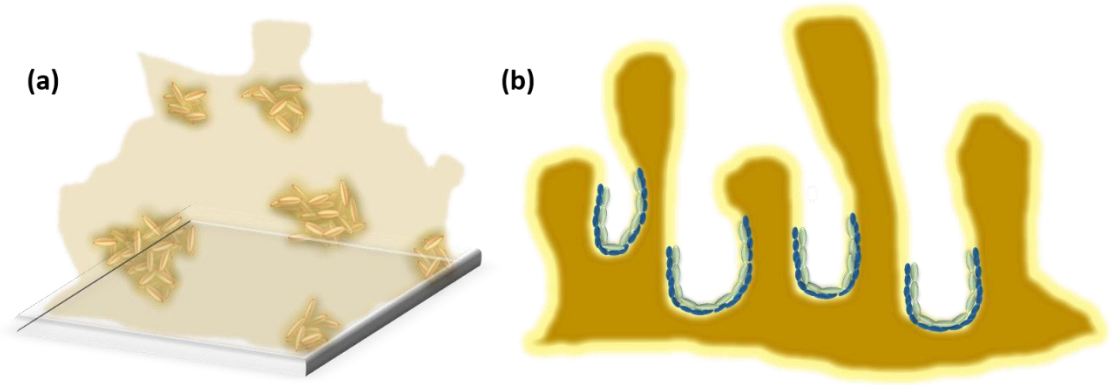

Figure 1.3: Spatial organization is important for both single species and polymicrobial growth. *Pseudomonas aeruginosa* (yellow) organizes into small dense aggregates in sputum (beige) (a), while *Snodgrassella alvi* (blue) and *Gilliamella apicola* (green) form characteristic layers in the ileum portion of the bee gut (yellow) (b).

Human Pathogens and *Pseudomonas aeruginosa*

P. aeruginosa is an opportunistic pathogen in nosocomial environments that commonly attacks immune-suppressed individuals, resulting in severe and persistent infections resistant to multidrug treatment [1], [6]. As discussed above, these cells tend to form dense aggregates surrounded by extracellular matrix in biofilms, where phenotypic

changes such as QS and physical isolation protect the cells from attack by a host's immune system and the action of antibiotics [6], [29]. In *P. aeruginosa*, QS pathways include those regulated by acyl homoserine lactones (AHLs), and one regulated by 2-heptyl-3-hydroxy-4-quinolone commonly known as PQS (*Pseudomonas* quinolone signal). Together, these systems work to aid in biofilm formation and increase bacterial virulence, manifested by changes in motility, the production of proteases, and toxins such as pyocyanin[24], [35], [36]. Thus, these communication systems are often key targets for the development of new therapeutic treatments [37], [38]. Disrupting the development of biofilms, aggregates and the social networks they create is an important goal for researchers[39], [40]. To achieve this, characterization of these microenvironments is necessary to lay out the next steps moving forward towards eliminating these pathogens, and due to its prevalence and virulence in various infection environments, *Pseudomonas aeruginosa* serves as a model pathogen in this endeavor. Combined with the power of μ3D printing of biocompatible hydrogels, a platform now exists to study these interactions in greater detail.

Unculturable Bacteria and *Vibrio fischeri*

Estimates have been made that approximately 10^8 bacterial species exist worldwide; unfortunately less than 2% of these species can be cultured using traditional flask and plate techniques [41]. The remainder are often referred to as “unculturable” bacteria. In recent years, researchers have endeavored to begin identifying unknown species through genetic amplification techniques like polymerase chain reaction (PCR) combined with analysis of the 16s ribosomal RNA, which can give clues about phylogeny and relationships between species [42]–[44]. However, to take advantage of these techniques, a certain amount of cellular material, commonly approximately 10^2 cells, must be present in order to accurately amplify the sequence. “Unculturable” cells, while

metabolically active, frequently do not divide at all in traditional batch culture, and confidently isolating 100 individuals of the same microbial species is, at best, tedious and impractical, and often simply not possible [41], [45]. Thus, a strategy to isolate single cells and *reintroduce their native environment to them* in a culture environment might, in some instances, provide a practical alternative. In this way, cells could be surrounded by other species fundamental to their own environment, along with all the nutrients, cues, and other factors necessary for their growth and reproduction.

One type of setting that is commonly investigated with respect to unculturables is the marine environment [42]. If a single cell could be isolated, trapped, and have the native seawater from which is was procured provided for its growth, it is possible that it might be able to reproduce, to provide sufficient genetic material for sequencing. Towards this goal, the model marine organism *Vibrio fischeri* can be used to determine how to apply the technique of μ3D printing to these unculturable microbes in the ocean [46]. While *V. fischeri* is readily culturable in a laboratory setting, the general requirements it has for growth as a marine microbe mimic those necessary for potential unculturable bacteria in oceanic environments. This makes it a preferred choice for investigating the application of the μ3D platform to this problem.

MULTIPHOTON EXCITATION AND μ3D PRINTING

The Shear Lab pioneered a μ3D printing technique based on the use of digital micromirror devices (DMDs) as dynamic intensity masks for direct-write, multiphoton lithography [16], [18]. In this approach, three-dimensionally localized, multiphoton excitation of a photosensitizer results in production of radicals or singlet oxygen that initiate intermolecular crosslinking of proteins [47]–[49]. By translating the focus of a laser

through a protein-photosensitizer reagent, 3D structures can be fabricated composed of a crosslinked protein matrix [50].

In most instances, molecular electronic excitation requires that the energy of an incident photon equals the spacing of electronic energy levels. However, in 1931 Maria Goeppert Mayer proposed that, in principle, an energy gap could be bridged, non-resonantly, by the near simultaneous absorption of two photons of lesser energy whose combined energy equaled that necessary to promote the transition of a single electron. Her prediction was later born out with the advent of high-intensity laser sources [51], [52]. In this process, absorption of the two photons is nearly simultaneous, often described as a first photon promoting a molecule to a "virtual state" (as in Raman spectroscopy), with a second photon interacting to complete the two-photon absorption event before the (femtosecond) decay of the virtual state. Such a process requires an extremely high photon flux, and thus extremely high intensities, according to the following set of equations, which represent two photon excitation in the form of a reaction scheme shown in Equation 1.1 [52]:

$$M + n(h\nu) \leftrightarrow M^* \qquad [1.1]$$

Here, M is the chromophore, M^* the excited chromophore, $h\nu$ is the photon, and n is the number of absorbed photons required to bridge the gap to the excited state. Building upon this reaction, a "rate" equation, Equation 1.2, can be written in which k is the rate constant, I is the instantaneous intensity of the excitation source (in units of photons s^{-1} cm^{-2}), and δ is the excitation cross-section (in units of $cm^{2n}(s/photon)^{n-1}$):

$$\frac{dM^*}{dt} = k\,[h\nu]^n[M] \;=\; \delta I^n[M] \qquad [1.2]$$

This results in linear scaling of one photon excitation, Equations 1.3 and 1.4, while two photon excitation scales as a power of n, Equations 1.5 and 1.6, shown below:

$$M + 1(h\nu) \leftrightarrow M^{*} \quad [1.3]$$

$$\frac{dM^{*}}{dt} \propto I \quad [1.4]$$

$$M + n(h\nu) \leftrightarrow M^{n} \quad [1.5]$$

$$\frac{dM^{*}}{dt} \propto I^{n} \quad [1.6]$$

To increase the probability of near-simultaneous absorption of multiple photons, a low-duty-cycle femtosecond pulsed laser can be used to constrain the photons within discrete temporal packets that are tightly focused using a high numerical objective. Using such an approach, it is possible to attain intensities sufficient to achieve reasonable rates of two-photon excitation within a three dimensionally constrained volume of approximately ~1 μm^3. Combining high quality optics (NA>1.0) and a near infrared femtosecond pulsed titanium:sapphire laser that has a duty cycle of ~10^{-5} (~10^{-13} s pulses produced approximately once every 10^{-8} s), it is possible to achieve peak laser intensities of ~10^{11} W cm^{-2} within the focal volume using an average power output of only 10 mW [18], [21], [53].

Figure 1.4 (a) and (b) illustrate the Jablonski diagrams for one photon and two photon excitation, respectively, and are accompanied by schematic representations showing localization of excitation for each case.

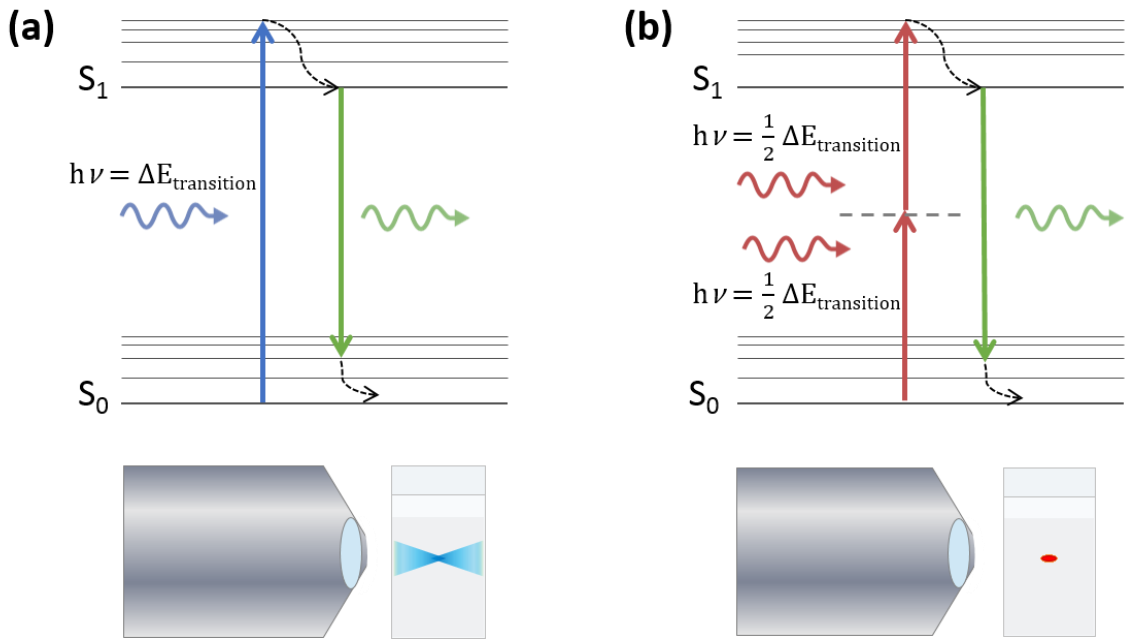

Figure 1.4: Jablonski diagrams (top) of single photon (a) and two photon (b) excitation and emission, accompanied by a visual representation of the focal volume of excitation in chromophore solutions for each (bottom).

Multiphoton lithography relies on this ability to localize reaction volumes to the microscale. Confining these processes to such a small volume allows for the precise control necessary to fabricate defined structures with submicron features that enable the study of cellular interactions. While multiphoton lithography has been shown to be applicable in the creation of various polymeric 3D objects using a range of synthetic reagents, the Shear lab has focused a great deal of attention on its application to the μ3D printing of protein hydrogels; a diagram of the optical table arrangement used for these processes is presented in Figure 1.5 [20], [21], [50]. Creating these structures, as mentioned previously, requires two-photon absorption of a photosensitizer within an aqueous protein solution. These localized activation events produce highly localized volumes of concentrated radicals or singlet oxygen, which in turn can initiate crosslinking events between side chains on

adjacent proteins, forming a protein matrix from a liquid solution. Here, a set of mirrors raster scans the focused beam across the surface of a DMD dynamic mask, which is positioned in a plane conjugate to the fabrication plane. The exposure pattern within the fabrication plane is determined by a binary image transmitted to the DMD by a computer. It is possible to synchronize changes in the mask displayed by the DMD with stepping the position of the reagent relative to the laser focus (along the optical axis dimension) to create a true 3D structure of arbitrary design. Another advantage of this technique is that these structures can be created around a bacterium in solution, simply by introducing cells to the hydrogel precursor solution beforehand. This enables the "trapping" of cells in order to create monoclonal colonies with densities and spatial organizations similar to those found *in vivo* [20].

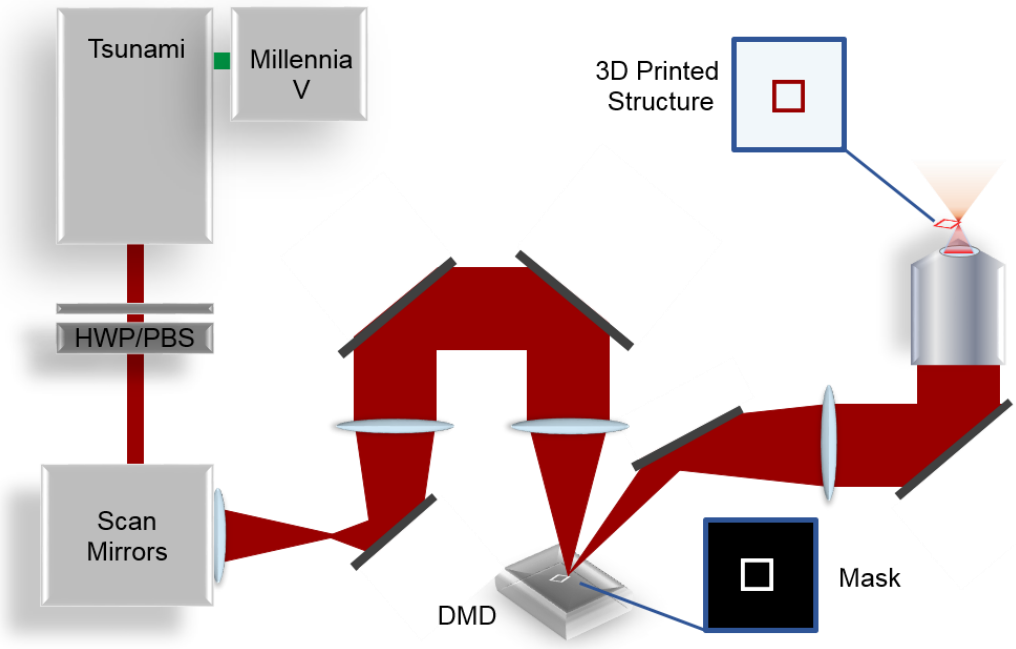

Figure 1.5: Schematic of the setup used in the Shear lab for µ3D printing of hydrogels. The Millennia Nd:YVO_4 laser pumps the Tsunami titanium:sapphire femtosecond oscillator, and the power is attenuated using a half wave plate/polarizing beam splitter (HWP/PBS) pair. The beam then passes through the scan mirrors, where it is raster scanned and focused onto the surface of a digital micromirror device (DMD) displaying a dynamic mask image, in this case a square with an empty interior. The white pixels cause the corresponding mirrors to further light along the optical path and into the objective where the laser is then scanned across the surface of the plane, creating a hydrogel cross-linked protein matrix. Because the DMD is positioned in a plane conjugate to the fabrication plane, the pattern displayed on the DMD is reproduced as a fabricated object. After fabrication in a given plane, the reagent is stepped along the optical (z) axis as new masks are displayed to create an intact 3D structure in a plane-by-plane fashion.

FLUORESCENCE AND CONFOCAL MICROSCOPY

The first tool ever used in identifying bacterial populations was microscopy, and still today it is one of the most common tools used in both identification and analysis of

microbial populations [54], [55]. While bright field imaging allows for examining features and identification via staining, modern techniques of genetic editing of bacterial genomes, such as the addition of gene expression reporters like green fluorescent protein (GFP), have taken advantage of various fluorescence-based approaches [56]. Wide-field fluorescence microscopy and laser scanning confocal fluorescence microscopy both are used to provide important insights into how bacterial populations grow, change, organize, and cause infections, and thus have become extremely popular in microbial analyses [57].

Fluorescence Microscopy

Fluorescence emission occurs when a chromophore absorbs a photon equal in energy to the gap between the ground and excited states of a particular electron within said chromophore, and then the electron returns to the ground state, emitting another photon. Due to vibrational relaxation in the excited and ground singlet states (and typically solvent re-orientation), this second photon is typically lower in energy than that of the incident photon, as shown in the Jablonski diagram shown in Figure 1.4 (a) [58]. Accordingly, fluorescence microscopes produce low-background fluorescence images by differentially filtering excitation and emission wavelengths [59]. For example, Figure 1.6 (a) shows a block diagram in which the excitation source, a mercury lamp providing a broad spectrum of visible wavelengths, is filtered to produce a single narrow wavelength window for excitation, indicated in blue. The dichroic mirror reflects the appropriate wavelengths downward to the objective and the specimen. When this blue light excites electrons within chromophores in the sample, wavelengths in both the green and yellow portions of the spectrum are emitted, and they are allowed to be transmitted through the dichroic. An emission filter before the pinhole blocks any radiation from the excitation source and ensures only wavelengths in the green portion of the spectrum reach the detector. These

filters can be extremely specific, allowing for a range of only tens of nanometers to pass through. Such specificity can be tremendously useful in microbiological applications, as it allows multiple chromophore "reporters" to be combined on single plasmids that are subsequently integrated into the genome. For example, a plasmid could be introduced that allows a bacterium to constitutively produce mCherry (a red fluorescent protein), while expressing GFP under only a specific set of conditions dictated by genetic expression of a specific protein [57], [60]. An example of cellular fluorescence from GFP excitation using a 488 nm excitation source paired with an emission filter centered on 509 nm is shown in Figure 1.6 (b).

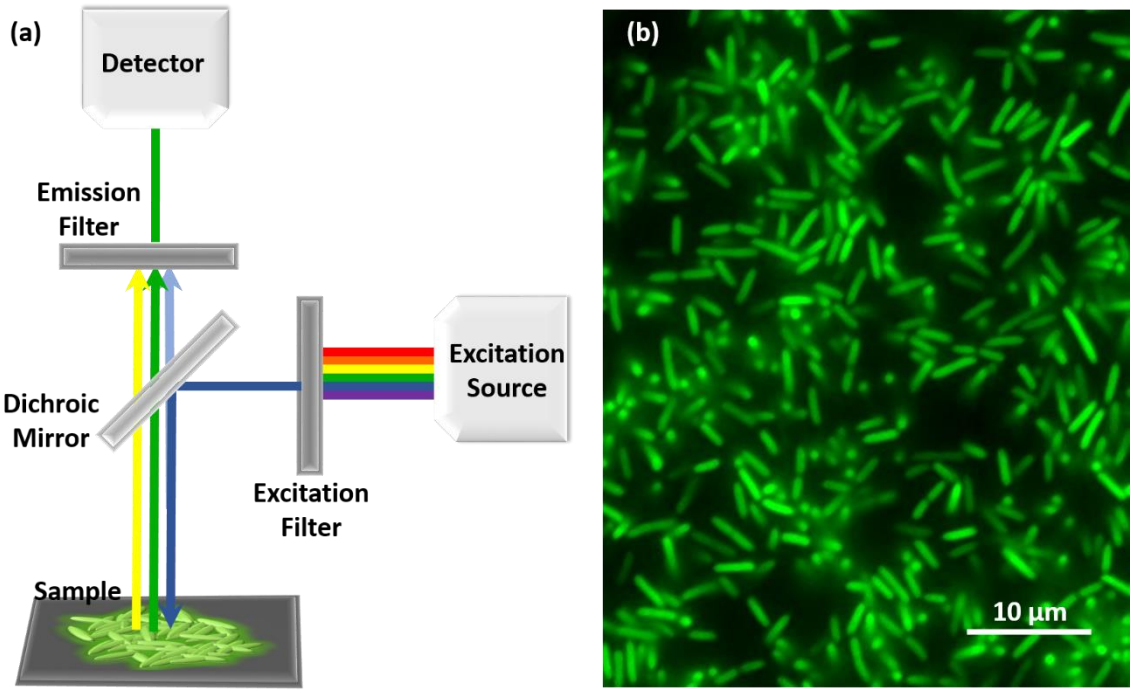

Figure 1.6: Block diagram of an upright fluorescence microscope (a) and a fluorescence image of *Pseudomonas aeruginosa* expressing green fluorescent protein (b).

Laser Scanning Confocal Microscopy

Laser scanning confocal microscopy (LSCM) uses the general principles of fluorescence microscopy with a few key added components that greatly improve imaging of three dimensional specimens, such as those found in biological samples [57], [61]. Most importantly, this approach provides the ability to eliminate out of focus light or flare using spatial filtering, which can prevent scattering and secondary fluorescence in planes outside the focal plane from interfering with imaging. This is achieved by introducing a pinhole after the emission filter and before the detector. While the emission filter will let all light within a particular range of wavelengths pass, only the light gathered from the in focus plane can pass through the pinhole to the detector, as seen in Figure 1.7 (a). In addition, thick specimens can be imaged using a serial optical sectioning technique, in which the plane is scanned and then the beam focus is stepped in the z-axis, such that each subsequent plane provides only information from that plane due to the pinhole. Finally, because LSCM uses a laser that is focused and then scanned across the surface as opposed to wide field fluorescence, it illuminates only one position in the x-y plane at a time, decreasing the likelihood of collecting spatially distorted signal. Together, these attributes make LSCM a powerful tool for the study of cells, which are often arranged in three dimensional communities (for example, in bacterial aggregates, tissue slices, etc.) [56], [61]–[63]. Figure 1.7 (b) displays a three dimensional projection of a stack of confocal images of *Pseudomonas aeruginosa* within a structure.

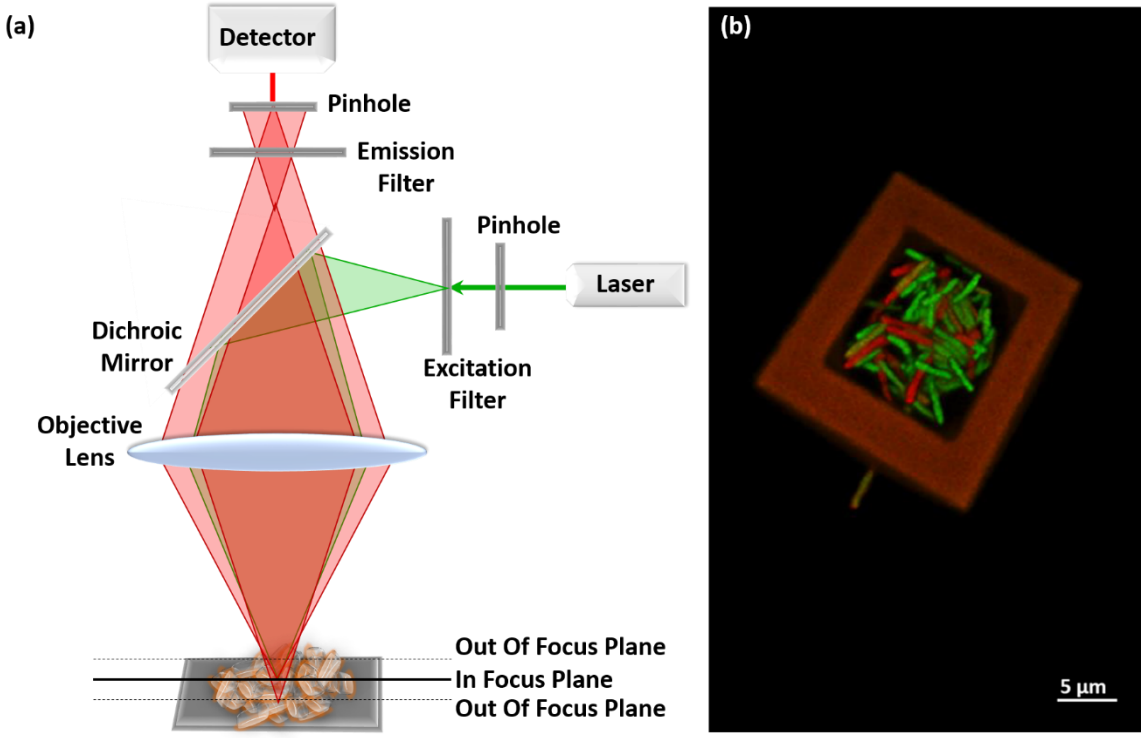

Figure 1.7: Block diagram of a confocal fluorescence microscope adapted from Olympus Microscopy Resource Center (a) and 3D projected stack of confocal images showing live *P. aeruginosa* expressing green fluorescent protein (green) and dead cells stained with propidium iodide (red), structure walls are indicated in reddish-orange (b).

ELECTROCHEMISTRY OF CELLS

As mentioned previously, cellular communication can rely heavily on the production and diffusion of chemical signaling molecules in the process known as quorum sensing. In addition, certain compounds and metabolites produced as a result of QS are important factors in increased virulence, cooperation between cells within a colony, and protection against host immune response and competing bacterial populations [29], [64]. One such product of QS in *P. aeruginosa* is pyocyanin, a toxin that can cause extensive damage to both competing species and host cells through oxidative processes [65]–[67]. Since it is a redox-active chemical, pyocyanin be detected using electrochemical methods

such as square wave voltammetry. The Stevenson lab has recently developed transparent carbon ultramicroelectrode arrays (T-CUAs) for detection of various cellular signaling molecules, including pyocyanin. Different from most electrodes, T-CUAs are optically transparent necessary for techniques such as fluorescence microscopy. [68], [69]. Figure 1.7 (a) displays the reversible redox half reaction of pyocyanin, while (b) and (c) display an example of how a calibration curve can be created from square wave response curves measured upon the addition of increasing amounts of pyocyanin.

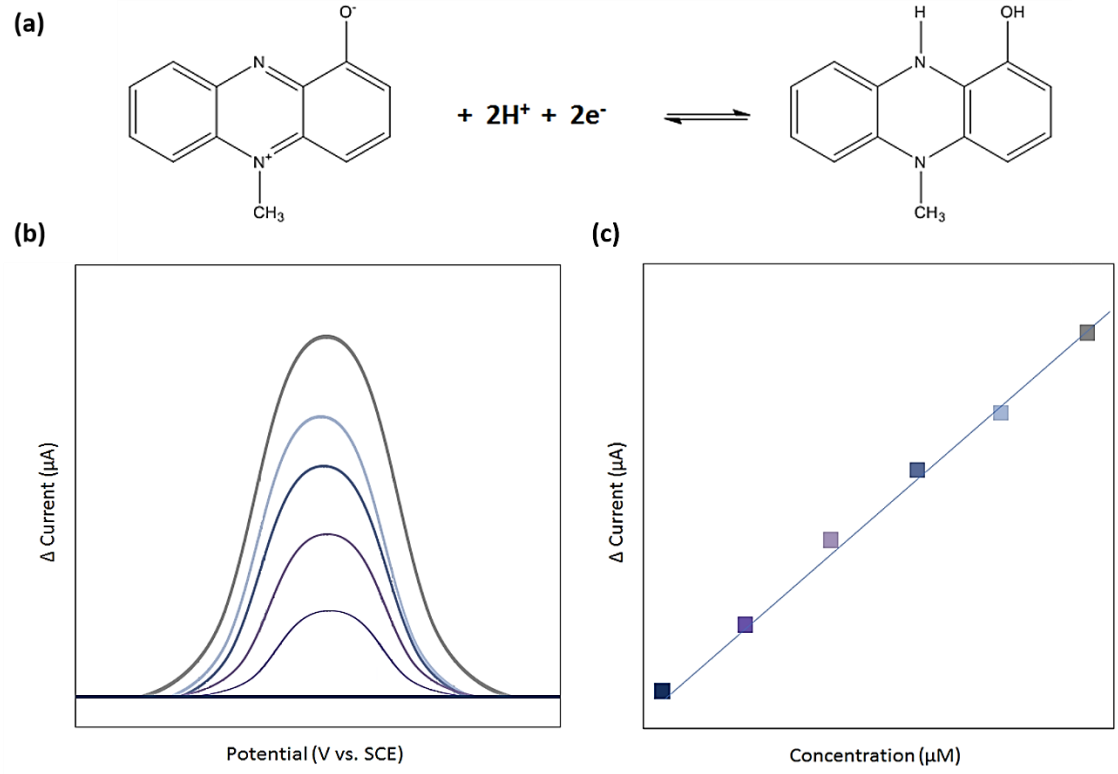

Figure 1.8: Pyocyanin reduction half reaction (a) and a generic square wave voltammogram displaying a set of response curves varying by concentration (b) and a generic calibration curve generated from the response curves (c).

MASS SPECTROMETRY

Mass spectrometry (MS) is an important tool utilized in many biological applications [70]–[72]. Not only can components in a heterogeneous mixture be separated and identified, but their relative abundances can be quantified as well. Separation techniques such as high performance liquid chromatography (HPLC) and gas chromatography (GC) can be coupled with mass spectrometry to analyze highly complex samples [73]. Tandem mass spectrometry (MS-MS) can provide even more details about the molecular structure of each component [74]. Consequently, in recent years, mass spectrometry has been able to provide important details about protein sequences, structural information, spatial distributions within a sample and other key data that improve our understanding of complex molecules [75]–[80]. For this reason, MS has become an increasingly useful tool in the study of microbiological systems, where it has been used to analyze a range of cellular byproducts, components, and interactions [72], [80], [81]. Figure 1.9 illustrates a block diagram of a typical mass spectrometer, wherein the sample is introduced through the inlet into a vacuum chamber, where it is ionized by a particular type of ionization source such as electron ionization or chemical ionization, then analyzed in a mass analyzer such as a quadrupole or an orbitrap, and then detected before the information is passed to a data output system.

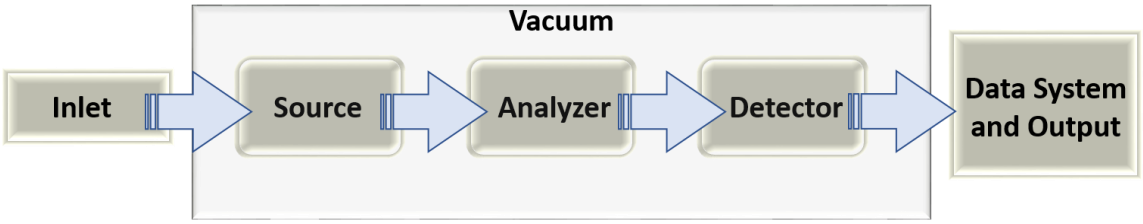

Figure 1.9: Block diagram of the components of a generic mass spectrometer.

Ultraviolet Photodissociation (UVPD)-MS

UVPD is a type of tandem mass spectrometry developed by the Brodbelt lab which allows for top down analyses of macromolecules such as lipids, nucleic acids, proteins and protein complexes [77], [82]–[84]. This process involves irradiating ions that have been produced by the primary ion source with ultraviolet (UV) photons while they are inside the mass spectrometer. This imparts a high level of energy to the ions, resulting in the cleavage of a large number of bonds creating many more fragmentation sites than would typically be seen with conventional collisional induced dissociation (CID) methods. This process not only results in a more detailed MS/MS spectrum but these fragment ions can also be used to piece together the structure of the analyte molecules [85]. The addition of multiple mass analyzers in conjunction with UVPD, such as with the Lumos system illustrated in Figure 1.10, produces a powerful tool that can give information about bacterial membrane components and to potentially provide insights into how those components can be specifically targeted in the development of disruptive therapeutics.

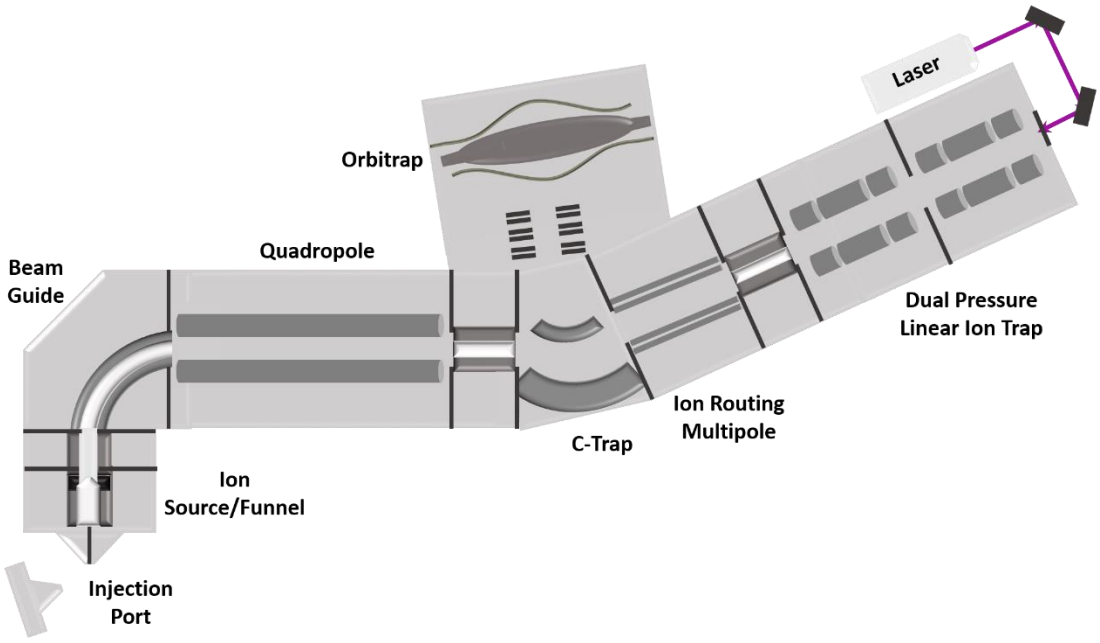

Figure 1.10: Block diagram of a Thermo Orbitrap Fusion Lumos Tribrid, adapted from the Thermo Fisher website, coupled to a UVPD laser. Samples are injected at the injection port before being ionized in the funnel, guided into the first mass analyzer, the quadrupole mass filter, and subsequently being directed into the ion routing multipole before being subjected to the orbitrap mass analyzer or the linear ion trap mass analyzer. UVPD of the ions occurs in the ion trap portion of the instrument.

Desorption Electrospray Ionization (DESI)-MS

DESI is considered an ambient ionization technique for preparing samples for mass spectrometry [86], [87]. While most samples are injected into the mass spectrometer and ionized under vacuum, as seen in Figure 1.9, DESI samples can be prepared on a slide and are ionized using an electrically charged solvent stream [88]. This produces a spray of charged sample ions that can be collected and transferred into the inlet of the mass spectrometer, as seen in Figure 1.11. This technique involves minimal sample preparation and can be performed on a wide array of native sample types, making it a preferred ionization source for many biological applications [89]–[91]. In addition, it provides an

excellent platform for MS imaging, as the stage containing the sample can be translated in the x-y plane, providing the ability to identify the specific spatial regions of a sample where particular analyte molecules reside. As a result, this technique has the potential to both identify extracellular signaling molecules while simultaneously mapping their relative location within a sample [72], [90], [92], [93].

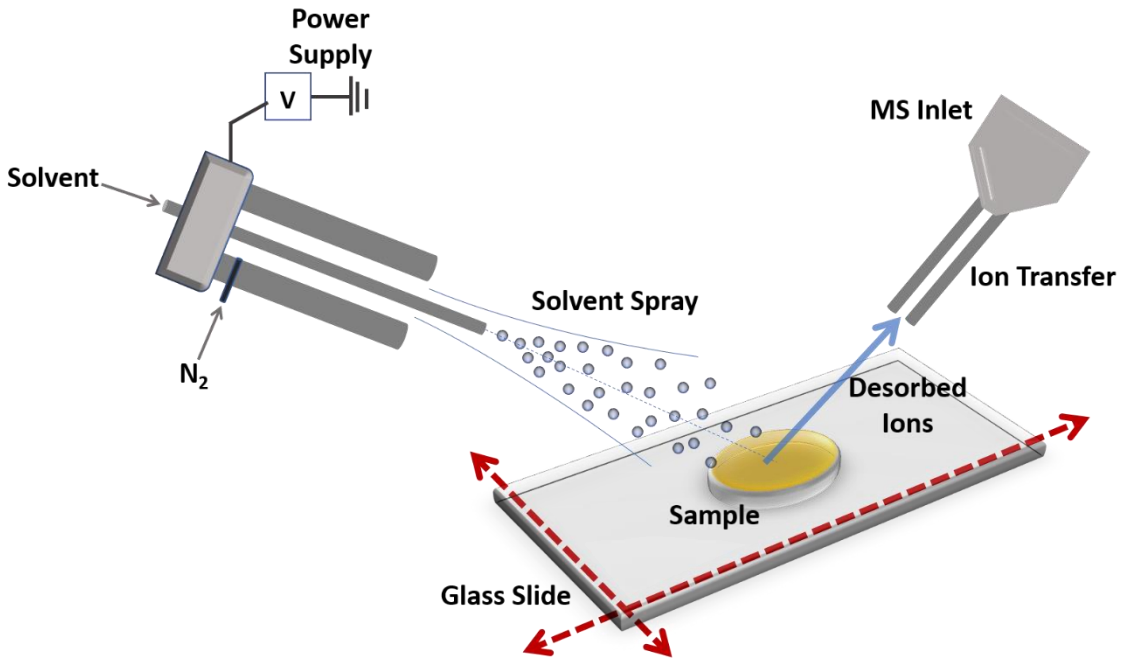

Figure 1.11: Diagram of a typical DESI-MS setup for extracellular molecule analysis. The solvent spray capillary remains immobile, while the glass slide translates on an open air stage in the x and y dimensions, as indicated by the red dashed arrows.

CONCLUSION

Understanding the complex sociomicrobiological and biogeographical components of bacterial populations is necessary in order to design new therapeutic treatments to interrupt the establishment of pathogenic colonies. Investigating both the communication

within and between bacterial communities, and determining their spatial organization with respect to one another can afford important insights into how to best face the challenges presented by multi-drug resistant infections. A key facet of this discovery process involves the application of quantitative analytical techniques in examining microbial communities that reflect *in vivo* populations with a high degree of fidelity. μ3D printing offers a bridge between *in vitro* and *in vivo* environments, by enabling precise spatial control, diffusivity of nutrients and waste products, and the ability to create protein hydrogel structures of arbitrary design.

The work presented in this dissertation applies a number of quantitative analytical techniques in the investigation of μ3D printed bacterial colonies to further our understanding of the complexities of microbial communication and cooperation. In addition, it involves the characterization of the hydrogel structures themselves, in order to determine key physical attributes such as porosity and melting temperature. These qualities are integral to the design of *in vitro* conditions that best represent environments encountered by pathogenic bacteria in infection sites. To this end, the following chapters address the technique of μ3D, the design of a platform for studying unculturable bacteria, characterization of solutions intended for μ3D of pathogenic bacteria such as *P. aeruginosa*, spatial organization studies, growth analyses done in collaboration with electrochemists, the application of DESI-MS to μ3D printed colonies, and cellular viability experiments done in collaboration with researchers in mass spectrometry.

Chapter 2: Micro 3D Printing and Optical Table Setup

INTRODUCTION

Multiphoton Excitation and μ3D Printing

As mentioned in Chapter 1, multiphoton excitation, particularly two photon excitation, is the fundamental basis for μ3D printing. The non-linear scaling of excitation with intensity allows for the extremely high photon flux necessary to achieve practical levels of multiphoton excitation events. Focusing the beam temporally, through the use of a high peak power near infrared (IR) femtosecond pulsed laser, such as a solid state titanium:sapphire oscillator, and spatially (e.g. to sub-micrometer beam waists), through the use of high numerical aperture (NA) objectives means planes nearest the focal point will have a much higher probability of supporting two photon events, especially if the chromophores have large two photon absorption cross sections. Within the ~1 μm^3 focal volume, or voxel, instantaneous intensities of ~10^{11} W cm^{-2} can be achieved with an average power of only 10 mW, given a typical 80 mHz repetition rate and a low duty cycle of ~10^{-5}. This combination of high instantaneous intensities, low average power, and very small focal volume is pivotal to the μ3D printing process. This allows the reaction to be confined to the specific regions in solution designated by the mask, and prevents excessive heating and energy scatter [17], [50]–[53], [94].

While two photon excitation has been used with a variety of substrates, including styrene, epoxy, and acrylate, the application to cell culture requires the use of more biocompatible components, such as proteins [50], [95]–[97]. In order to create a solid μ3D printed microstructure from a liquid protein solution, numerous inter-molecular crosslinking events must occur between side chains of amino acid residues on adjacent proteins within the solution. While this can happen naturally in certain photo-oxidizable

residues like tyrosines and histidines under ultraviolet light exposure, using a photosensitizer allows for highly efficient two photon laser light absorption, producing a host of radical species or singlet oxygen to facilitate crosslinking [47], [49]. Rose bengal for example, is a photoinitiator can convert absorbed light energy into chemical energy, via either Type I or Type II reactions following two photon excitation. It will either be involved in a hydrogen abstraction event, producing radicals that then initiate crosslinking (Type I) or the production of singlet oxygen (Type II) with similar results [47]. Various types of photosensitizers are available depending on the application, taking into consideration phototoxicity, cytotoxicity, laser wavelength, optical transparency, efficiency, etc. In addition, various proteins can be used in the crosslinking process, including but not limited to bovine serum albumin, lysozyme, apomyoglobin, and gelatin [98]. Gelatin affords the added benefit of producing a solid or semi-solid "gelled" reagent at room temperature, allowing motile cells to be immobilized and thus able to be trapped without complex guidance-based methods [20]. It also allows for the creation of unconstrained three dimensional architectures [17]. Regardless of the protein chosen, however, the basic principle remains the same. The photosensitizer is activated within the focal volume, producing either radicals or single oxygen species which in turn facilitate crosslinking between side chains of adjacent protein molecules.

Another fundamental aspect of the μ3D printing process is the concept of the "mask" and its relation to the digital micromirror device, or DMD [16], [18]. As the laser light is reflected along the table, the beam is scanned, creating a plane, using a set of galvo scanning mirrors. This plane is translated across the table until reaching the DMD, where the beam becomes focused, and the scan collimated. Similarly, in the focal plane of the sample, the beam is focused and the scan collimated, making them conjugate planes. This is integral to the mask based system. The DMD itself is a chip, located within a dismantled

projector, composed of an 800 x 600 array of individually addressable 16-μm x 16-μm aluminum mirrors that can be switched "on" or "off" by means of a ±10º tilt [99]. Binary images, or "masks" that can be facilely created using PowerPoint, ImageJ, or Adobe Photoshop containing black and white pixel array instructions can be sent to the DMD through the computer using the same video graphics array (VGA) cable frequently used as an interface between computers and projectors. The white pixels in the mask result in an "on" state of the mirrors on the chip, allowing laser light to continue along the optical path towards the sample, while the black pixels result in an "off" state, directing laser light away from the sample and into a beam block. One by one, new images can be presented to the DMD as the z-axis is stepped up in the sample via motorized focus driver attached to the microscope fine focus. Because the DMD is positioned in a plane conjugate to the fabrication plane (i.e., there is a one-to-one spatial correlation of points in the DMD plane with the fabrication plane), exposure patterns in the reagent correspond to display patterns on the DMD for each fabrication plane, resulting in crosslinking patterns that build a structure from the coverslip up with arbitrary, three-dimensional submicron resolution. This chapter will cover an investigation of the various components and their contribution to the finished protein hydrogel products that enable the analysis of cellular growth and communication on the microscale.

REAGENTS

Bovine serum albumin (BAH64-1639) was purchased from Equitech-Bio (Kerrville, TX). Gelatin Type A from porcine, 60 Bloom (16560) was acquired from Electron Microscopy Sciences (Hatfield, PA). Rose bengal disodium salt (R323-25) and was purchased from Fisher BioReagents (Fairlawn, NJ). BupH phosphate buffered saline packs (28372) were purchased from Thermo Scientific (Waltham, MA).

FABRICATION CONDITIONS

Hydrogel fabrication solutions were created by solubilizing rose bengal (RB) into phosphate buffered saline (PBS) at a concentration of 5 mM in a heated sonicator for one hour at 60 ºC. Bovine serum albumin (BSA) and 60 Bloom gelatin Type A from porcine (gel60) was then added to 500 µL of this solution in amounts sufficient to final concentrations of 40 mg mL^{-1} and 150 mg mL^{-1}, respectively. This was vortexed briefly in a 1.5 mL mini centrifuge tube and then placed in the oven at 60 ºC for thirty minutes and then vortexed again for a few seconds. The solution was then placed on a heated shaker at 37 ºC for three hours. Following this, a 30 µL droplet was pipetted onto a #1 borosilicate coverslip in a Teflon sample well and allowed to cool to ~20 ºC. Free-standing protein microstructures were then created using an Olympus UPlanApo 100x/1.35 NA objective (Tokyo, Japan) on an inverted Zeiss Axiovert 100 microscope (Oberkochen, Germany) using variable z-axis step sizes and laser powers. The well was then filled with PBS and returned to 37 ºC for 45 minutes, and then with fresh PBS before imaging. Details of the µ3D printing and parameters will be addressed in subsequent sections.

GENERAL OPTICAL TABLE SETUP AND COMPONENTS

The fundamental components of the optical table necessary for fabrication of the protein hydrogel microstructures include the femtosecond pulsed, near-IR tuned laser, complete with a pump source, followed by an external shutter allowing the beam access to the rest of the optical components, that is controlled by a computer program synced with the scan mirrors and DMD. Next, a means to attenuate power manually day to day, such as a combination of a half-wave plate and polarizing beam splitter is necessary, followed by the scan mirrors themselves, which translate the beam into a planar scan. The DMD follows, with the focused laser beam scanned across its surface as it displays the mask

presented by the computer. The mirrors are also controlled by the computer such that scans are synchronized with mask presentation. Finally, a microscope with high numerical aperture objectives to tightly focus the beam at the fabrication plane in solution is employed, equipped with a z-axis translation stage, and a charge coupled device (CCD) camera to monitor and record fabrication. As mentioned previously, a computer is also necessary to control and synchronize the various components of the shutter, scan, z-step, and imaging. Additional optical table components, such as the lenses and mirrors serve to translate the beam across the table, allowing the beam waist to be tightened, and for focusing and collimation as required.

Figure 2.1 illustrates the components used in the Shear lab for microfabrication, all of which are mounted on a table equipped with Newport Stabilizer laminar flow isolators. First, a Spectra Physics (Santa Clara, CA) titanium:sapphire Tsunami is pumped by a Spectra Physics Nd:YVO_4 Millenia Pro V and cooled by a Thermo (Waltham, MA) Neslab RTE-111 chiller. As the beam exits the Tsunami, it is reflected towards the rest of the optical components by M_1, the output mirror. (All table mirrors are Newport (Irvine, CA) Valumax near-IR broadband dielectric mirrors.) This beam is centered on a shutter controlled by a Uniblitz (Rochester, NY) VMM-D1 shutter driver. When the shutter is open, it passes through a Newport half wave plate, and is reflected by M_2 through an iris, for daily alignment, and centered onto a Thorlabs (Newton, NJ) polarizing beam splitter. A Melles Griot (Carlsbad, CA) 13PEM001 broadband power meter can be inserted and removed from the beam path at this point, and power can be attenuated as necessary on a daily basis by rotating the half wave plate. The reflected beam then passes through a pair of telescopic Newport lenses TL_1 and TL_2, meant to tighten the beam as it translates across the table. Each are equipped with irises and there is a separate iris in between to ensure proper alignment. The re-collimated beam is then reflected down into the Thorlabs

scanning galvo mirrors by M_3 through M_5. From here, L_1 focuses the beam and collimates the scan, L_2 collimates the beam and focuses the scan, M_6 through M_7 translate, and then L_3 focuses the beam onto the DMD (a component of a BenQ MP510 projector) and collimates the scan. Periscope mirrors P_1 and P_2 raise the beam height, and L_4 focuses the scan and collimates the beam. Finally, after being reflected up through the Zeiss Axiovert 135 (Oberkochen, Germany) microscope by a 99% reflective dichroic mirror, the Olympus (Shinjuku, Japan) UPlanApo NA 1.35 100X objective refocuses the beam and collimates the scan, causing the DMD and sample focus to be in conjugate planes. A Prior (Cambridge, United Kingdom) Proscan stage allows for the stage to be translated in the x and y dimensions. This stage also enables the sample to be raised up in stages, or steps, in the z-axis. This is achieved using the same National Instruments (Austin, TX) LabVIEW 2011 program that controls the scan mirrors, DMD and shutter. A Hamamatsu (Hamamatsu City, Japan) ORCA-Flash 8.2 CCD camera is mounted to the top of the microscope to monitor the fabrication process.

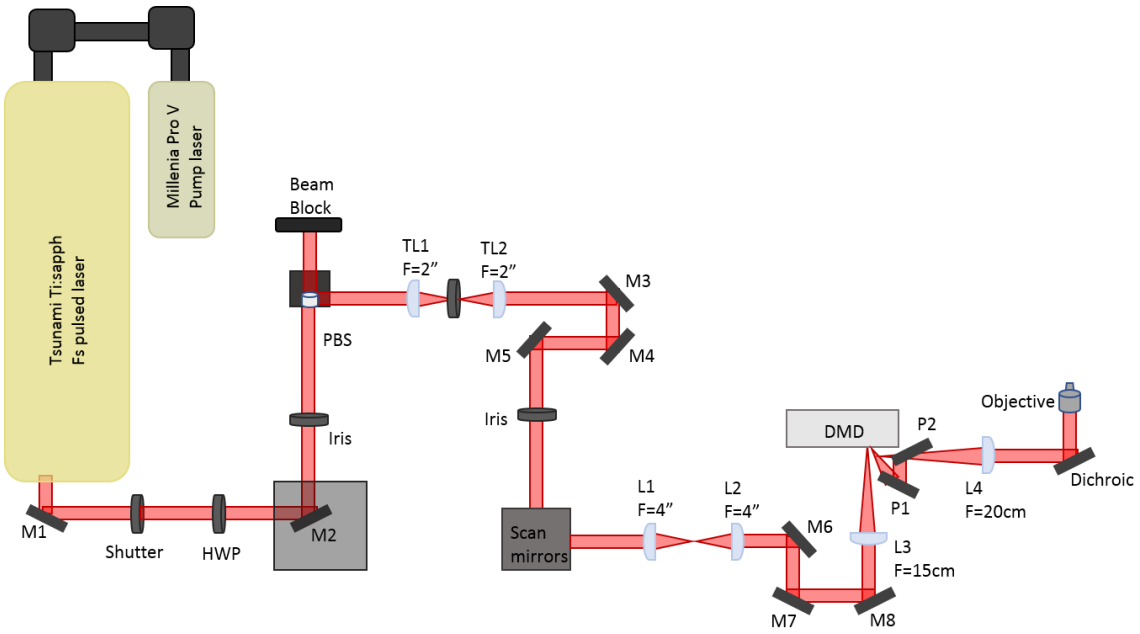

Figure 2.1: Diagram of the optical table setup used for µ3D printing.

IMPORTANCE OF COMPONENTS TO HYDROGEL MATERIAL FABRICATION

Having a properly functioning optical table is key to the construction of high integrity, structurally sound protein hydrogel products. There are numerous components of the table which, if malfunctioning, or functioning sub-optimally, can result in a host of problems at the fabrication level. For example, misalignment of the telescopic lenses prohibits µ3D printing completely, and the beam focus may not even be visible on the computer screen through the CCD camera. Another key issue that is frequently encountered is the DMD. The DMDs used in the Shear lab are micromirror arrays present within projectors, such as the BenQ MP510. Tim Hooper in Welch Hall has been consistently indispensable in his role of helping us to dismantle these projectors to reveal the chip within. However, revealing the chip to use it in the optical table setup also exposes it to laboratory elements such as dust, debris, and human contact. In addition, the laser power, while distributed across the surface during the scan, is extremely intense at the focus on

the surface of the DMD when the scan is not engaged. Failure to attenuate the power before daily alignment can burn or even melt portions of the chip. In addition, the projector model in use is 12 years old and out of production, requiring the purchase of used and refurbished units which may have electronic issues contributing to chip malfunction. However, as seen in Figure 2.2, it is absolutely necessary to maintain a properly functioning chip, as any aberration will be passed on to the conjugate plane during fabrication. The red arrow in Figure 2.2 (a) indicates a portion of a dome wall is out of focus and is no longer in contact with the coverslip, due to the mirrors on the portion of the DMD that corresponds with that area of the mask being damaged. Similarly, arrows in Figure 2.2 (b) reflect an analogous problem.

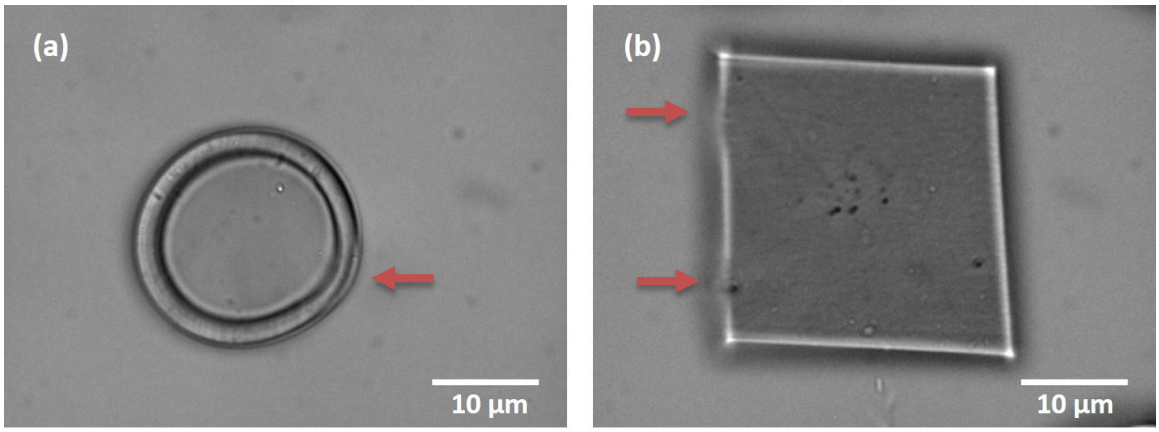

Figure 2.2: Bright field images of hydrogel structures fabricated with a DMD containing an aberration, a dome (a) and a large pad (b).

Figure 2.3 indicates the result of such aberrations in the fabrication process. In (a), the red arrows indicate areas of the domes which are no longer connected to the coverslip. After the fabrication process, any cells that might have still remained in the traps were allowed to grow for 4 hours at 37 °C. This gave time for the bacterial cells to multiply within and around the structures. A bright field image of this can be seen in Figure 2.3 (a)

Cells can be identified as the small fibrous looking elements in the image. Image (b) was taken directly after rinsing the structures shown in (a) a second time with a phosphate buffered saline solution following that growth period. The red arrows still indicate the "holes" in the bases of the domes, and it is clear that most of the cells both within and outside the structures have been rinsed away. This confirms that the aberrations have indeed caused openings at the bases of these structures, allowing cells to be pulled out during the rinsing process.

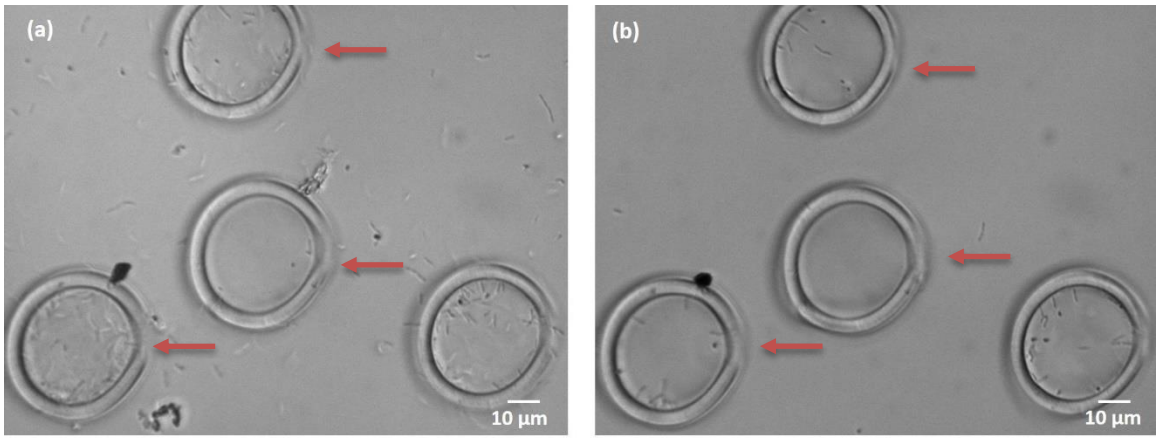

Figure 2.3: Bright field images of hydrogel domes fabricated with a DMD containing an aberration. Some cells can be seen following trapping inside the domes (a) and most have been removed following a rinse, due to poor structural integrity (b).

Finally, after replacement of the DMD with a newer, undamaged device, the resulting domes are structurally sound with no inconsistency in attachment to the coverslip, as evidenced by Figure 2.4. Both (a), the base, and (b), the roof, appear in focus across the length of the structure, indicating successful construction of the object. Subsequent tests performed involving cell capture did not result in a loss of cells post-rinse.

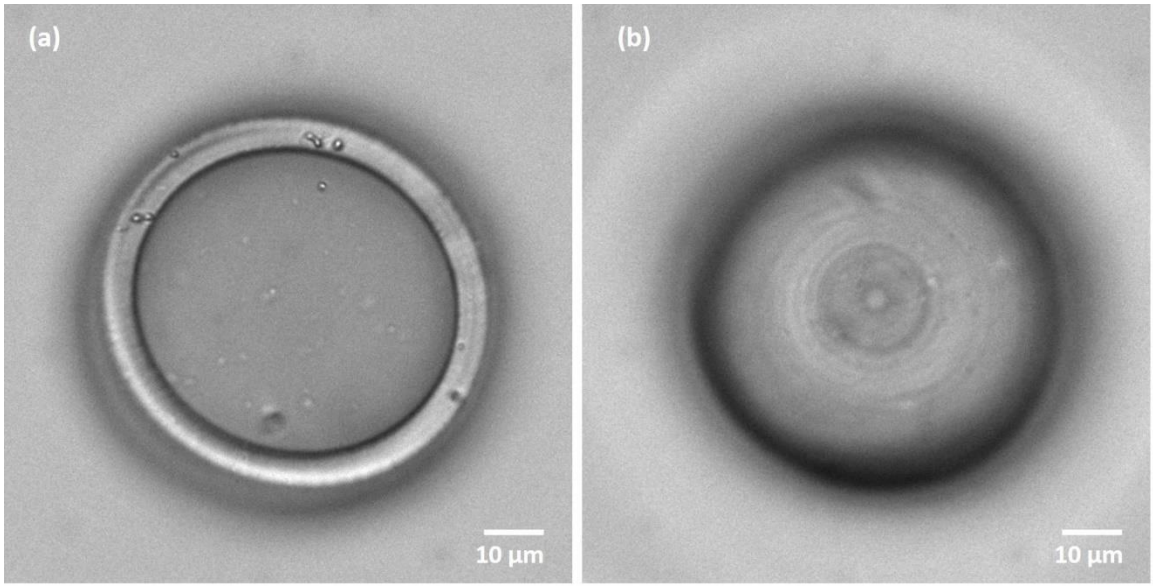

Figure 2.4: Bright field images of a hydrogel dome fabricated with a new DMD displaying structural integrity from the bottom (a) and the top (b).

The laser itself can also create a host of problems if not functioning properly. For example, power fluctuations can result in striations in the structures as the beam is changing in stability over the course of the scan. These are displayed in Figure 2.5 (a) and (b), where the red lines give an indication of the angle of striations, which can be identified as the small, tightly packed lateral lines across the dome (a) and pad (b). While these striations may not appear as disruptive as the DMD aberrations, they indicate a lack of overall structural integrity, and the success rate of products like these adhering to the coverslip through multiple rinses is significantly reduced.

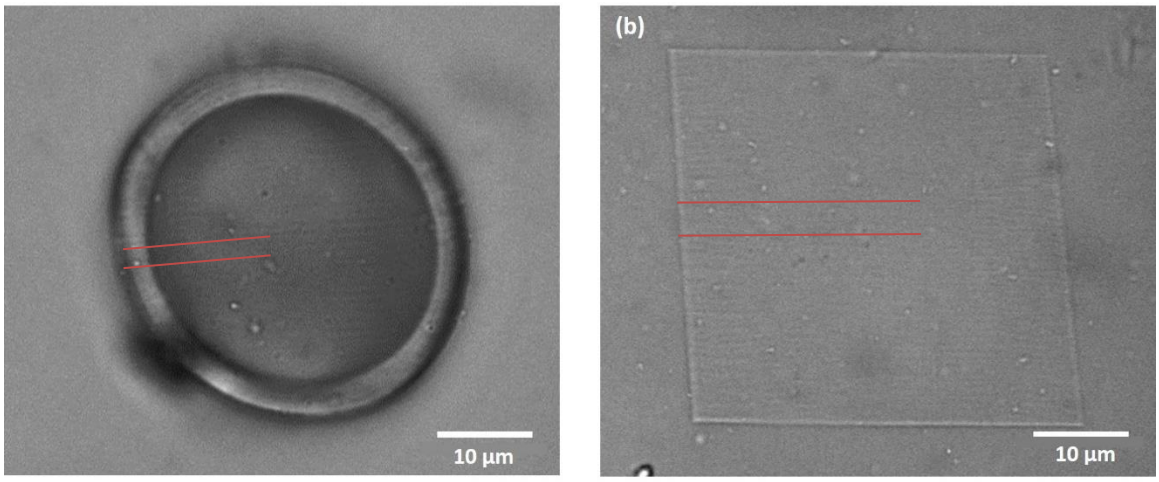

Figure 2.5: Bright field images of hydrogel structures fabricated with a variable pump laser output. Consistent lateral striations of less than a micron apart are visible on both the dome (a) and the pad (b). Red lines indicate the angle of the striations for reference purposes only.

While minor laser fluctuations can cause the striations see above, more serious ones can prohibit fabrication entirely under the conditions typically used for fabrication. The laser system can display poor stability for various reasons (e.g., environmental, diode stability, mirror cleanliness, etc.), as exemplified in Figures 2.6 and 2.7. Figure 2.6 (a) depicts power measurements taken at the output window of the Tsunami over an approximately 2 hour period, showing not only a cyclic type variation in power over this time period, but a minimum of 676 mW and a maximum of 707 mW, around a 30 mW difference. This reflects ~4% of the ~700 mW average, a substantial amount for a nonlinear process [100]. A 4% difference can result in mW differences at the back aperture, which depending on the application can be extremely disruptive. Figure 2.6 (b) is a recording of the power before the scan mirrors, where a similar cyclical pattern in power output is seen over a period of ~15 minutes.

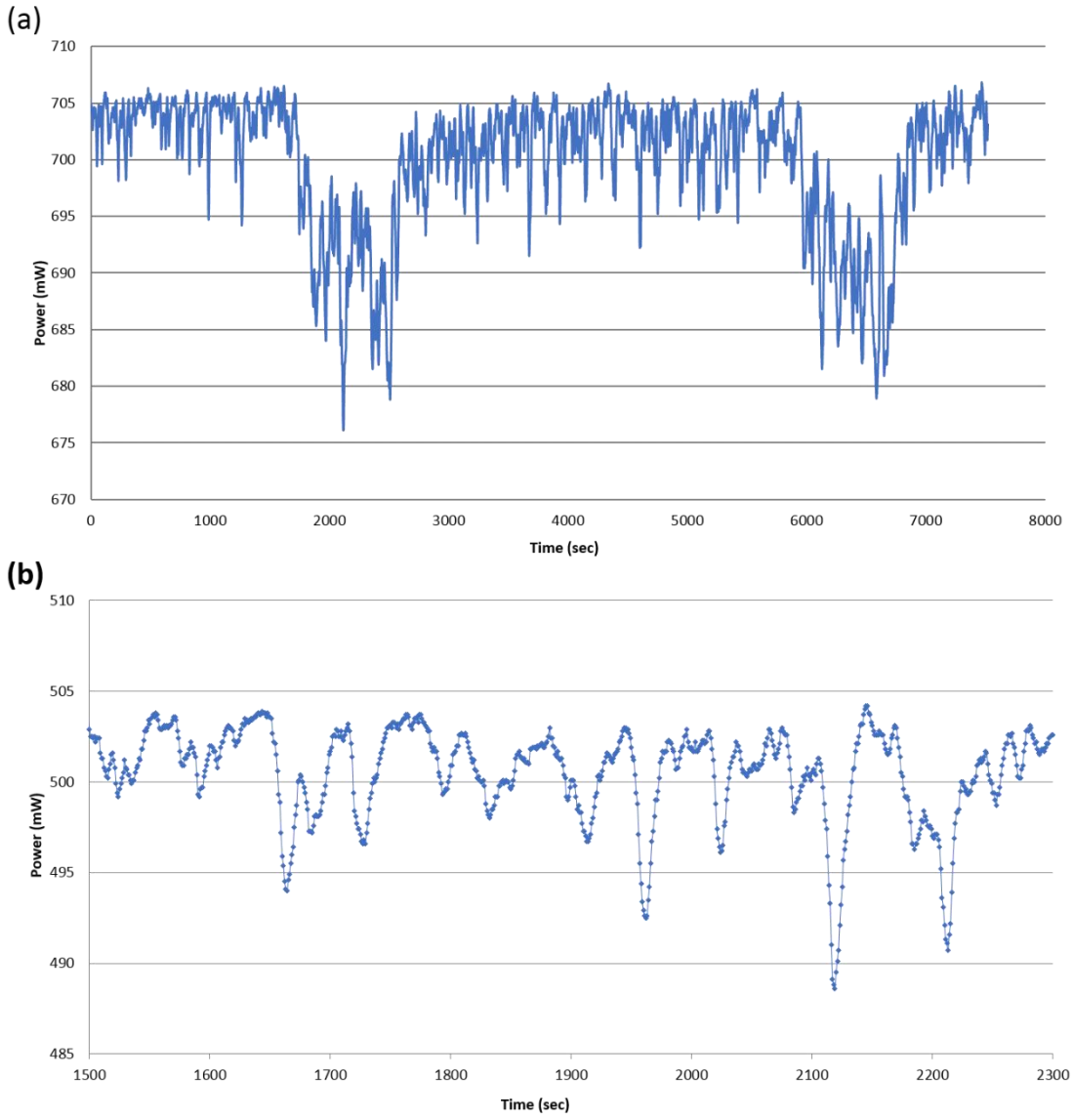

Figure 2.6: Graphs depicting laser power at the output window for ~2 hours (a) and before the scan mirrors for ~15 minutes (b).

Figure 2.7 (a) shows the power while scanning, just before the entrance to the microscope. This pattern should reflect the wave pattern of the y scan mirror on the galvo scanner, which is set to sawtooth (inset) and the dashed vertical lines indicate the general position of the wave reset. It is clear that not only is the scan power throughout one cycle

variable, but the average power output over this time period is variable as well, with a maximum of ~51 mW and a minimum of ~46 mW. This illustrates the compounding nature of the table elements with respect to power loss, as described earlier.

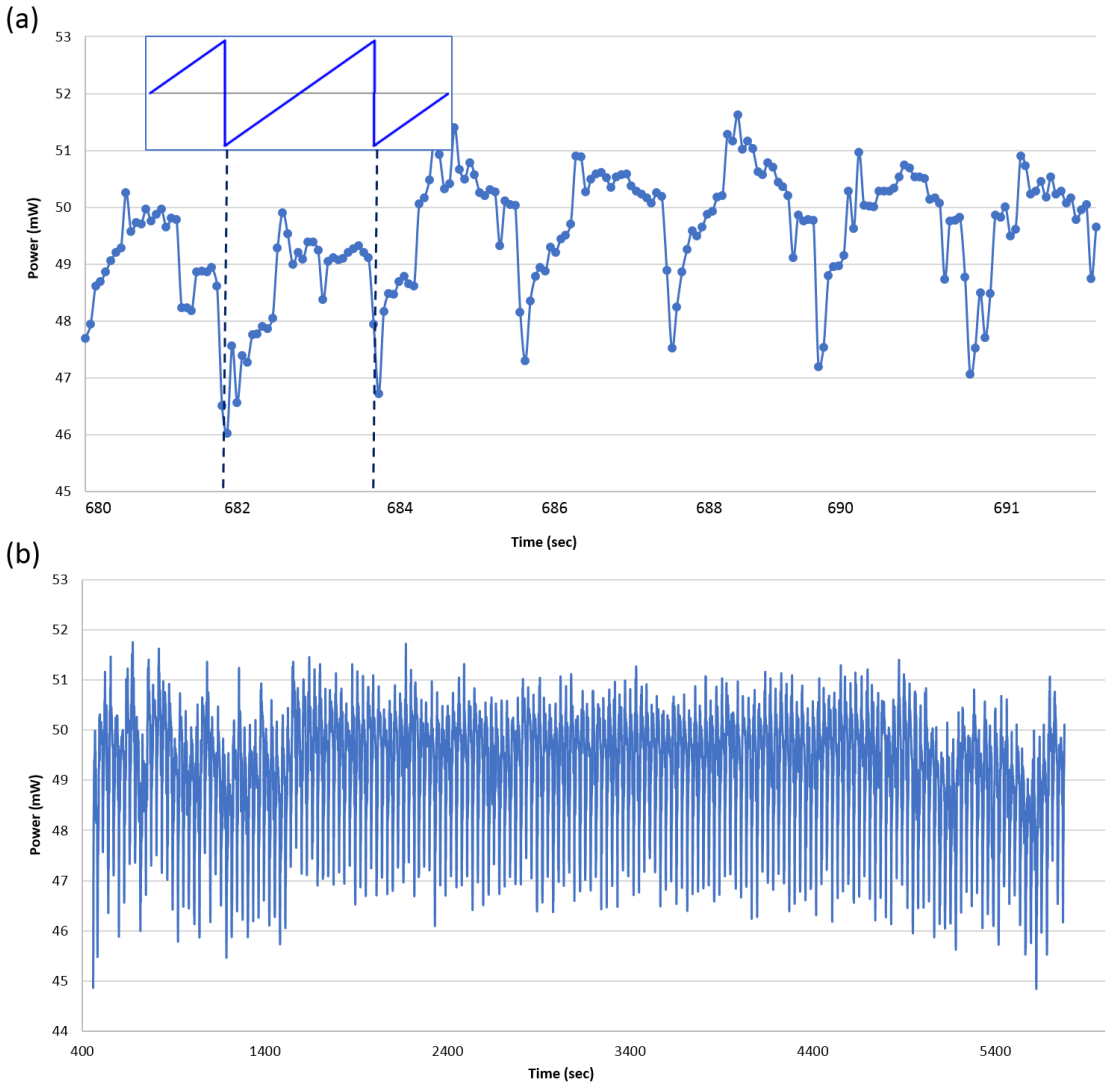

Figure 2.7: Graphs depicting laser power during scanning prior to entering the microscope for ~15 sec (a) and ~1 hour and 30 minutes (b). Inset in (a) indicates the sawtooth wave function applied to the y axis galvo scan mirror, and the vertical dashed lines indicate approximately where the reset should be.

Figure 2.7 (b) monitors the scan power at the same position for approximately an hour and a half. Again, variable power is seen in the maximum and minimum of ~52 and ~45, as well as in the scan reset values (the bottommost portion of each line in the graph) and the scan itself (the darker areas of the scan near the top).

Without a means to fix the laser itself, it was suggested that accommodations be made to account for these power fluctuations, such as increasing the overall power to raise the average power, scanning through structures twice to improve structural integrity, changing the y scan frequency and subsequently amplitude, and changing the step size. These amendments are outlined in Tables 2.1 and 2.2, and the corresponding bright field images of the trial results are shown in Figures 2.8 and 2.9, respectively.

Trial	1&2	3	4	5	6	7	8	9	10
Power (mW)	275	275	275	275	285	265	265	265	275
Step Size (µm)	0.5	0.5	0.25	0.5	0.5	0.5	0.25	0.5	0.5
Y Frequency (mHz)	200	200	200	200	200	200	200	200	100
Y Amplitude	1.25	1.25	1.25	1.25	1.25	1.25	1.25	1.25	2.5
Waveshape	sawtooth	sawtooth	sawtooth	sawtooth	sawtooth	sawtooth	sawtooth	sawtooth	sawtooth
Time (sec)/Plane	5	5	5	5	5	5	5	5	10
Other Parameters	-	(top down)	-	(scan twice)	-	-	-	(scan twice)	-

Table 2.1: Trial 1 parameters to compensate for lack of laser stability. Power is measured in mW before the scan mirrors, the step size refers to the z-axis intervals, and the y frequency/amplitude correspond to the speed of the y scan mirror, hence the alteration of the time per plane in the last column. "Scan twice" simply means to rescan through a finished structure, and "top down" indicates an attempt at stepping down through solution to anchor to the coverslip instead of building up from it.

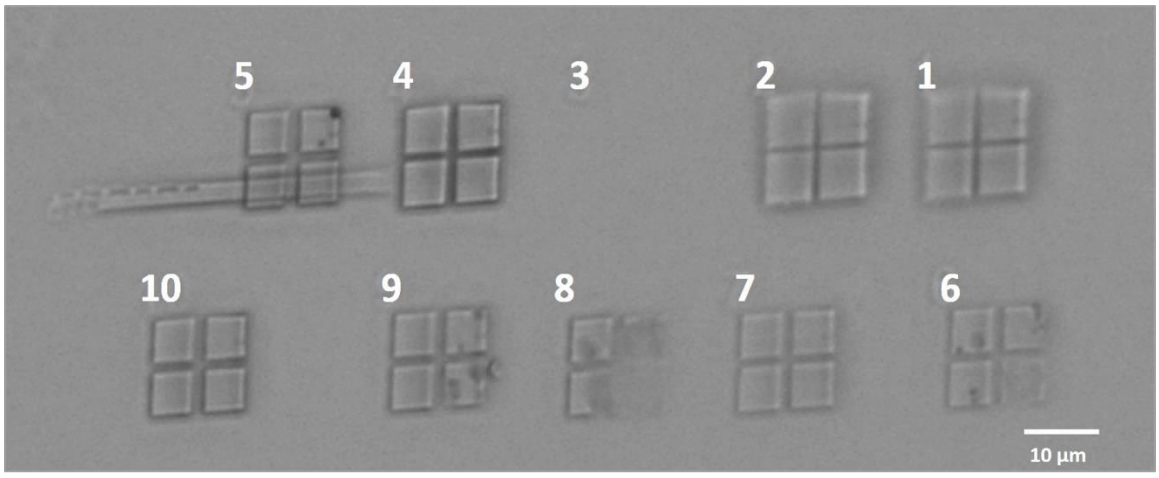

Figure 2.8: Bright field image depicting the results of Trial 1 parameters to compensate for the lack of laser stability.

Figure 2.8 displays the results of Trial 1. While 1 and 2, the original scan settings, appear moderately successful, the blurred edges and low optical density of the pads indicate a lack of integrity that is unlikely to withstand multiple rinses. The top down scan (3) did not yield a product at all. Parameter 4 involved cutting the step size in half, and 5 required a rescan through the structure, both achieving the same end goal. However, as can be seen in 5, visible as a black circle in the top right, this resulted in explosions, where the solution became overheated by the laser. This is also present in 4 but harder to identify in the plane of focus displayed, but a darker region between the top and bottom right pads indicates an explosion at a deeper focus plane. Simply raising and lowering the power did not achieve improved fabrication (6 and 7). A smaller step size at a lower power, 8, produced multiple explosions, and scanning twice at a lower power, 9, had similar results. Slowing down the scan at the normal power, 10, did seem to improve the structural integrity, but doubles the time necessary for µ3D printing, and for many applications is prohibitive.

Trial	1&2	3	4	5	6	7	8	9
Power (mW)	275	275	275	285	265	265	265	275
Step Size (µm)	0.5	0.25	0.5	0.5	0.5	0.25	0.5	0.5
Y Frequency (mHz)	200	200	200	200	200	200	200	100
Y Amplitude	1.25	1.25	1.25	1.25	1.25	1.25	1.25	2.5
Waveshape	sawtooth	sawtooth	sawtooth	sawtooth	sawtooth	sawtooth	sawtooth	sawtooth
Time (sec)/Plane	5	5	5	5	5	5	5	10
Other Parameters			(scan twice)				(scan twice)	

Table 2.2: Trial 2 parameters to compensate for lack of laser stability. Power is measured in mW before the scan mirrors, the step size refers to the z-axis intervals, and the y frequency/amplitude correspond to the speed of the scan in the y dimension, hence the alteration of the time per plane in the last column. "Scan twice" simply means to rescan through a finished structure.

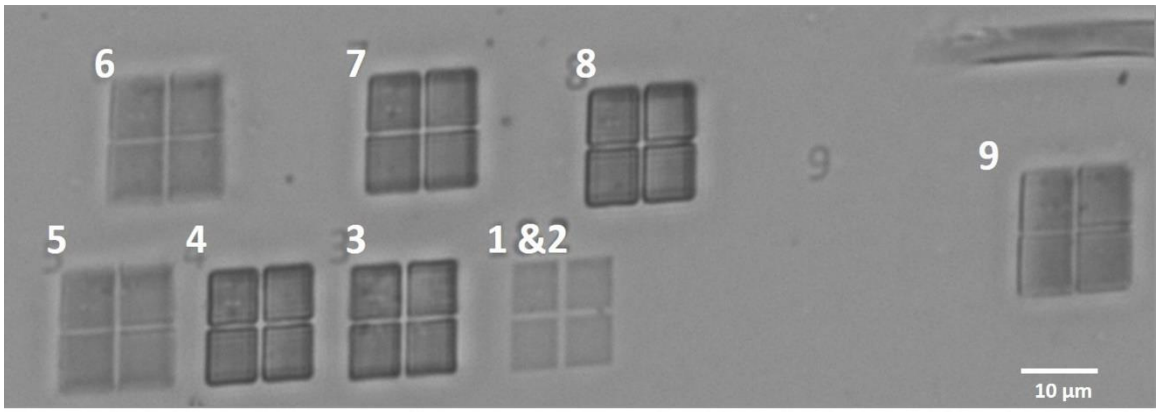

Figure 2.9: Bright field image depicting the results of Trial 2 parameters to compensate for the lack of laser stability.

Figure 2.19 shows the results for Trial 2, this time the original settings yielded only one four-square structure out of two, as seen under the 1&2 label. Reducing the step size by 50% did improve the results of 3 slightly, and rescanning this time, 4, did not result in multiple explosions. Simply raising and lowering the power, 5 and 6, did not improve

results, but lowering the power and reducing step size by 50% or lowering the power and rescanning, 7 and 8, did. This time slowing the scan at the usual settings did not improve results consistently, evidenced by the blurring edges of 9.

Despite the fact that these trials were carried out within a day of one another, it is apparent that even the same parameters, such as Trial 1-8 and Trial 2-7, or Trial 1-9 and Trial 2-8, yielded different results. Consistent fabrication is key to reproducibility, an important characteristic of these hydrogels when considering attributes such as porosity, diffusivity, stiffness, structural integrity and more. In a working system, consistent reliable products are able to be created, such as the pads shown in Figure 2.10 and 2.11. Figure 2.10 shows bright field images taken from the coverslip of two structures, a 4 µm tall pad (a) and an 8 µm tall pad (b). The triangle in the upper corner of each pad is present only in the last layers, and is for focusing at the top of the structures. Figure 2.11 shows a plane of focus higher up in solution for the same two pads from 2.10, illustrating a lack of deviation as the laser translated up through the z-axis.

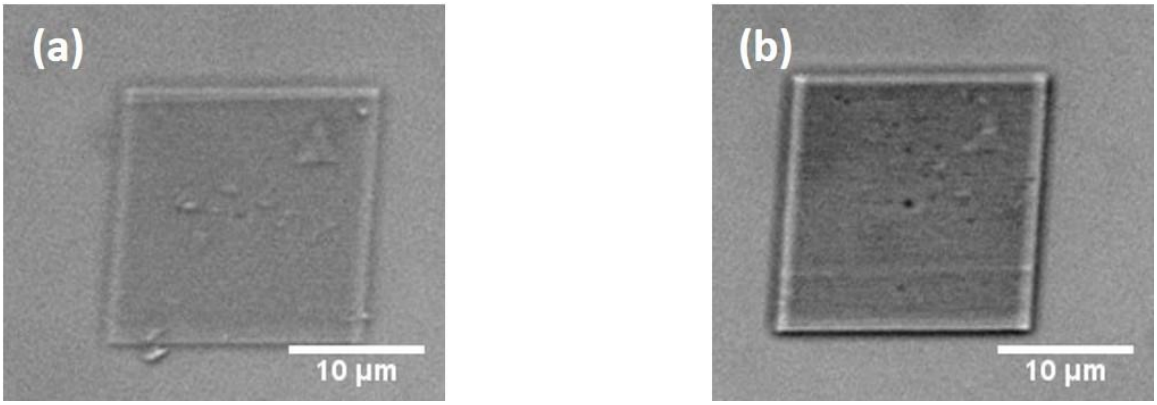

Figure 2.10: Bright field images depicting structures fabricated with a stable laser power and a functional DMD viewed from a plane near the coverslip. A 4 µm tall pad (a) and an 8 µm tall pad (b) are shown.

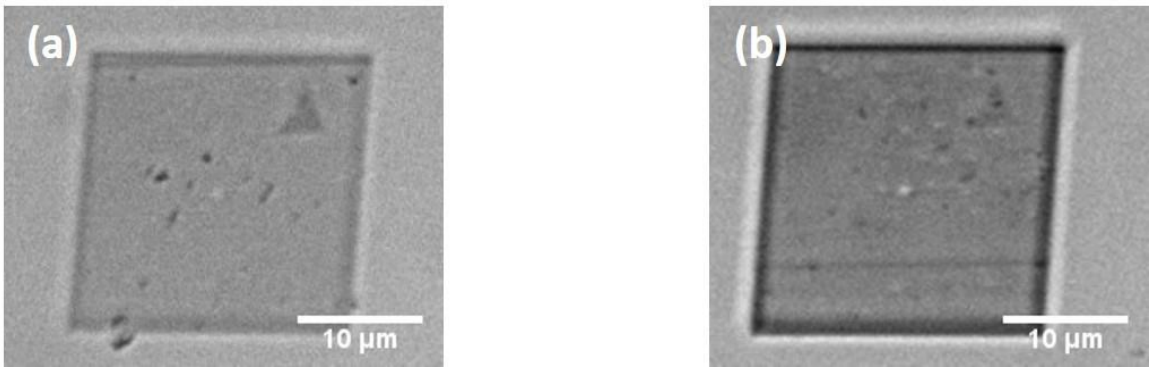

Figure 2.11: Bright field images depicting structures fabricated with a stable laser power and a functional DMD viewed from a plane near the top of the taller pad. The same 4 µm tall pad (a) and 8 µm tall pad (b) from Figure 2.10 are shown.

CONCLUSION

This chapter covered an in depth look at the current technologies being employed in the Shear lab, and the importance of various techniques and equipment to µ3D printing. A detailed explanation of the general optical table setup required for the fabrication of protein hydrogels was outlined and discussed, highlighting the lasers, scan mirrors, DMD, microscope setup, and programs. Next, the "Project Beam the Laser through the Wall" was discussed, including the challenges presented, and the ultimate outcome that included beam divergence too extensive to overcome with available optics. Additional challenges were addressed with respect to setting the table up in a new building, including the lack of apparent divergence from traditional optical guidelines on the previous setup, and the necessity for similar methods with the new table. The importance of the proper function of all components was explored in detail in the final section. It was observed that a DMD with defects could result in poor structural integrity and an inability to contain microbial populations to complete studies with respect to their communication and biogeography. Next, the effect of laser power instability was addressed, including the production of

striations and weak structural integrity. The laser power fluctuations were monitored over time at the laser output, before the scan mirrors, and while scanning just before the microscope. It was observed that while a low percentage of the total power did not seem to be an issue at the output, downstream it could be greatly exacerbated by the addition of optics and equipment such as the scan mirrors and DMD. Images were taken of various trials to account for the power fluctuations with a variety of fabrication parameters, but in the end it was shown that many of these are unreliable and can change in effect day to day. In the end, it was concluded that well-functioning equipment can produce superior structures, and that those products are reproducible and will reliably have consistent characteristics (like diffusivity, pore size, crosslinking density, ect.) that are required for the study of sociomicrobiology.

Chapter 3: Designing a Platform for Studying Unculturables

INTRODUCTION

Unculturable Bacteria and *Vibrio fischeri* as a Model Organism

Aliivibrio fischeri, more commonly known as *Vibrio fischeri*, is gram negative microbe found in marine environments throughout the world. It is important as a model organism in the investigation of biofilm formation, quorum sensing, bioluminescence, and bacterial symbiosis with animals, due to its somewhat famous association with Hawaiian bobtailed squid [46], [101]–[103]. In addition, the genome for *V. fischeri* has been completely sequenced, allowing for investigation into phylogeny, resulting in its recent change in genus [104]. As a result, in the investigation of new means to culture "unculturable" marine organisms, *V. fischeri* presents an attractive opportunity for researchers. It demands culture conditions, such as low temperature, high salinity, increased viscosity, and similar nutrient availability, which are required by these as of yet un-sequenced bacteria [105], [106]. Increasing its attractiveness as a substitute for these microbes is that it grows robustly in a laboratory setting under proper conditions [103]. Consequently, it was chosen as a stand in for these proof of concept studies. The general concept behind these studies involves the idea that unculturable cells are unable to grow and divide normally as a result of lacking key nutrients and/ or factors in their environment that are not being provided by laboratory culture conditions. This could involve a range of necessary ions, carbon sources, chemical signaling from surrounding cells, physical properties of the media, and other aspects of their local environment [107]. Providing them with the conditions necessary to grow might be achieved using μ3D printing. As shown in the schematic presented in Figure 3.1, a sample of seawater and the microbes suspended therein would serve as the solvent for the protein and photosensitizer typically solubilized

in buffer or media. A single cell could be trapped using the fabrication technique presented previously in Chapters 1 and 2. Residual fabrication solution could them be washed away, and seawater from the original sample from which the bacterium was trapped could be reintroduced. Thus, the newly trapped bacterium would be free to grow and divide within the diffusible trap walls surrounded by its native environment, to a greater extent. Provided that cellular division occurs, the trap containing the cells could be reclaimed, and the cells inside harvested for genetic sequencing, particularly 16s RNA sequencing, which is highly conserved between different species of bacteria [44], [108].

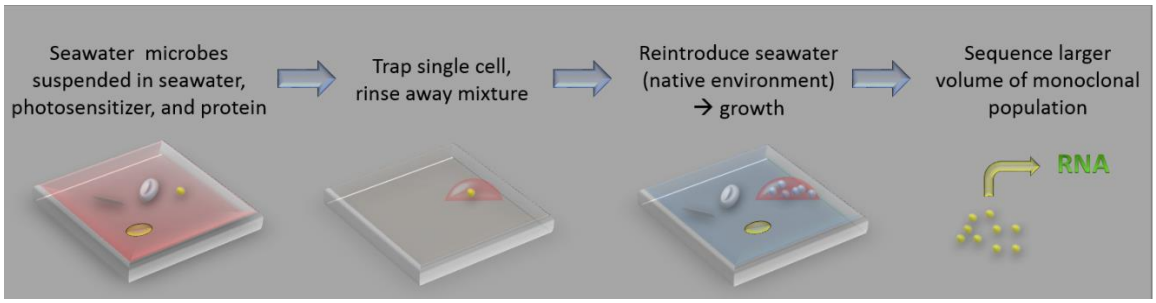

Figure 3.1: Schematic of trapping unculturable sea microbes to facilitate growth to obtain material for RNA sequencing. Native seawater containing microbes is used as the solvent for creating fabrication solution, and following the trapping of a single cell of interest, is reintroduced in order to encourage growth of the trapped cell. Following sufficient divisions, the trap is reclaimed and the cells within sequenced.

Protein Conjugated Photosensitizers

Previously in the Shear lab, a variety of components have been used as photosensitizers in the creation of the hydrogel precursor, or fabrication solution [20], [109], [110]. Rose bengal and methylene blue have become staples, as they yield hydrogel products with high structural integrity and tend to be tolerated by at least a subset of cell types of interest to the lab. However, in applications involving sensitive cell types, it has

become necessary to conjugate the photosensitizer to a protein, to prevent its ability to enter the cell and cause damage as a result of oxidative or free radical reactions [109]. Tethering the photosensitizer to a much larger molecule, such as proteins like bovine serum albumin (BSA) or gelatin, reduces the ability of these damaging species to cross the cell membrane, as shown in Figure 3.2, below [111].

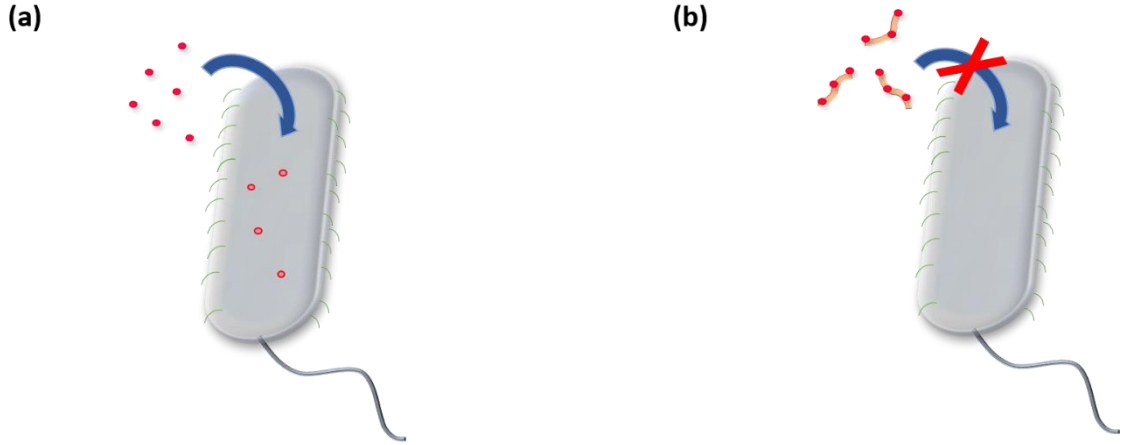

Figure 3.2: Schematic of cellular exposure to photosensitizer (red dots) vs. photosensitizer conjugated to gelatin (red dots along beige string). Free photosensitizer can readily cross the bacterial cell membrane (a) but conjugation to gelatin minimizes crossing due to the size of the new molecule (b).

While many bacteria do not seem to be affected by their exposure to photosensitizers at low concentrations for short periods of time, others are highly sensitive [112]. Due to the lack of knowledge surrounding appropriate culture conditions for the un-sequenced marine bacteria, precautions were taken to conjugate photosensitizer to the gelatin component of the fabrication solution to minimize potential ill effects on the cells.

A common photosensitizer that has been conjugated to gelatin previously in the Shear lab is eosin [109]. Eosin is available for purchase with an isothiocyanate group attached, allowing conjugation to gelatin through reactions with lysine residues along the gelatin fragments. Through the use of an established protocol, this reaction can be

performed yielding approximately one mmol of eosin per fifteen grams of gelatin, or 5 tags per fragment [113]. This process has been shown to be effective in creating fabrication solutions that are minimally cytotoxic to both bacterial and mammalian cells [109]. The general reaction scheme is shown in Figure 3.3, below.

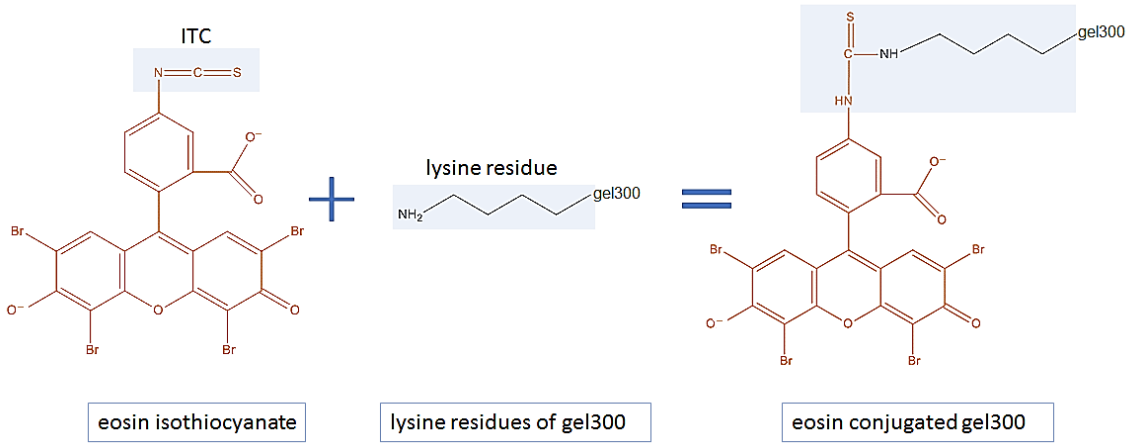

Figure 3.3: Schematic of eosin isothiocyanate conjugation to gelatin. In this case, "gel300" refers to the Bloom number, and this represents attachment to 300 Bloom porcine gelatin Type A.

EXPERIMENTAL DESIGN AND METHODS

Initial experimental design involved a proof of concept study to determine whether marine bacteria could be trapped using hydrogel precursor solutions developed in the Shear lab. This process involved designing a sea media fabrication solution containing eosin isothiocyanate (ITC) conjugated gelatin which minimized potential damage to cells. Additionally, it was necessary for the melting temperature to be low enough to prevent cell death. This would allow bacteria, specifically *Vibrio fischeri*, to be introduced into the solution and trapped. Subsequently, the gelatin could be melted away in order to reintroduce their sea salts growth media as seen in Figure 3.4. This would mimic the

isolation, trapping and reintroduction to native media (e.g. seawater and the microbes and molecules naturally contained therein) of marine bacteria proposed in Figure 3.1.

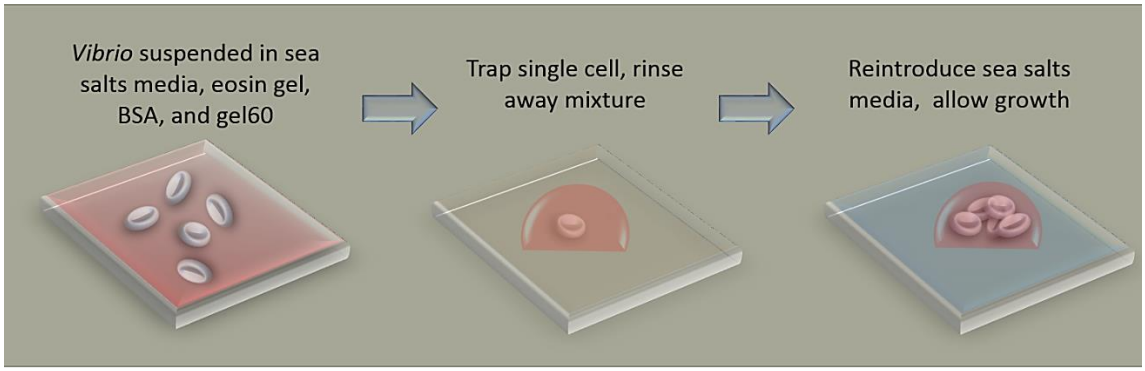

Figure 3.4: Schematic *Vibrio fischeri* trapping and reintroduction to sea media. "Eosin gel" refers to eosin ITC conjugated gelatin Type A, 300 Bloom. "BSA" refers to bovine serum albumin, and "gel60" refers to porcine gelatin Type A, 60 Bloom.

Reagents

Bovine serum albumin (BAH64-1639) was purchased from Equitech-Bio (Kerrville, TX). Gelatin Type A from porcine, 300 Bloom (G-1890 and G-2500), lysozyme (L-6876), sea salts media (S9883), apomyoglobin (A8673), yeast extract (Y1625), tryptone (T7293), glycerol (G-6279), peptone (PO431), agar (A5306), and methylene blue (M9140) were acquired from Sigma-Aldrich (St. Louis, MO). Gelatin Type A from porcine, 60 Bloom (16560) was obtained from Electron Microscopy Sciences (Hatfield, PA). Eosin-5-isothiocyanate (E-18) was acquired from Invitrogen (Carlsbad, CA). Rose bengal disodium salt (R323-25), sodium hydroxide (SS266-1), dimethyl sulfoxide (D128-500), and sodium chloride (S271-3) were purchased from Fisher BioReagents (Fairlawn, NJ). Protoporphyrin IX (102757) and eosin Y disodium salts (152471) were obtained from MP Biomedicals (Santa Ana, CA). Malachite green (63160) was purchased from Fluka (Morris

Plains, NJ). HEPES sodium salt (AC21500-1000) was acquired from Acros Organics (Geel, Belgium). Tryptic soy broth (R455052), Hyclone L-15 Leibovitz media (SH30525.01) and BupH phosphate buffered saline packs (28372) were purchased from Thermo Scientific (Waltham, MA).

Bacterial Strains, Plasmids, and Culture Conditions

Vibrio fischeri ES114 was cultured from freezer stock on sea salts agar plates containing 40 g L^{-1} sea salts medium, 5 g L^{-1} peptone, 1 g L^{-1} yeast, and 15 g L^{-1} agar in deionized (DI) water. Overnight cultures were grown at ~20 °C, in sea salts media containing 40 g L^{-1} sea salts, 5 g L^{-1} tryptone, 3 g L^{-1} yeast, and 3 mg L^{-1} glycerol in DI water. The following day 10 µL of these cells were diluted into 4 mL of the sea salts media and allowed to grow for two hours at room temperature until reaching mid-logarithmic phase. These rapidly dividing cells were then diluted into fabrication solution at a 1:5 ratio immediately before use.

Conjugation Protocol

A protocol was followed to obtain eosin-5-isothiocyanate (eosin ITC) conjugated to gel300 at a rate of approximately 5 eosin tags per gelatin fragment, or one millimole eosin per 15 grams gel300. Following this process, the ratio of conjugated to unconjugated gel300 was approximately 1:10. The original protocol is presented below, and all amendments will be addressed in later sections.

First a 0.1 M sodium bicarbonate buffer was prepared by thoroughly dissolving 25.12 g of sodium bicarbonate into 3 L of DI water at RT and subsequently titrating with sodium hydroxide (NaOH) to a pH of 9.0.

The material for conjugation was prepared by dissolving 11.2 mg eosin ITC into 1 mL dimethyl sulfoxide (DMSO) previously filtered through a Corning 0.2 μm pore RC syringe/disc filter (CLS431212) from Sigma (St. Louis, MO). 100 mg gel300 was then measured into a 25 mL flask, to which approximately 9 mL buffer was added. This solution was stirred and gently heated on a hot plate at 37 °C to dissolve (10 minutes). The eosin/DMSO solution was subsequently added and the flask was covered with aluminum foil and stirred overnight at 37 °C (15 hours).

The following day, a Float-A-Lyzer G2 8-12 kD 10 mL dialysis tube (G235067) from Spectrum Labs (Los Angeles, CA) was soaked in 10 % ethanol in DI water for 15 minutes. This solution was introduced to the interior of the tube as well to ensure complete exposure to the ethanol water solution. Next, this solution was removed, and the tube was filled with and soaked in DI water for 15 minutes. Finally, the tube was emptied and filled with the eosin ITC gel300 mixture from the flask, placed in the large beaker of remaining buffer, and soaked overnight (15 hours) at RT with stirring.

The following day the buffer was replaced with DI water and the tube was soaked with stirring all day (8 hours). At the end of the day, the eosin ITC gel 300 (eosin gel) solution was transferred from the dialysis tubing into a 50 mL centrifuge tube, flash frozen by immersing in liquid nitrogen, and lyophilized for two days.

Optimization of Fabrication Conditions

The novelty of this technique required several optimization steps to create a working fabrication solution. First, the salinity of sea salts raised the question of whether any photosensitizer would be able to dissolve into culture media. To determine this, three photosensitizers previously used for fabrication by the Shear lab were tested at concentrations frequently used to make structures. Namely, 5 mM rose bengal, 5 mM

methylene blue, and 10 mM free eosin Y were each added to 1 mL volumes of 60 °C sea salts media and vortexed briefly. All solutions were then sonicated in a 60 °C heated water bath for one hour. Methylene blue and eosin Y both solubilized, however, rose bengal created a precipitate. Methylene blue and eosin Y were subsequently tested to determine fabrication quality. To each one mL vial of sea media and photosensitizer, 40 mg mL^{-1} BSA, and 200 mg mL^{-1} gel60 were added. These were vortexed briefly, then placed in an oven at 60 °C for half an hour followed by a heated 37 °C shaker for 3 hours. To each of two Teflon sample wells containing #1 borosilicate coverslips, 60 µL of the respective solutions were added and allowed to cool to ~20 °C. Fabrication was performed as described in Chapter 1, at a power of ~35 mW at the back aperture, to create 15 x 30 µm pads measuring 5 µm tall. 500 µL of sea salts media was then added to each well and they were placed in the incubator at 37 °C for 45 minutes. Following this, the wells were rinsed via pipetting to remove uncrosslinked gelatin, and fresh media was added. All structures remained adhered after the rinse. Subsequently, tests were performed to determine if the protein ratios of the eosin conjugated gelatin solutions previously used in the Shear lab would yield similar results. A solution of 30 mg mL^{-1} BSA, 100 mg mL^{-1} gel60, and 80 mg mL^{-1} eosin gel was created using the method described earlier in this section. Test fabrication at a power of ~45 mW at the back aperture yielded successful pad structures following a rinse. However, due to the low temperature culture conditions required for *V. fischeri* (20 – 26 °C), a 27.8 °C melting temperature solution would not allow the survival of the cells during the rinsing process [103]. Thus, a new solution was created containing 60 mg mL^{-1} BSA, 50 mg mL^{-1} gel60, and 80 mg mL^{-1} eosin gel in sea salts media, with a melting temperature of 22.3 °C. This was used with a power at the back aperture of ~45 mW, and fabrication of the pads was performed as previously described. These conditions were used for all further studies, in which hollow dome structures, Figure 3.5, were created

to test the integrity of a model hollow structure for capturing cells. Bright field images of the printed domes are shown in Figure 3.6.

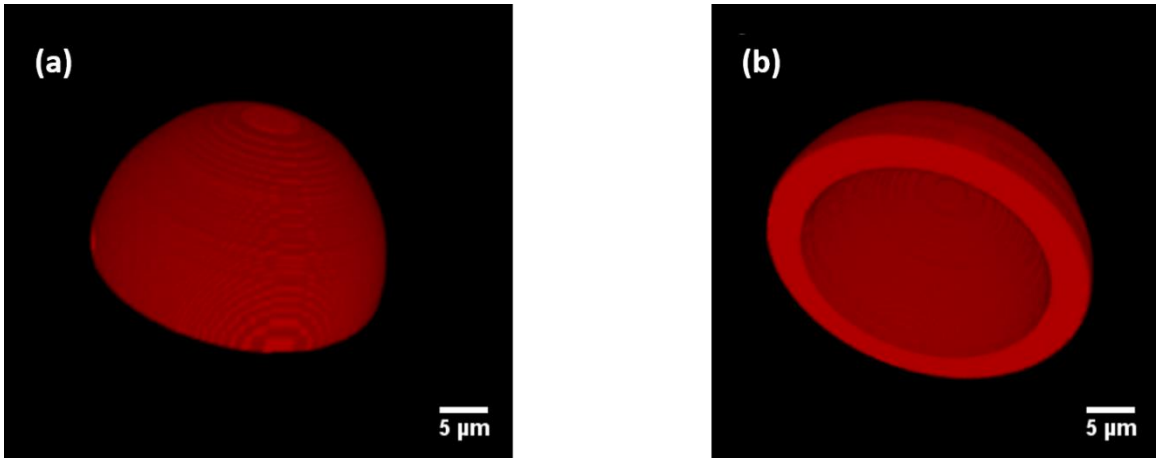

Figure 3.5: 3D render of dome design to test integrity of hollow structures made with eosin gel, viewed from above (a) and from underneath (b).

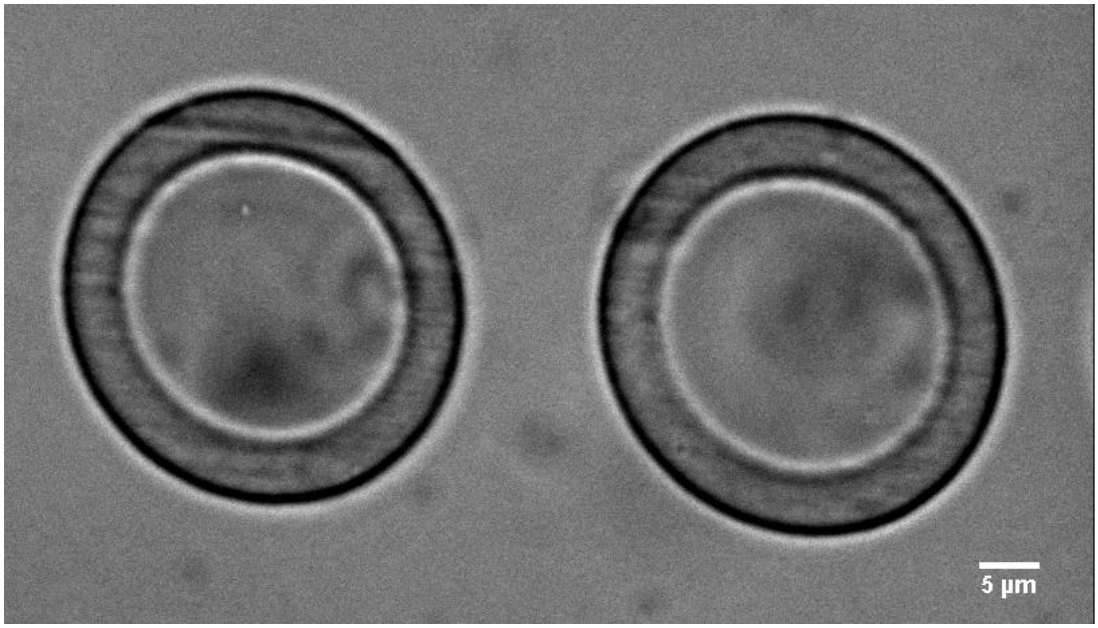

Figure 3.6: Bright field image of successful fabrication of the eosin gel dome structure designs in Figure 3.5, post-rinse.

Following a visual assessment of the images shown in Figure 3.6, taken post fabrication and following multiple aggressive rinses, the domes were determined to be stable. Thus, *V. fischeri* in exponential phase were diluted into the 24 °C fabrication solution at a ratio of 1:5, vortexed briefly, and allowed to shake at 24 °C for 15 minutes to eliminate bubbles in the solution. A 60 µL droplet of this cell solution was then deposited onto a coverslip in a Teflon well and allowed to cool to RT. Cells were trapped using the layer by layer approach described in Chapter 1, using the design referred to as "square to dome" shown in Figure 3.7. Following fabrication, 500 µL of sea salts media, heated to 25 °C was added to the sample well and rinsing was performed via pipetting. New media was introduced to the well, and the cells were allowed to grow at RT inside these structures for 18 hours.

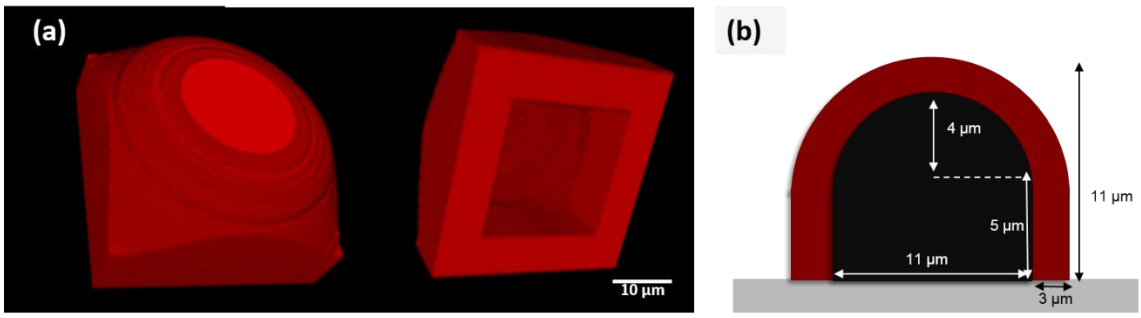

Figure 3.7: "Square to dome" structure top and viewed from above (left) and below (right) in (a) and dimensions (b).

RESULTS AND DISCUSSION

Successful Culturing of *Vibrio fischeri*

Prior to capturing the cells in hydrogel structures, a brief experiment was performed to determine cell viability in the sea salt media. Exponential phase cells were introduced to the fabrication solution, at a 1:5 ratio at 24 °C and allowed to mix on the heated shaker at

the same temperature for 15 minutes. As an initial test, 60 μL of these cells in solution was then pipetted into a sample well and allowed to sit for a further 30 minutes to encourage attachment to the coverslip. The wells were then rinsed at 25 °C in sea media and the attached cells were allowed to grow. The coverslip was observed at 2 hours and 18 hours post-rinse. This resulted in bacterial growth, as shown in Figure 3.8, indicating that the solution was not highly cytotoxic.

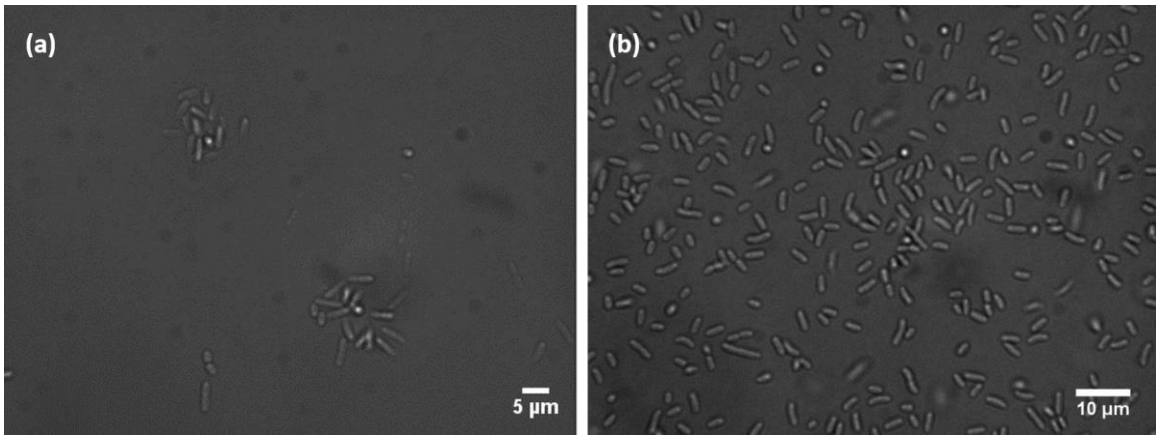

Figure 3.8: Bright field images of *V. fischeri* cells on the coverslip, two hours (a) and 18 hours (b) after rinsing away fabrication solution.

Once this was assessed, cell trapping was attempted as detailed earlier in the chapter. Following the rinse, individual cells were visible in the traps as shown in Figure 3.9 (a). These were allowed to grow for 18 hours at RT, and following a subsequent rinse with fresh sea media, it was clear the cells had divided within the structures, Figure 3.9 (b).

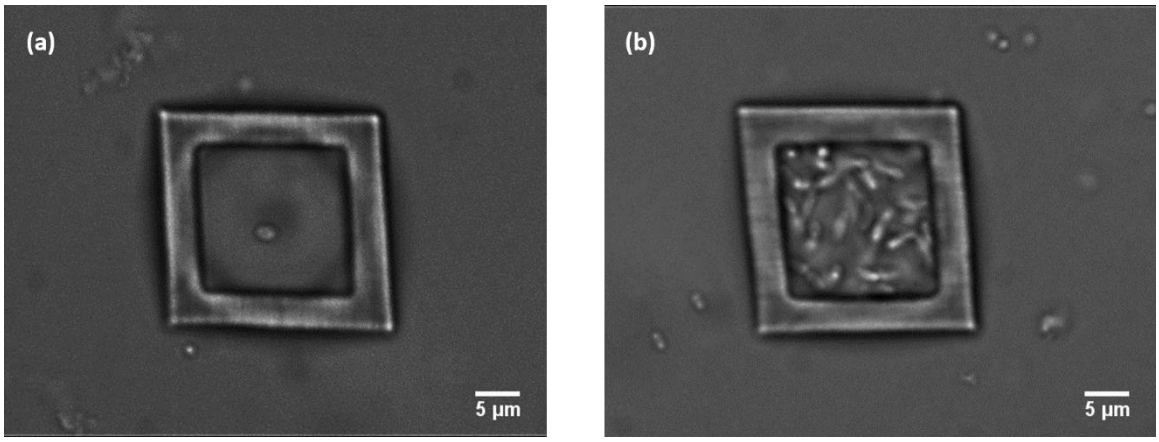

Figure 3.9: Bright field images of *V. fischeri* cells within the protein microstructures, immediately post-rinse (a), and after 18 hours (b).

It was clear from these experiments that the sea salts growth media did not affect the solubility of the photosensitizer and protein in any noticeable way, and that the eosin gel solutions and fabrication process did not have any noticeable detrimental effects on the *Vibrio fischeri*. These two observations taken together hold promise towards the isolation and culturing of unculturable marine microbes. Manufacturers of the sea water media claim the salinity and viscosity of the media mimics ocean water with a high degree of efficacy. Thus, it is possible that introducing microbes and seawater into the fabrication solution and trapping individual cells may not have a damaging effect on them, while rinsing with fresh seawater filled with the same microbes may encourage the growth of the unculturable strains.

Conjugation Troubleshooting

Following successful trials in which *V. fischeri* were captured and cultured, the conjugation process designed to tether the free eosin to the gelatin, and thus protect the cells from absorbing toxic photosensitizer, began to fail. The resultant lyophilized product appeared spongy and collapsible, as opposed to the fluffy protein that had previously been

obtained, Figure 3.10 (a). Upon mixing with the ingredients necessary to make the fabrication solution, the pink eosin conjugated gelation separated into a distinct layer at the bottom of the vial, Figure 3.10 (b). It was noted that while visible separation in the dialysis tubing, Figure 3.10 (c), always resulted in a poor product, it was not sufficient to assume that a homogeneous solution in the tubing would result in a successful end product.

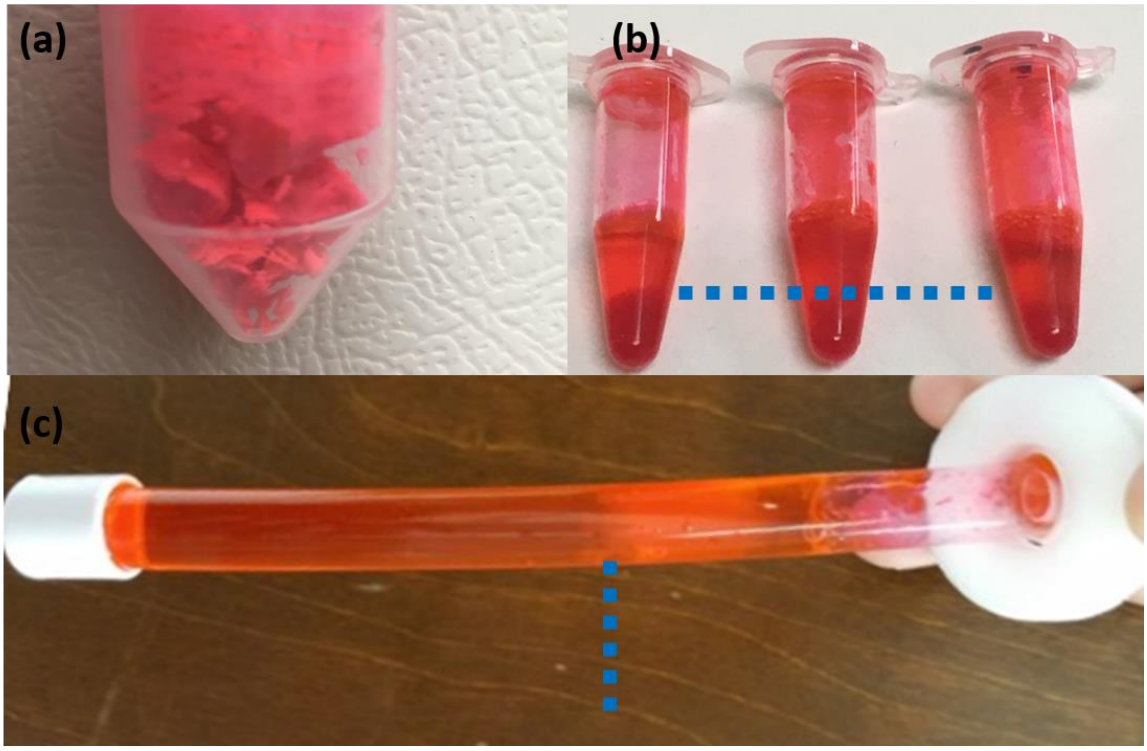

Figure 3.10: Images of the failed eosin conjugated gelation: lyophilized spongy material (a), separated eosin conjugated gelatin in solution (b) and separated bilayers in the dialysis tubing (c). Blue dashed lines indicate interface of bilayers.

Despite the obvious separation of the solution, fabrication of structures was attempted. The solution was placed in a 60 °C oven for half an hour, then vigorously vortexed and immediately pipetted onto a coverslip in a Teflon sample well. After cooling, the droplet was observed using bright field microscopy as shown in Figure 3.11. It is clear

that the solution is heterogeneous in all portions of the droplet, and that the treatment in the oven and vigorous vortexing did not solve the issue.

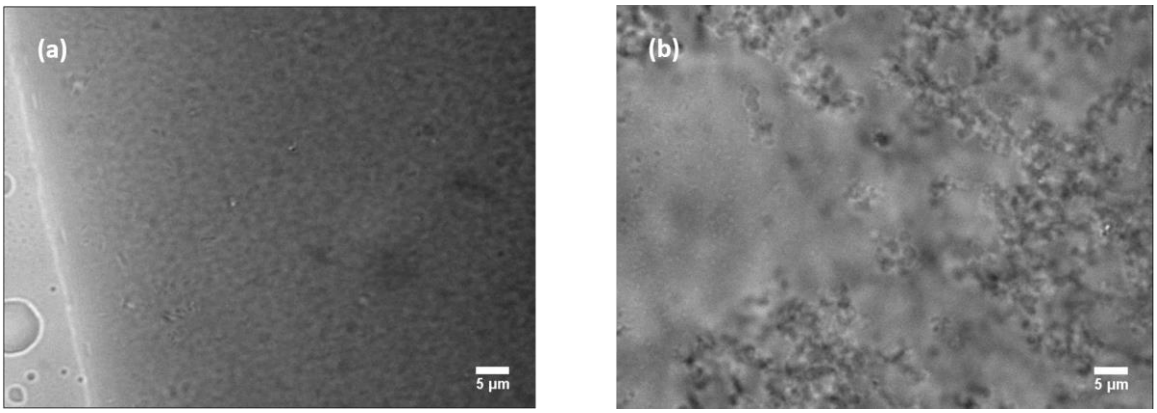

Figure 3.11: Bright field images of heterogeneity in the eosin gel fabrication solution, (a) at the droplet edge, and (b) in the middle of the droplet.

Fabrication was attempted despite the obvious lack of homogeneity, but the resulting structures were highly irregular and did not resemble the intended dome structure, Figure 3.12.

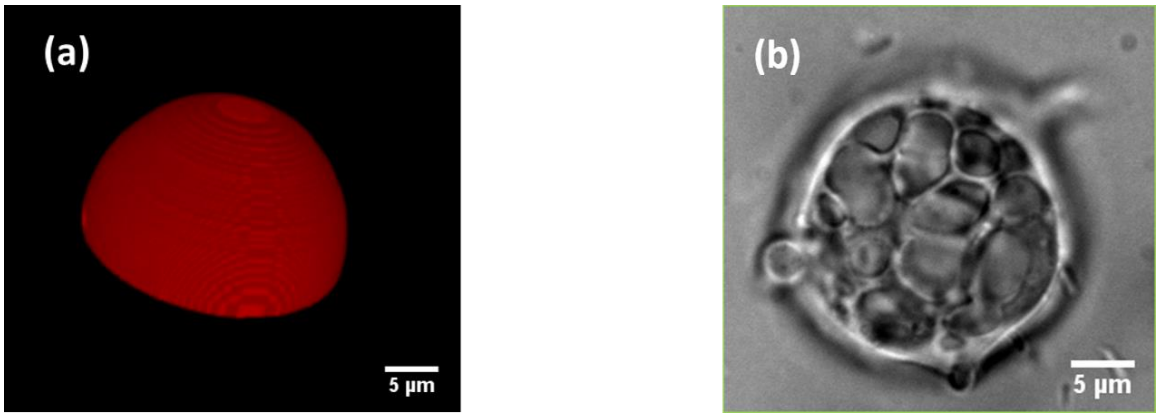

Figure 3.12: 3D render of the dome design used to test eosin conjugated gelatin fabrication (a), and the resultant structure (b).

Subsequently, numerous attempts were made to discover the source of the problems with conjugation. The following list describes actions taken to discover the step in which conjugation was failing:

- Two different lyophilizers were used to ensure a correlation with instrument malfunction
- An attempt was made to rotovap the product instead of lyophilizing, considering that perhaps the liquid nitrogen preparation step was a factor
- Two separate researchers tried the same protocol side by side to minimize random error
- Eosin Y was added to the gelatin and lyophilized without the conjugation step, to determine if the conjugation step was the primary issue
- BSA, gel60 and gel300 were dissolved at ratios used for fabrication, but at the concentration used for conjugation, and eosin ITC in DMSO was added to this mixture to react with the gel300 component
- Conjugation was attempted without dialysis to eliminate that as a source of interference
- Dialysis of the eosin gel was attempted with a much smaller volume of 1 mL to ensure swift and complete dialysis of the reacted product
- Vigorous stirring during the addition of the eosin ITC – DMSO mixture was performed, and the mixture was added dropwise to the dissolved gelatin to ensure gradual reaction and prevent overloading of reaction sites
- Different CAS numbers of gel300 were used- G1890 and G2500, to ensure the gel300 makeup was not an influencing factor
- New eosin ITC, dialysis tubing, DMSO, and NaOH were purchased to eliminate contamination or chemical expiration as a cause

- Different media and buffers were tested for solubility of the final product including L-15 Leibovitz media, tryptic soy broth, HEPES sodium salt buffer, and phosphate buffered saline solution to elucidate possible solubility issues
- Two solutions, one of the eosin gel in buffer, and one of the BSA and gel60 in buffer, were added together in attempt to prevent the eosin gel from crashing out as a result of adding it simultaneously with BSA.
- Eosin gel was added to a solution of BSA only to determine if the gel60 was a factor
- DMSO was added to a solution of only eosin gel to attempt to prevent BSA interference with solubility upon its subsequent addition
- BSA was left out of the solution, to eliminate its effects on solubility as the cause
- The solution was cooled to 37 °C prior to adding the BSA to avoid aggregation
- Very small increments of BSA were added to a solution of eosin gel and gel60 to determine if the issue was simply due to competing solubility
- Lysozyme and apomyoglobin, respectively, were substituted for BSA to lower the potential for aggregation
- An attempt to conjugate lysozyme with eosin ITC was made to see if the substrate was somehow contributing
- The final concentration of eosin gel in solution was lowered to determine if the solubility of the eosin gel itself was causing insolubility in other proteins
- The conjugation was tried in a different building with a different DI water supply, in order to rule out potential contaminants from the buffer

Following the failure of all of these modifications to produce a working solution, the pH of the solutions was tested and it was found that the pH of the final solution was approximately 11while the isoelectric points of BSA and gelatin are 5.2 – 7 and 4 – 5.5,

respectively [114], [115]. It was thus concluded that proximity of the pH to the isoelectric points of the two proteins was not a factor in the lack of solubility.

A final attempt was made to conjugate alternative photosensitizers to gelatin. Protoporphyrin IX and malachite green are both available as isothiocyanates, and thus were tested for fabrication. While both solubilized easily in buffers, protoporphyrin IX did not result in fabrication, even at very high concentrations (10 and 20 mM) and laser power (60 mW at the back aperture). Malachite green on the other hand made structures with a high degree of fidelity at the same concentrations, with powers at the back aperture of 47 and 45 mW, respectively. Unfortunately, an attempt at conjugating malachite green ITC to gel300 resulted in an additional failure. During the conjugation step, the malachite green ITC turned a deep blue color and visibly separated from the gelatin during the dialysis step.

PROPOSED FUTURE STUDIES

Despite the numerous failures in producing a successfully lyophilized gel300 eosin ITC conjugate, there is the possibility that the process may work again. Previously in the Shear lab, the author and other researchers have had both success and failure in effecting this conjugation. It is possible that it may work again, provided the issue can be pinpointed. If this is achieved, the next steps would be to replicate the *V. fischeri* experiments. Next would be to obtain a sample of seawater from the University of Texas at Galveston to test the trapping of individual cells and reintroduction of their native environment to see if they can be cultured in this way. Finally, provided they are able to grow into sizeable colonies, one might be able to obtain a large enough sample for ribonucleic acid sequencing, furthering our understanding of these microbes.

CONCLUSION

This chapter covered the proof of concept experiments necessary to begin applying μ3DP to the challenge of collecting genetic material from "unculturable" marine microorganisms using *Vibrio fischeri* as a model organism. First, optimization of fabrication conditions was performed, and it was determined that while rose bengal is not soluble in the sea media required for the growth of marine organisms, both eosin Y and methylene blue are at typical concentrations for μ3D printing applications. BSA and gelatin could also be solubilized easily in the two respective photosensitizer/sea media solutions, and both solutions yielded robust structures following fabrication and rinsing. Using the eosin gelatin conjugation protocol discussed in the chapter, solutions were made using BSA, gel60, and eosin gel concentrations previously used in the Shear lab. While these ratios also produced structurally sound architectures, the melting temperature of the solution was too high to support survival of *V. fischeri* during the rinsing period. Subsequently, a new solution with a melting temperature conducive to their growth was designed. Using this solution, single cells were able to be trapped and successfully grown into monocultures. Unfortunately, due to an as of yet unidentified cause, the conjugation protocol has ceased to be successful. Despite multiple attempts to pinpoint the issue, it remains elusive. However, should a solution to this problem be elucidated, proposed future studies involve replicating the *V. fischeri* experiments, and testing the compatibility of genuine seawater samples to serve as the solvent for the protein/photosensitizer fabrication solution. In this way, individual marine microbes can be isolated and growth to densities sufficient for genetic sequencing, enabling researchers to expand the phylogenetic tree for these organisms that were previously unable to be cultured and categorized.

Chapter 4: Characterizing Materials for Micro 3D Printing

INTRODUCTION

Characterization of protein hydrogels used in the Shear lab has mostly involved tests of stiffness, surface features, changing dimensions, and optical density [17], [110], [116], [117]. Moving forward, characterization of more intrinsic features of the solutions and products such as melting temperature and toxicity of solutions, nature of crosslinks, crosslinking density and structure porosity could provide valuable insight into the nature of these hydrogels. It will also provide a means to design these gels with more predictable qualities in order to maintain a high level of reproducibility with respect to their applications.

Melting Temperature of Hydrogel Precursor Solutions

Physical properties of the fabrication solutions, particularly those involving gelatin, are a valuable place to begin characterization, due to their direct role in facilitating the ability to create unconstrained three dimensional architectures and trap motile cells [17], [20]. As a result, melting temperatures, which can influence both viscosity and the ability of bacterial cells to survive during the rinsing period, were determined for a range of bovine serum albumin (BSA)/gelatin solutions. The effects of varying both concentration and Bloom number, an indication of fragment length, were investigated. Such knowledge will facilitate the educated design of future fabrication solutions, tailored to the specific needs of the individual cell type or experiment.

Porosity of Hydrogels

To date, relatively few studies have been conducted in the Shear lab on protein hydrogel pore size [118]. However, the permeability of these structures to aqueous solutes

is a key aspect of their appeal. The ability of small molecules to pass in and out of the structure walls allows for the transport of cellular nutrients, waste, products and signaling molecules. While diffusion has been investigated in the form of fluorescein tagged gentamicin, a common antibiotic used in the study of antibiotic resistance in *Pseudomonas aeruginosa*, the range of pore sizes present in structures created from different fabrication solutions has not [19]. In an effort to determine average pore size in structures of varying composition, transmission electron microscopy (TEM) was performed on samples fabricated with a range of gelatin concentrations within the original fabrication solution. In addition, solutions were also made in which the BSA concentration was doubled and the gelatin concentration remained the same, in order to determine the contribution of BSA to pore size within the material.

DESIGN AND METHODS

Melting Temperature Determinations

Experiments were performed to determine the effect on melting temperature of increasing gelatin concentration in the hydrogel precursor solutions used in the Shear lab. The 60 Bloom data presented here is courtesy of Allison Myers.

Reagents

Bovine serum albumin (BAH64-1639) was purchased from Equitech-Bio (Kerrville, TX). Gelatin Type A from porcine, 60 Bloom (16560) was acquired from Electron Microscopy Sciences (Hatfield, PA). Gelatin Type A from porcine, 300 Bloom (G-2500) was purchased from Sigma-Aldrich (St. Louis, MO). Rose bengal disodium salt (R323-25) was obtained from Fisher BioReagents (Fairlawn, NJ). BupH phosphate buffered saline packs (28372) were acquired from Thermo Scientific (Waltham, MA).

Experimental Setup

A range of hydrogel precursor solutions were created in order to determine the melting temperature range achievable using common reagents included in fabrication solutions. All solutions contained 5 mM rose bengal (RB) dissolved into 2 mL tryptic soy broth (TSB) via an hour long exposure to a 60 ºC heated sonicator bath. Next, 250 µL of this solution was placed in a 1.5 mL Eppendorf tube to which 40 mg mL^{-1} bovine serum albumin (BSA) was added simultaneously along with a range of gelatin concentrations, either 300 Bloom porcine gelatin Type A (gel300) or 60 Bloom porcine gelatin Type A (gel60), respectively. These concentrations are delineated in Table 4.1. The mixture was then vortexed briefly, placed in a 60 ºC oven for 30 minutes, and placed on a heated shaker at 37 ºC for at least 45 minutes.

Solution Designation	60 Bloom		300 Bloom	
	BSA (mg mL^{-1})	Gelatin (mg mL^{-1})	BSA (mg mL^{-1})	Gelatin (mg mL^{-1})
1	40	75	40	75
2	40	100	40	100
3	40	125	40	125
4	40	150	40	150
5	40	175	40	175
6	40	200	40	200

Table 4.1: Concentrations of BSA and gelatin used in solutions for melting temperature studies.

Determination of melting temperature was performed using a Fluke 179 True RMS multimeter and thermocouple (Everett, WA), along with a Corning PC 420 stirrer/hotplate (Corning, NY), as illustrated in Figure 4.1.

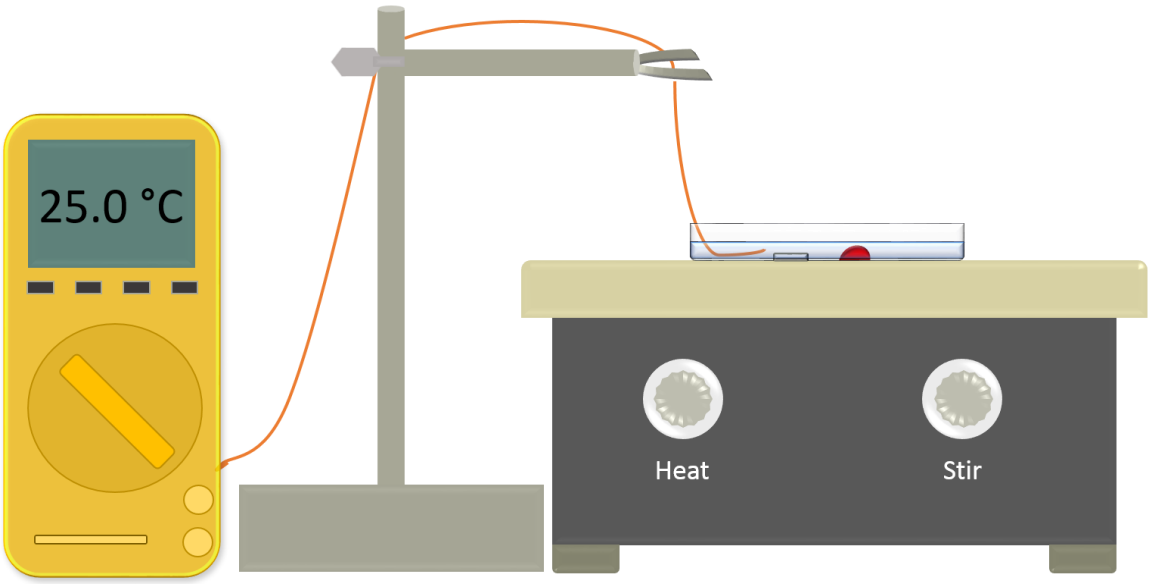

Figure 4.1: Melting temperature determination setup, showing the hotplate with petri dish containing stir bar, gel droplet, and buffer. Thermocouple and multimeter are designated in yellow. Not to scale.

First, a ~22 ºC small glass petri dish was placed upon a RT stirrer/hotplate. A 1 cm stir bar was placed inside, and a 30 µL droplet of solution heated to 37 ºC was placed as close as possible to the stir bar without touching it. The droplet was then allowed to cool to RT. The petri dish was filled to 2/3 capacity with filtered phosphate buffered saline (PBS) and the stirring was set to 6. The thermocouple was then introduced such that it lay parallel to and ~1 mm away from the bottom of the petri dish. It was located as close as possible to the droplet without disturbing it. The heat was then set to 2, allowing the temperature of the buffer and droplet to rise ~0.1 ºC every 30 seconds. The melting temperature was recorded as the temperature displayed on the multimeter when the first strand of melted droplet, visible due to the pink rose bengal component, began to be carried away by the force of the stirring PBS. Subsequent trials were performed with each of the

solutions of various concentrations, after allowing the hot plate to return to RT, and measurements for each were performed in triplicate.

Porosity Studies

Previously in the Shear lab, Dr. Jodi Connell conducted a brief investigation into the porosity of hydrogels composed of bovine serum albumin (BSA) and rose bengal (RB) using transmission electron microscopy (TEM) [118]. The porosity studies presented in this chapter aim to investigate the effects of increasing gelatin concentrations in fabrication solution. Two types of gelatin Type A from porcine were used: 300 Bloom (gel300) and 60 Bloom (gel60). Three concentrations of gel300 were created with 40 mg mL^{-1} BSA and are listed in Table 4.2, where at the median concentration, a separate solution was made incorporating twice the amount of BSA, 80 mg mL^{-1} for comparison. As an additional comparison, a fifth solution was created using the median concentration of gelatin, 150 mg mL^{-1} of gel60, at the doubled BSA concentration of 80 mg mL^{-1}. All solutions contained a final concentration of 7 mM RB.

Solution Designation	300 Bloom		60 Bloom	
	BSA (mg mL^{-1})	Gelatin (mg mL^{-1})	BSA (mg mL^{-1})	Gelatin (mg mL^{-1})
2	40	100	---	---
4	40	150	---	---
4+	80	150	80	150
6	40	200	---	---

Table 4.2: Concentrations of protein used in fabrication solutions for porosity studies.

Reagents

Bovine serum albumin (BAH64-1639) was purchased from Equitech-Bio (Kerrville, TX). Gelatin Type A from porcine, 60 Bloom (16560), Micro-Bed Embedding Resin (50-980-394) and uranyl acetate were obtained from Electron Microscopy Sciences (Hatfield, PA). Rose bengal disodium salt (R323-25) was purchased from Fisher BioReagents (Fairlawn, NJ). Tryptic soy broth (R455052), acetone (A18-500) and BupH phosphate buffered saline packs (28372) were acquired from Thermo Scientific (Waltham, MA). Glutaraldehyde 10% (18426) and ACLAR (10501-10) were obtained from Ted Pella, Inc. (Redding, CA). Coomassie Brilliant Blue G-25 (0615-10G) was purchased from Amresco (Solon, OH). Ethanol (111ANH200) was acquired from Pharmco (Farmer's Branch, TX).

Fabrication Conditions

A 7 mM RB solution was created using phosphate PBS and sonicated for one hour at 60 ºC to solubilize. 500 µL of this solution were then pipetted into a 1.5 mL centrifuge tube to which varying amounts of BSA and either gel60 or gel300 were added. These values were delineated previously in Table 4.2. For each experiment, a 10 µL droplet of solution was pipetted onto a #1 borosilicate glass coverslip seated in a Teflon well, immediately after which a small piece of ACLAR, a polymer film necessary for the resin embedding process, was placed face down upon the droplet. A second coverslip was sandwiched on top of the ACLAR, and the well was screwed tight to create a thin layer of solution as demonstrated in Figure 4.2 (a), which was then allowed to cool to ~22 ºC. This sandwich was necessary to avoid fabricating through the ACLAR, which while mostly optically transparent, did not allow heat to dissipate rapidly during the fabrication process and consequently often melted.

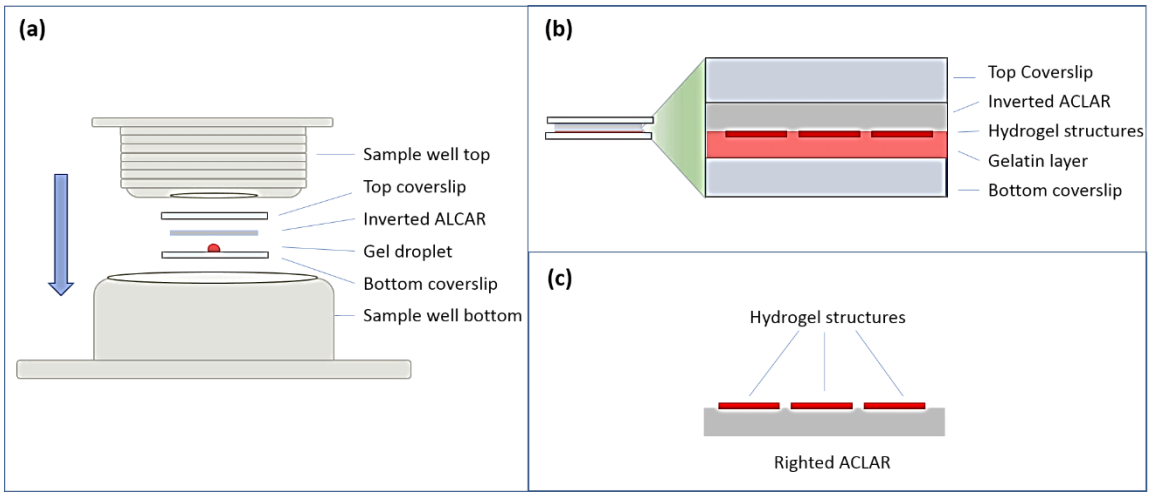

Figure 4.2: Diagram of hydrogel preparation on ACLAR for porosity studies. Sample well assembly with gelatin droplet (a), gelatin and inverted ACLAR sandwiched between coverslips (b), and final product before TEM preparation (c).

Fabrication was then performed at a power of ~35 mW at the back aperture using the layer by layer approach described in Chapter 1. However, instead of building up layer by layer from the coverslip, the process was started 15 µm below the bottom surface of the ACLAR. The resulting fabrication process resulted in a 30 x 40 x 15 µm structure adhered to the ACLAR, such that post-fabrication when the ACLAR was righted the structures would be on top, as seen in Figure 4.2 (b) and (c). Rinsing was performed by allowing the ACLAR and bottom coverslip to soak in a small petri dish of PBS at 37 ºC for one hour, followed by a more vigorous rinsing with warm PBS once the coverslip had detached.

TEM Sample Preparation

Preparation for TEM, with the assistance of Dwight Romanovicz, began with soaking the ACLAR pieces in a 5% (v/v) glutaraldehyde PBS solution for 24 hours. This

was followed by a soak in 0.5% (w/v) solution of Coomassie in PBS for 24 hours. The pieces were then returned to glutaraldehyde solution until further steps.

The structures were dehydrated prior to embedding them in resin. The ACLAR pieces were first rinsed three times in buffer and placed in mini centrifuge tubes before treating with ethanol and acetone. During each step, the previous solution was removed, and the next solution introduced before placing in a Biowave microwave (Ted Pella) at 250 W for 40 seconds. First the buffer was removed and replaced with 50 % ethanol in DI water, then 70 %, 90 % and 100 % respectively. The 100 % step was repeated, and then two treatments were performed in 100 % acetone. Next, four steps were performed with varying concentrations of resin (33 % in acetone, 66 %, and then 100 % resin two times), and microwaved for 5 minutes each. The finished product was sectioned prior to TEM.

Imaging and Data Analysis

Imaging was performed by Dwight Romanovicz using a Thermo Scientific FEI Tecnai Transmission Electron Microscope (Waltham, MA) operated at 80 kV fitted with an AMT Advantage HR 1kX1k digital camera with FFT assistance.

Data analysis was performed using ImageJ software from the National Institute of Health (Bethesda, MD). Obtained TEM images were binarized and given a set threshold, and then using the Particle Analyze tool, the areas of the pores were identified. Histograms of the pore size frequency were generated, and subsequently categories were developed to display the data as number of pores per solution type of a given range. The four ranges include individual pore areas of 0 – 25 nm^2, 25 – 500 nm^2, 500 – 5000 nm^2, and 5000+ nm^2. All analysis was performed in quintuplicate on images with a total area of 2053489 nm^2, a 1433 nm by 1433 nm area.

RESULTS AND DISCUSSION

Melting Temperature Determinations

Data for solutions containing gel60 is courtesy of Allison Myers. The following Figures 4.3 and 4.4 display the melting temperatures obtained for solutions created with gel60 and gel300 gelatin solutions, respectively. Data points with large error bars were repeated more than three times, over different days, and reflect accurately the average of all values obtained. A particular source of the deviation could not be pinpointed at this time.

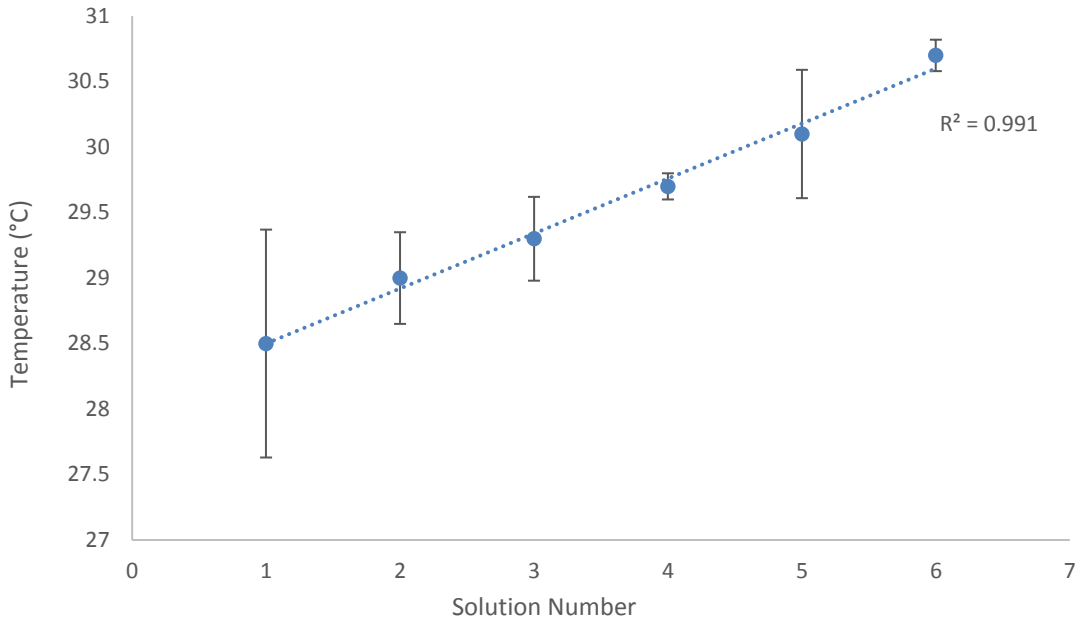

Figure 4.3: Melting temperatures of the 60 Bloom gelatin solutions. The horizontal axis numbers correspond to the values in Table 4.1. Error bars correspond to the standard deviation, n = 3.

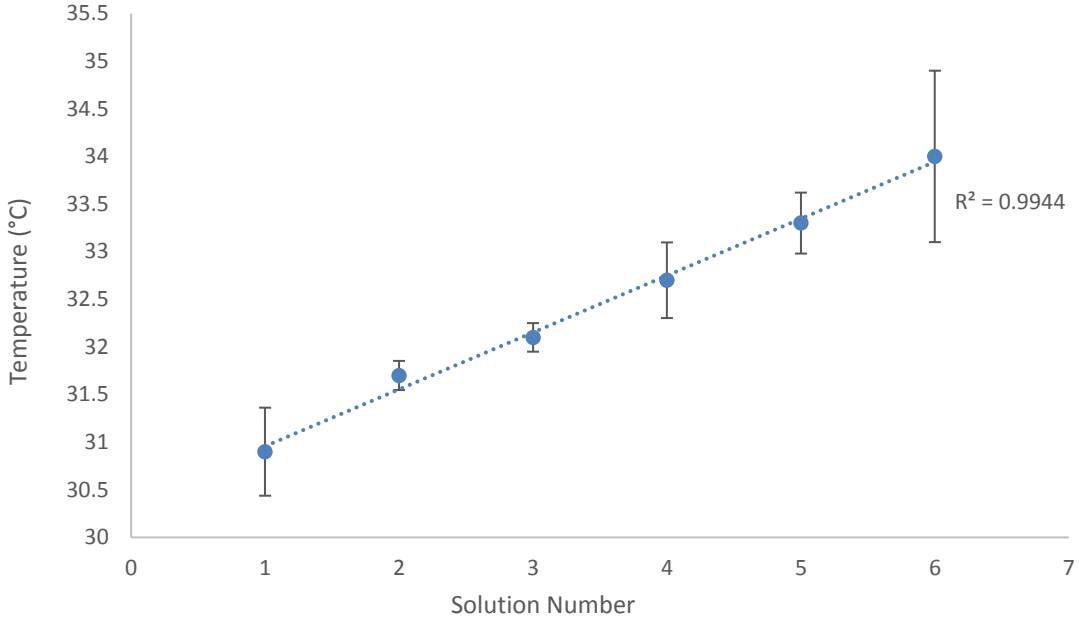

Figure 4.4: Melting temperatures of the 300 Bloom gelatin solutions. The horizontal axis numbers correspond to the values in Table 4.1. Error bars correspond to the standard deviation, n = 3.

It is evident from Figures 4.3 and 4.4 that increasing the Bloom number of the gelatin added increases the melting temperature of the solution overall. Whereas the melting temperature of the gel60 solutions range from 28.5 ± 0.9 ºC to 30.7 ± 0.1 ºC, the gel300 solutions range from 30.9 ± 0.5 ºC to 34.0 ± 0.9 ºC, despite containing identical amounts of gelatin. This rise in melting temperature is likely due to the nature of the gelatin fragments, as increasing the Bloom number correlates to an increase in gelatin fragment length. Another trend that can be observed is that a linear increase in gelatin of either Bloom number corresponds to a linear increase in the melting temperature, as both R^2 values for linear trend lines are above 0.99. This can provide a valuable means of calculating gelatin to BSA ratios that can increase the ease with which the melting temperature of these hydrogel precursor solutions can be tuned. The ability to control this attribute is especially important in consideration of cell trapping. Many microbes have

maximum temperatures at which they can continue to grow and divide, with the upper limits causing cell death. Carefully tuning these solutions to optimize cell survival can ensure that the hydrogel precursor solutions result in minimal cell disruption.

Porosity Studies

Porosity studies, performed alongside Dwight Romanovicz, were used to determine the number of pores within various ranges of pore areas in nm^2, for each of the five fabrication solutions tested. Figure 4.5 displays pores in the 0 – 25 nm^2 range, while Figure 4.6 displays those in the 25 – 500 nm^2 range, Figure 4.7 in the 500 – 5000 nm^2 range, and Figure 4.8 in the 5000+ nm^2 range.

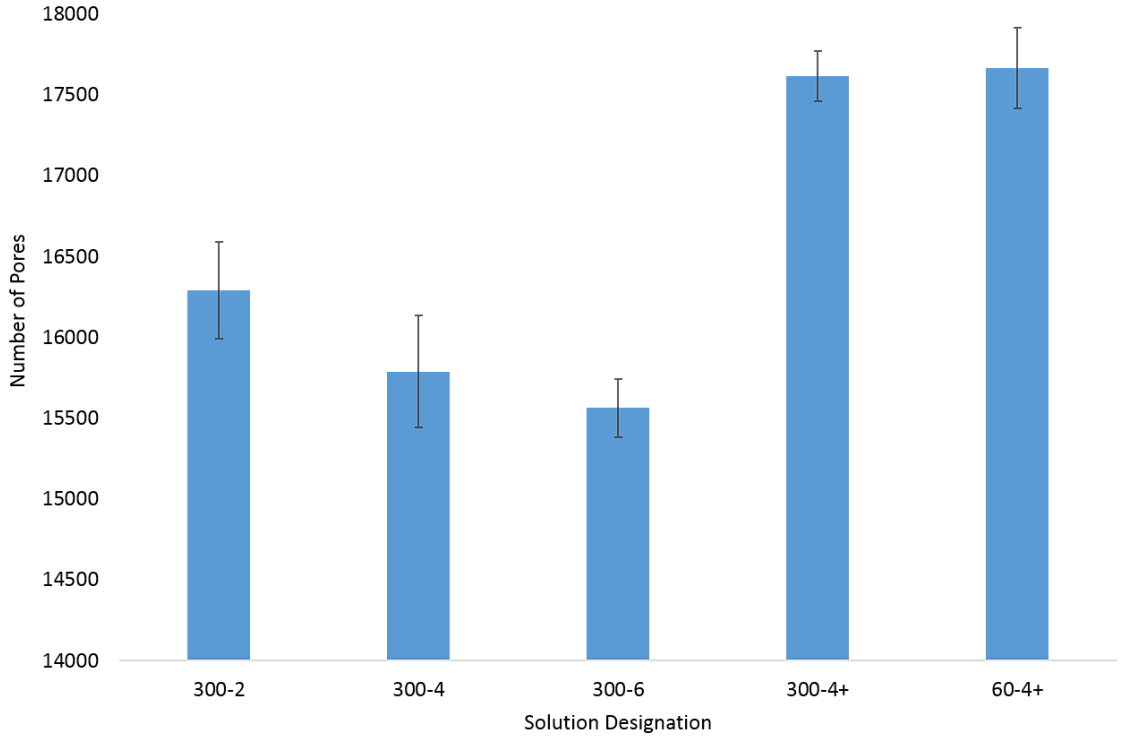

Figure 4.5: Graph displaying the number of pores within the size range of 0 to 25 nm^2 for the five solutions listed in Table 4.2. Error bars represent standard deviation, n = 5.

While the number of pores between 0 – 25 nm^2 appears to decrease with added gel300 for solutions 300-2, 300-4, and 300-6, the average values of 16291 ± 298, 15789 ± 347, and 15562 ± 181 indicate that although 300-2 and 300-6 are statistically significantly different, 300-4 is not significantly different from either 300-2 or 300-6. However, 300-4+ is significantly increased from 300-4, at 17617 ± 156. This indicates that the added BSA reduced the number of pores in the 0 – 25 nm^2 range at the same gelatin concentration. The 60-4+, while statistically similar to the 300-4+ at 17667 ± 250, also has significantly higher levels of 0 – 25 nm^2 pores than the first three gel300 solutions, despite being made with a lower Bloom number gelatin.

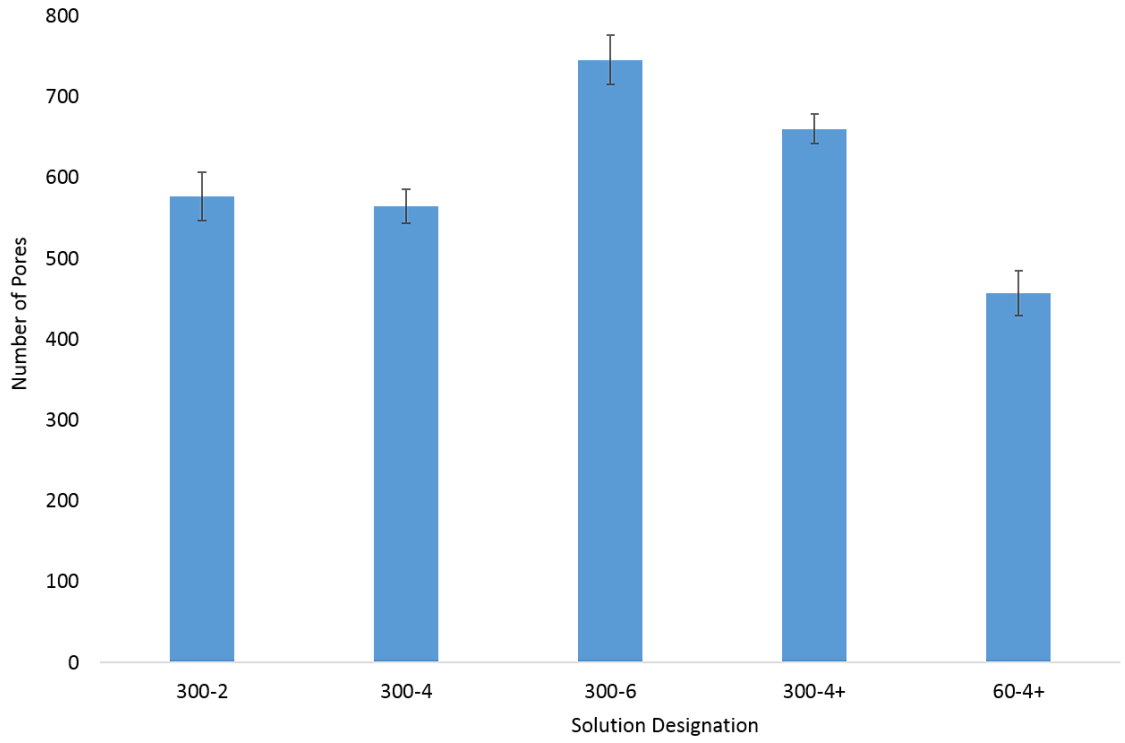

Figure 4.6: Graph displaying the number of pores within the size range of 25 to 500 nm^2 for the five solutions listed in Table 4.2. Error bars represent standard deviation, n = 5.

Again, for 25 – 500 nm^2, the 300-2 and 300-4 solutions are statistically similar with average values of 577 ± 30 and 565 ± 210. However, the 300-6 has an unexpected significant increase at 746 ± 30, considering the addition of protein would be presumed to decrease pore size overall due to the increase in crosslinking site availability. The 300-4+ still has significantly more pores in this range than the 300-4, but less than the 300-6 at 660 ± 18. The 60-4+ has less pores in this range than any of the gel300 solutions, at 457 ± 28, despite previous hypotheses that increasing BSA might decrease pore size, and that 300 Bloom would result in smaller pores than 60 Bloom.

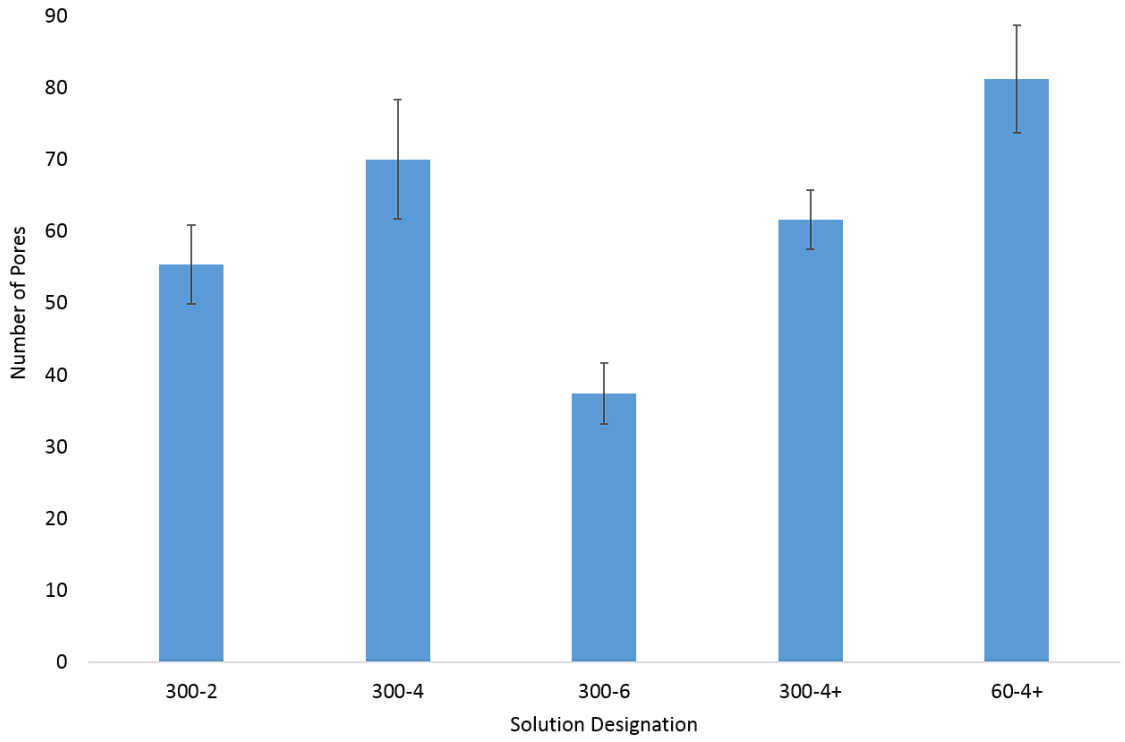

Figure 4.7: Graph displaying the number of pores within the size range of 500 to 5000 nm^2 for the five solutions listed in Table 4.2. Error bars represent standard deviation, n = 5.

In the 500 – 5000 nm^2 the 300-2 and 300-4 are slightly statistically different, with 300-2 having slightly less pores in this range than 300-4, 55 ± 6 versus 70 ± 8, respectively. However, 300-6 has a large significant decrease of pores in this range, at only 37 ± 4. 300-4+ is not statistically different from its 300-4 counterpart, at 62 ± 4. Additionally, the 60-4+ also is statistically similar to the 300-4 solution, at 81 ± 7 pores, but does not share this similarity with the 300-4+ solution.

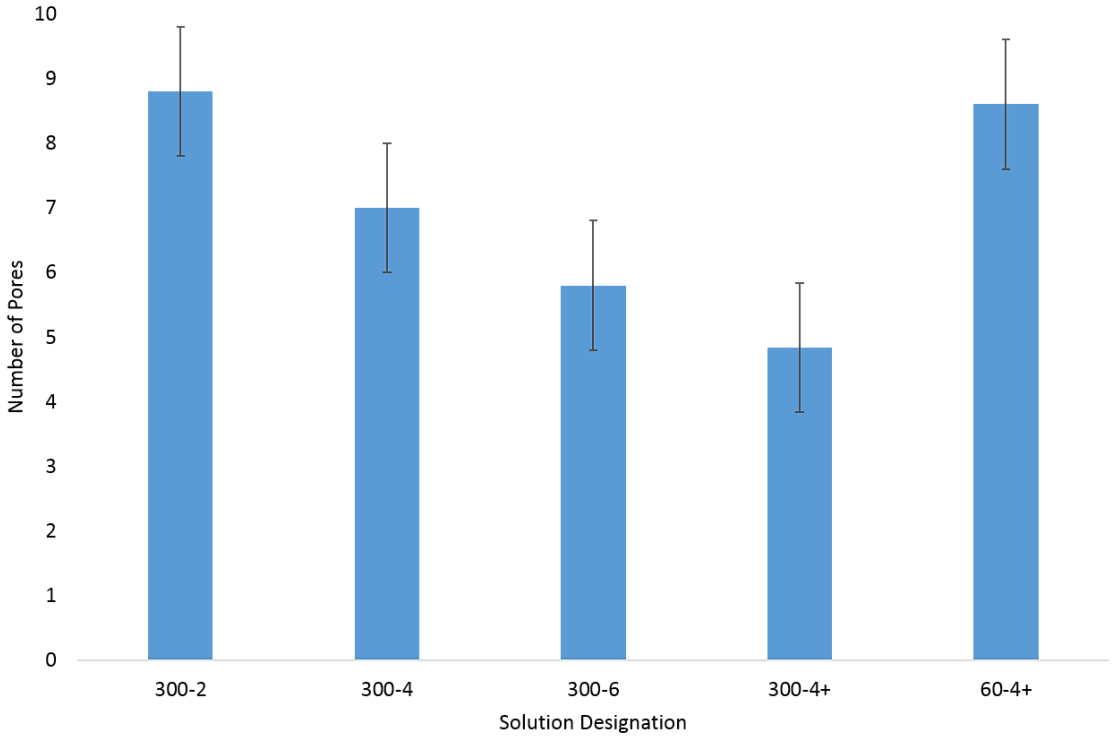

Figure 4.8: Graph displaying the number of pores within the size range of 5000+ nm^2 for the five solutions listed in Table 4.2. Error bars represent standard deviation, n = 5.

Finally, in the 5000+ nm^2 range, again the 300-2 and 300-4 solutions are statistically similar, and the 300-4 and 300-6 solutions are as well, though the 300-2 and 300-6 are significantly different. The pore numbers for the 300-2, 300-4, and 300-6, are 9 ± 1, 7 ± 1, and 6 ± 1, respectively. In this range, the 300-4+ and 300-4 are not statistically

different, with the 300-4+ having 5 ± 1 pores. The 60-4+ is statistically similar to both the 300-2 and 300-4 in this range, at 9 ± 1 pores.

Below, in Figures 4.9 – 4.13 are representative TEM images on which the data analysis was performed. While at a glance, Figure 4.9 and Figure 4.10 may look the same, while 4.11 and 4.12 look similar to each other but not the previous two, and Figure 4.13 looks significantly different, in the end the data must be relied on, as it represents statistical analysis on hundreds of thousands of pores over multiple images for each solution parameter.

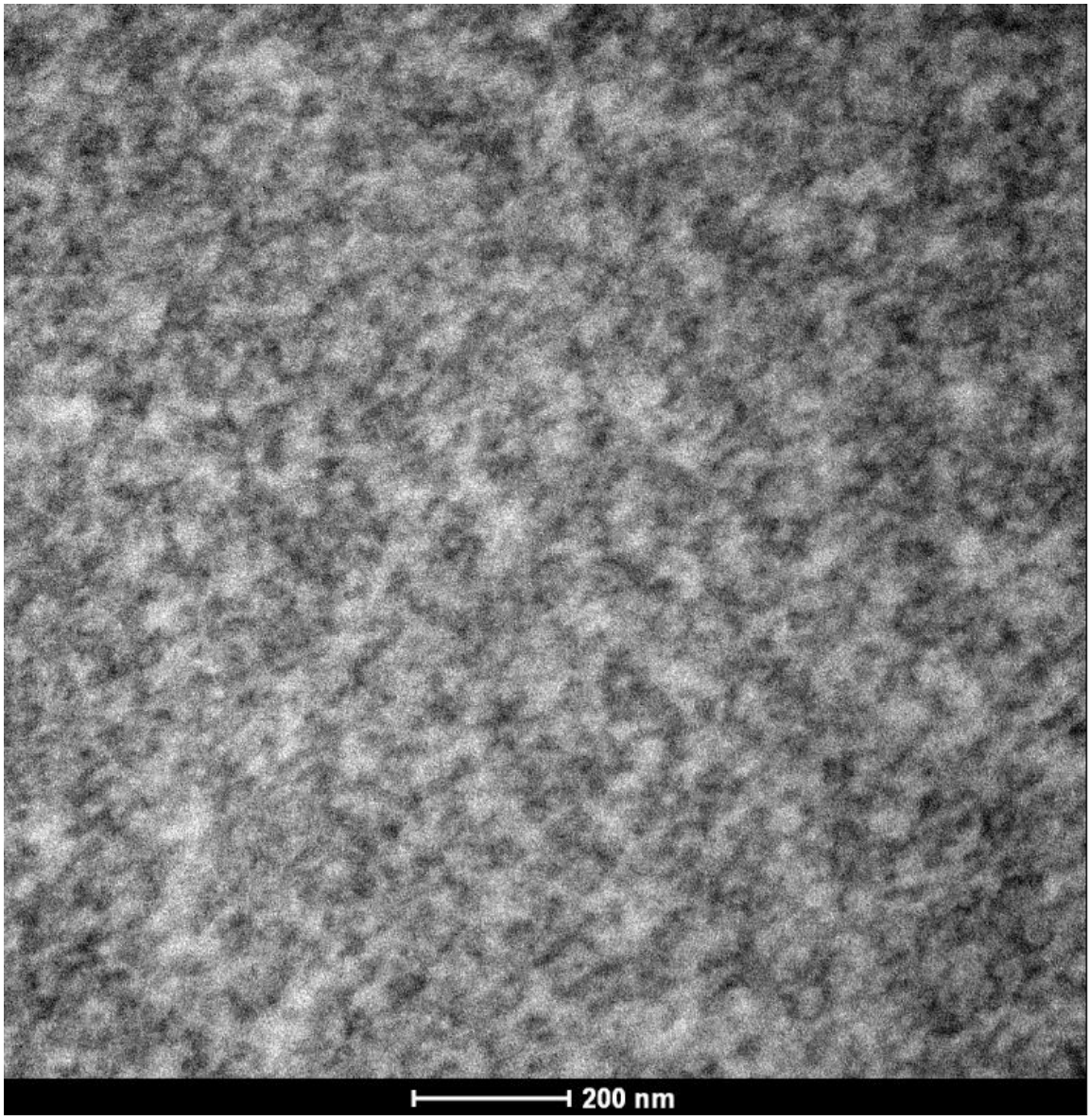

Figure 4.9: TEM image of the pores present in a pad fabricated with solution 300-2.

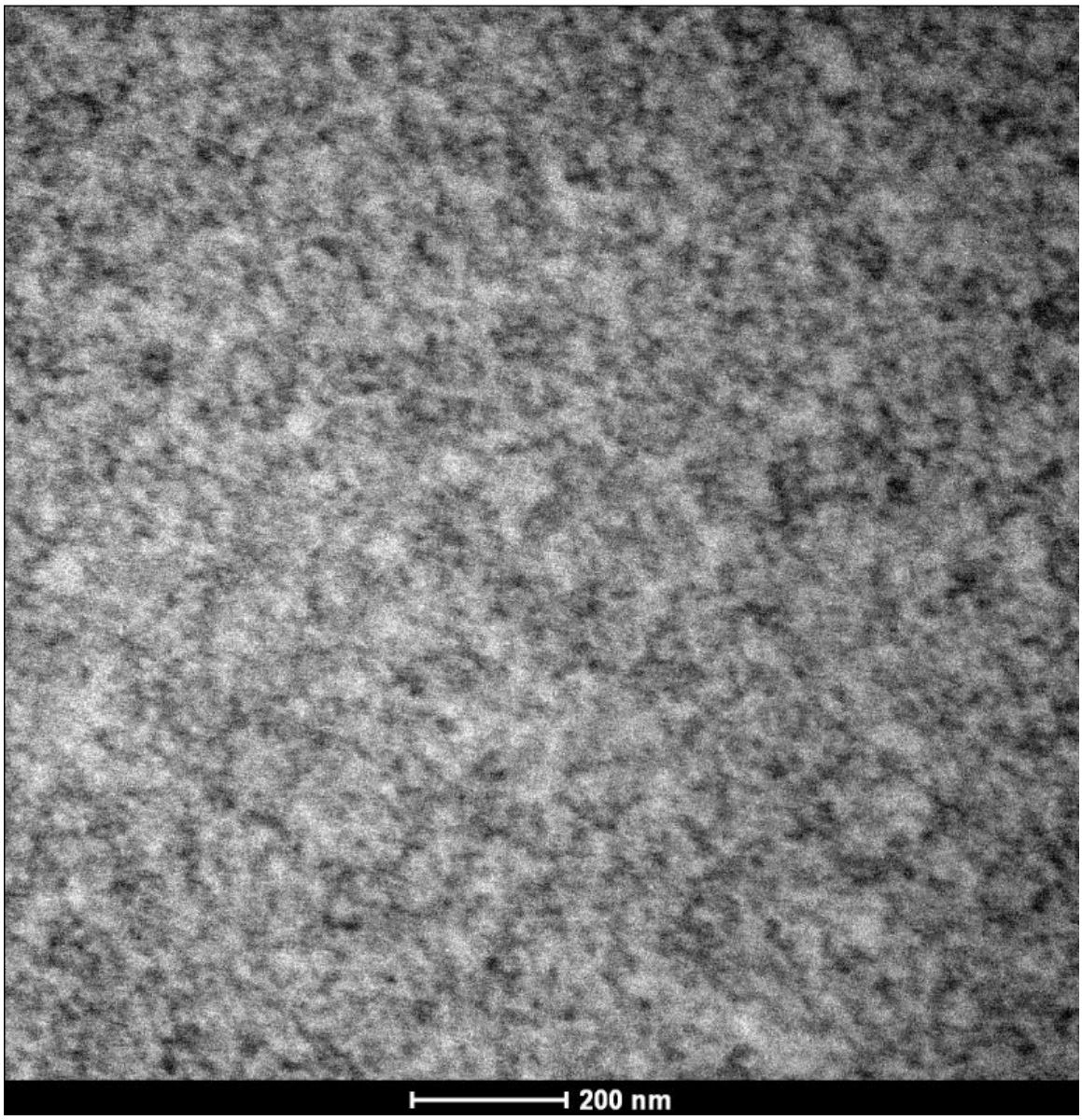

Figure 4.10: TEM image of the pores present in a pad fabricated with solution 300-4.

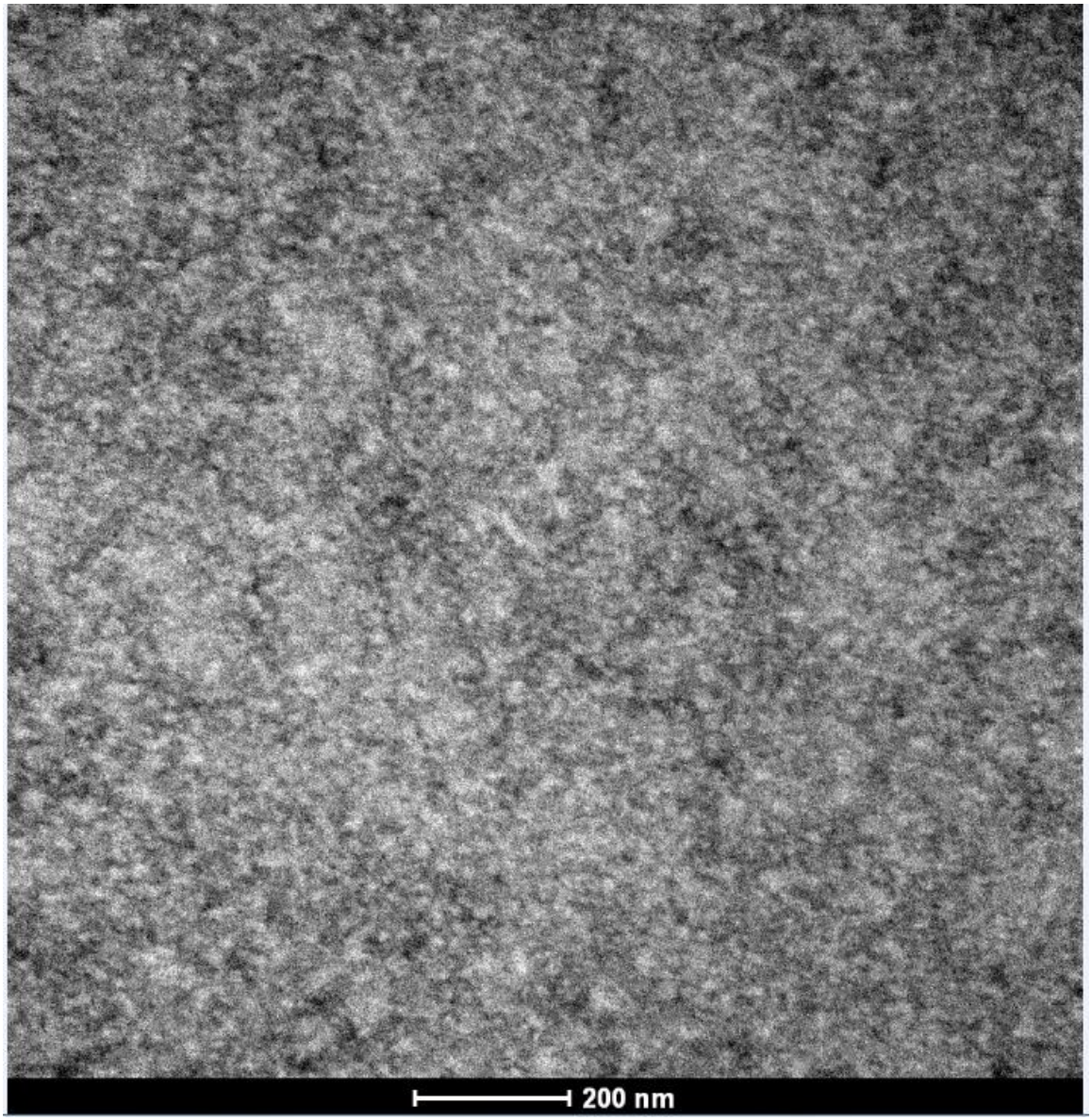

Figure 4.11: TEM image of the pores present in a pad fabricated with solution 300-6.

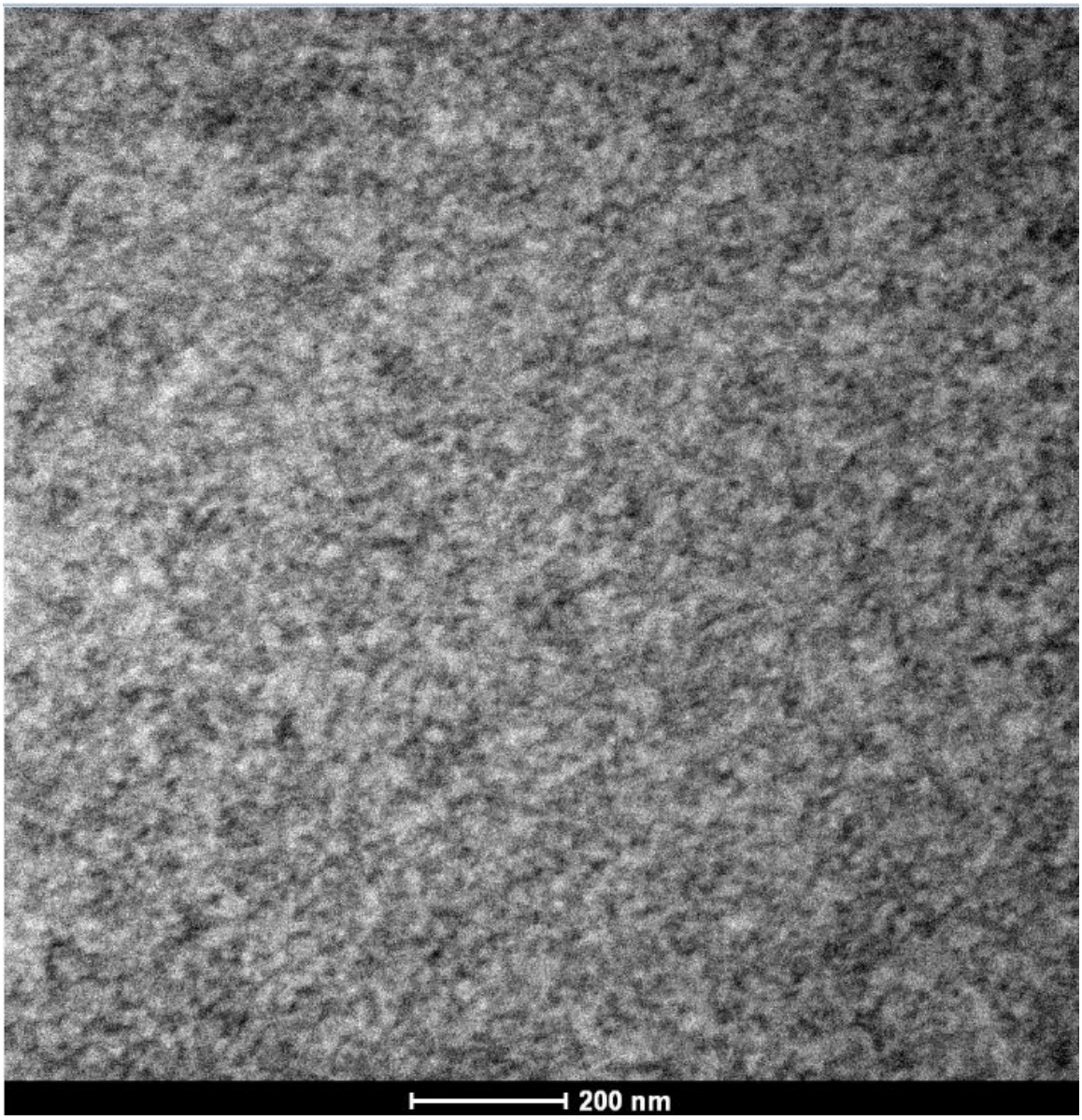

Figure 4.12: TEM image of the pores present in a pad fabricated with solution 300-4+.

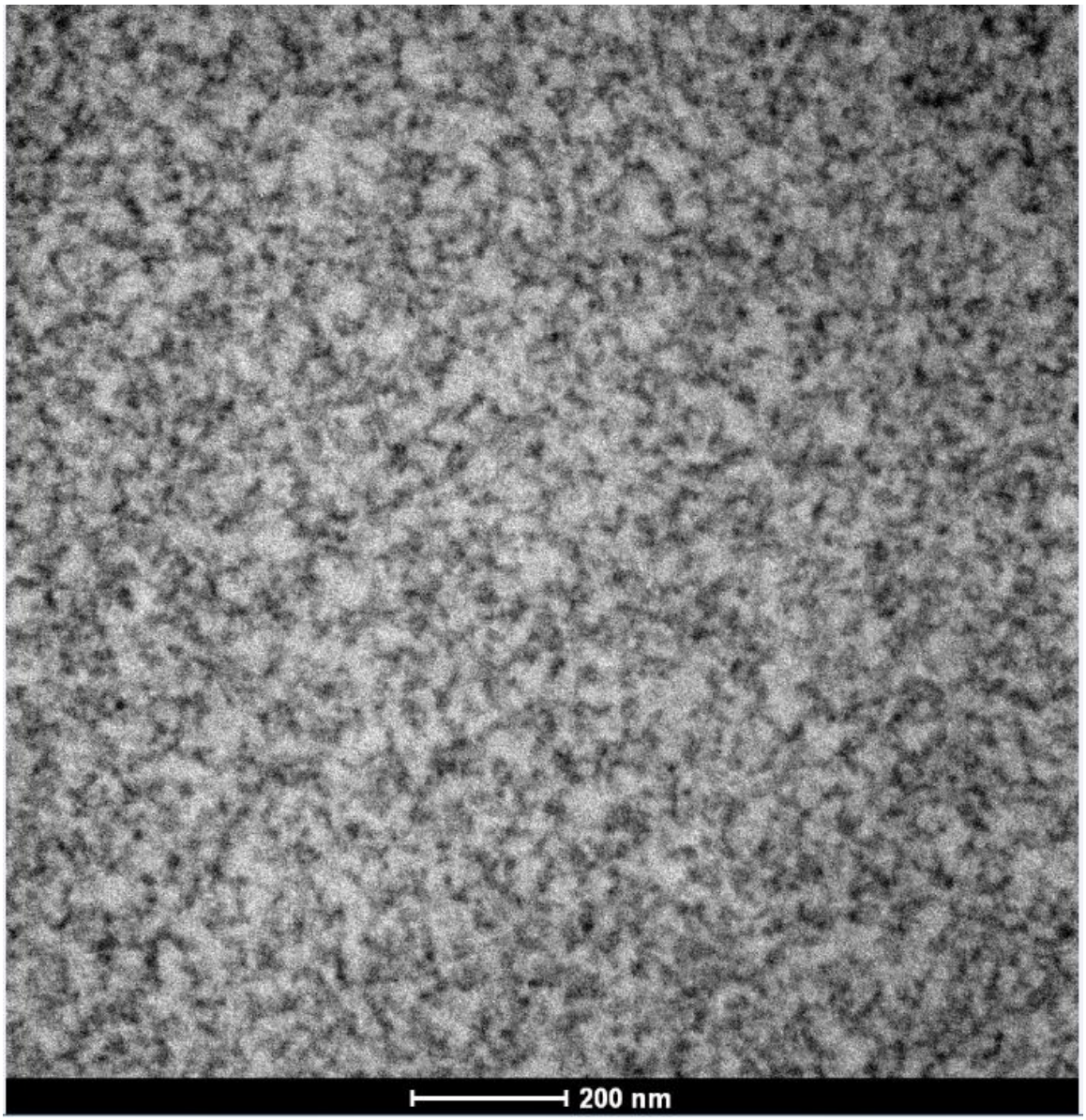

Figure 4.13: TEM image of the pores present in a pad fabricated with solution 60-4+.

Conclusion

This chapter covered the characterization of hydrogel precursor solution and hydrogel μ3D printed materials, using melting point determinations and TEM studies. The melting temperature ranges determined for the gel 60 and gel300 solutions both yielded

linear melting point versus concentration curves that differed based on Bloom number, with the gel60 range being statistically significantly lower than the gel300 range. Due to the linear nature of the curves, these can be used to predict approximate melting temperatures of solutions designed for future applications. Unfortunately, the post fabrication analyses of the hydrogel material did not produce a coherent pattern. While optically the fabricated structures appear to have differing pore sizes that decreased in size with increasing protein content, the analysis did not appear to confirm that trend. It is possible that the method of data analysis is incorrectly chosen for this application, or it is possible that the TEM images are misleading with respect to their true data content. Regardless of explanation, it is clear that this is not a preferred method of characterizing fabrication solution content with respect to porosity and diffusivity at this time. Further investigation may be necessary to elucidate a superior method. Overall, however, both of these studies contribute towards the end goal of optimizing methods to characterize these materials. This process is integral to the design and analysis of research integrating μ3D printing and microbiology.

Chapter 5: Proximity Studies[1,2]

INTRODUCTION

Spatial Organization of Bacterial Aggregates

Pseudomonas aeruginosa, the opportunistic pathogen found in a variety of nosocomial infections in the immune suppressed, is a highly social creature, as mentioned in Chapter 1. It can communicate in a process known as quorum sensing (QS) through a variety of pathways, and two in particular, the *las* and *rhl* systems, are frequently exploited by biologists for their role in increasing cell virulence [25], [27]–[29], [35]. The proteins LasR and RhlR are activated upon binding to their homoserine lactone (HSL) autoinducers: N-3-oxy-dodecanoyl homoserine lactone (3OC12-HSL) and N-butanoyl-L-homoserine lactone (BHL). Once activated they can bind to various *las-rhl* gene boxes on promoters of certain genes responsible for virulence factors [35]. In particular, it has been found that by "knocking out," (a process of replacing or interrupting a sequence of DNA) the "*lasI-rhlI*" gene box, a majority of the virulence factors under the control of QS can be eliminated [35]. Thus, these knockouts, dubbed *ΔlasIΔrhlI* mutants, can be used to assess whether *P. aeruginosa* is able to effectively quorum sense. Furthermore, LasR is also responsible for inducing the expression of a protein called RsaL, which is a repressor of the gene *lasI* [35]. Since LasR must be complexed with 3OC12-HSL to bind the *rsaL* promoter to make the RsaL protein, putting fluorescence indicator genes such as green fluorescent protein (GFP)

[1] S. Darch, O. Simoska, M. Fitzpatrick, J. Barrazaa, K. Stevenson, R. Bonnecazee, J. Shear, and M. Whiteley, "Spatial determinants of quorum signaling in a *Pseudomonas aeruginosa* infection model," *Proceedings of the National Academy of Sciences*, p. 201719317, Apr. 2018.
Author designed and created all protein microstructures used in the study and participated in cell culture.

[2] O. Simoska, M. Sans, M. Fitzpatrick, C. Crittenden, L. Eberlin, J. Shear, K. Stevenson, "Real-time Electrochemical Detection of *Pseudomonas aeruginosa* Phenazine Metabolites using Transparent Carbon Ultramicroelectrode Arrays," *ACS Sensors*, accepted, Oct. 2018.
Author completed all cell culture and UV-Vis readings at the various time points.

downstream of *rsaL* allows for determination of the amount of quorum sensing occurring through the LasR pathway. In short, if more GFP is being produced, it must mean more RsaL is being expressed. Since more RsaL is being expressed, more LasR must be bound to 3OC12-HSL. Thus, it acts as a reporter for QS communication through this pathway [32].

As aforementioned, bacterial communication is dependent not only on the chemical signals themselves, but spatial organization and biogeography [10], [27], [30], [31]. Subsequently, it is important to understand the ways in which bacteria organize themselves and how it influences their ability to quorum sense and cooperate as a community in order to increase population virulence and establish resistant biofilms. However, studying *in vivo* populations can be difficult to achieve, and traditional culture techniques do not allow enough spatial control [15]. With μ3D printing, there is precise control over the localization of cells, and different cell types can be co-cultured and yet isolated from each other by the walls of the hydrogel structure [20]. In order to determine the spatial determinants of *P. aeruginosa* in an environment meant to replicate similar conditions to those of a cystic fibrosis lung, the Whiteley lab developed a synthetic sputum that could be used as a model [32], [119], [120] A group of normal, wild type (*wt*) *P. aeruginosa* called "producers" of signal were trapped and allowed to grow on a coverslip, while *ΔlasIΔrhlI* mutants of *P. aeruginosa* called "responders", which can only respond to quorum sensing molecules but cannot make their own, were grown in the artificial sputum. These aggregates that formed in sputum were then deposited onto the coverslip over the structure, and measurements were made to determine "calling distance," or the distance between the trap and aggregates necessary to produce a response, as shown in Figure 5.1.

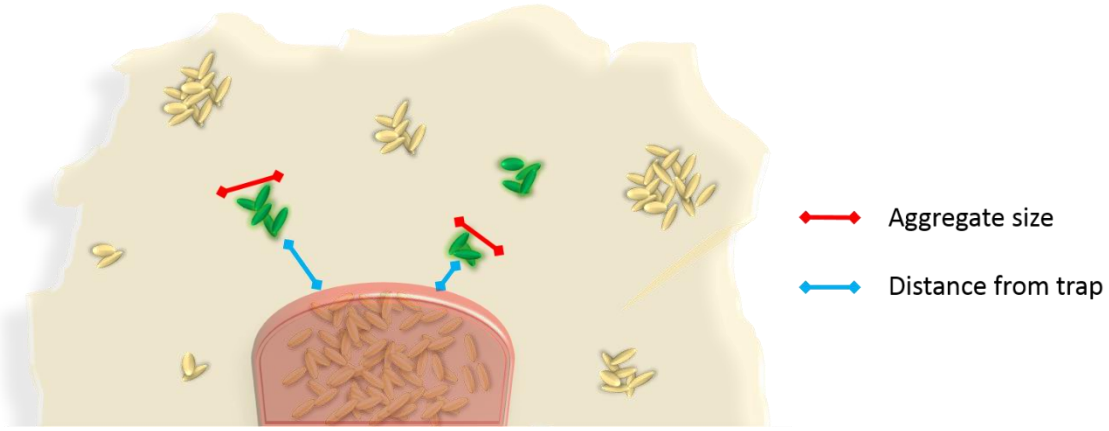

Figure 5.1: Schematic showing trapped "producer" cells in proximity to small "responder" aggregates suspended in artificial sputum. Green indicates that the aggregates are receiving signal from the trapped cells, and this fluorescence can be used to determine aggregate size (red arrows) and distance from the trap (blue arrows). Not to scale.

Electrochemistry and UV-Vis Spectroscopy

As mentioned in Chapter 1, *P. aeruginosa* communicate in a variety of ways, and one result of their QS communication is the production of the biotoxin pyocyanin, a redox active molecule [65]–[67]. Since pyocyanin is a byproduct of the QS pathway, it can be used as an important biomarker for increased virulence in *P. aeruginosa* infections [121]. In order to obtain a quantitative measure of the amount of pyocyanin produced at each stage of bacterial growth, it was necessary to monitor the production over time. Olja Simoska, using the transparent carbon microelectrode arrays (T-CUAs) developed in the Stevenson lab, designed an experiment to obtain quantitative electrochemical measurements of the production of pyocyanin over the course of 48 hours using square wave voltammetry [68], [69], [122]. In order to monitor the stages of growth within the populations being analyzed, the optical density at 600 nm (OD_{600}) was measured at each time point during the analysis. Measuring the OD_{600} with a UV-Vis spectrometer is a

standard practice in the microbiology world for assessing culture growth. While more quantitative measure exist, such as flow cytometry and assessing colony forming units (CFUs), the OD_{600} allows researchers to quickly assess bacterial growth as time progresses. Thus, UV-Vis measurements were taken to accompany the square wave voltammetry response curves over time during the 48 hour period.

EXPERIMENTAL DESIGN AND METHODS

Overview

Dr. Sophie Darch of the Whiteley lab proposed a study to determine how aggregate size and biogeography plays a role in intra- and interaggregate quorum sensing (QS) signaling in cystic fibrosis (CF) lung sputum. Using an *in vitro* model designed by the Whiteley lab to mimic CF sputum, SCFM2, along with *Pseudomonas aeruginosa* PA14 strains altered to only respond to QS signaling molecules, experiments were developed to test these spatial parameters [32]. Figure 5.2 shows the general concept, in which trapped "producer" cells, wild type PA14 (PA14 *wt*), are overlaid with the synthetic sputum mixture inoculated with "responder" cells possessing the plasmid pSEDQS (PA14 QS)- those that cannot produce their own QS signals but can be affected by the signal from the producers. The responder cells constitutively produce mCherry, allowing for determination of total biomass of the aggregates in SCFM2, and upon receiving the QS signal N-3-oxy-dodecanoyl homoserine lactone (3OC12-HSL) from the trapped producer cells can initiate GFP expression. Thus, the presence of activated responder aggregates can be detected, their biomass quantified, and their distance from the producer trap measured using confocal microscopy and software analysis.

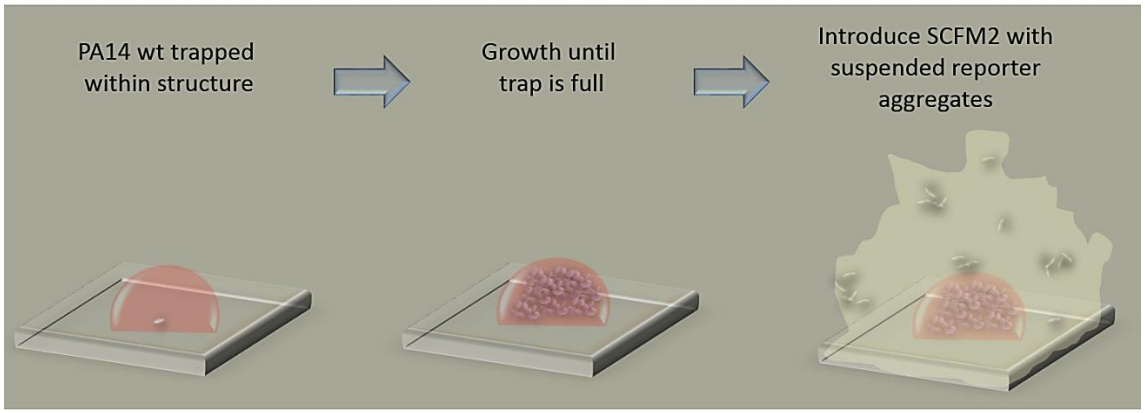

Figure 5.2: Schematic showing the general experimental design in which PA14 *wt* are captured and allowed to grow to a maximum density of 10^3 cells pL^{-1}. Synthetic sputum with PA14 QS aggregates is then introduced on top of the trap, and subsequent analyses can be performed.

While aggregates formed in SCFM2 both naturally and randomly, the producer cell organization process required multiple trap designs, described in detail later in this chapter, in order to replicate various cell cluster sizes. These designs will be presented in the forthcoming sections.

Reagents

Bovine serum albumin (BAH64-1639) was purchased from Equitech-Bio (Kerrville, TX). Gelatin Type A from porcine, 60 Bloom (16560) was acquired from Electron Microscopy Sciences (Hatfield, PA). Rose bengal disodium salt (R323-25) and carbenicillin disodium salt (BP2648-1) were purchased from Fisher BioReagents (Fairlawn, NJ). Tryptic soy broth (R455052), was purchased from Thermo Scientific (Waltham, MA). Tryptic soy agar (R455002) was acquired from Remel (San Diego, CA).

Bacterial Strains, Plasmids, and Culture Conditions

All strains used in these experiments were provided by the Whiteley lab. Over the course of these studies, wild type *Pseudomonas aeruginosa* PA14 (PA14 *wt*) "producers",

and PA14 *ΔlasIΔrhlI* "responders" containing either plasmid pSEDQS (PA14 QS) or pSEDQS2 (PA14 QS2) were used. PA14 *ΔlasIΔrhlI* pSEDQS constitutively expresses mCherry (excitation/emission = 587/610), and a transcriptional fusion of rsaL:*gfp*, allowing for production of green fluorescent protein (GFP) (excitation/emission = 488/510). The second mutant also contains a construct allowing overexpression of *lasR*. All strains were grown from tryptic soy agar (TSA) plate culture and prior to use were shaken overnight at 37 °C at 200 rpm in tryptic soy broth (TSB).

Prior to trapping, 80 µL of overnight culture containing PA14 *wt* was diluted into 4 mL TSB and allowed to shake at 37 °C at 250 rpm for two hours. The optical density at 600 nm (OD_{600}) was then determined and a dilution into TSB was performed such that the final OD_{600} in fabrication solution would be equal to 0.01.

Aggregates of PA14 *ΔlasIΔrhlI* containing either plasmid pSEDQS or pSEDQS2 were formed in SCFM2 by washing aliquots of overnight culture twice and re-suspending in phosphate buffered saline solution (PBS). Cells were inoculated into SCFM2 at an OD_{600} of 0.05 and vortexed to mix. 500 µL of suspended cells were then deposited onto the traps in wells of a chambered coverslip and incubated at 37 °C for 2.5 hours prior to imaging.

Fabrication Conditions

The hydrogel precursor solution was made by sonicating rose bengal (RB) into PBS at a concentration of 5 mM for one hour at 60 °C. 600 µL of this solution was then added to a 1.5 mL centrifuge tube along with enough bovine serum albumin (BSA) and 60 Bloom gelatin type A from porcine (gel60) to reach concentrations of 40 mg mL^{-1} and 150 mg mL^{-1}, respectively, upon the addition of 120 µL of cell culture. Before the addition of the cells the solution was vortexed briefly, placed in a 60 °C oven for 45 minutes, vortexed again, and placed on a 37 °C heated shaker for 3 hours. Finally, cells were added at a final

concentration equaling an OD_{600} of 0.01, the solution was vortexed to mix, and placed on the heated shaker for ten minutes to remove bubbles. 30 µL of this solution were pipetted into four wells of a Labtek 8 well chambered #1 borosilicate coverslip measuring 25 x 57 mm (134534) from Thermo Fisher (Waltham, MA). The droplets were cooled to ~22 °C, before structures were fabricated around cells at a power of ~35 mW at the back aperture, as described in Chapter 1. Following fabrication, each well then received 200 µL of TSB, and the coverslip was placed in the incubator at 37 °C for 45 minutes, then each well was rinsed with fresh 37 °C TSB.

Design of 3D Printed Traps

Previous studies performed by the Shear and Whiteley labs involved the use of 2 pL traps which held ~2000 cells [22]. Thus, the initial design for this study began with a 2 pL dome shaped trap with a 10 µm inner radius and 4 µm walls. However, initial tests of this design did not yield a measurable response from the responder aggregates in the form of detectable GFP signal. Subsequently, a 5 pL trap was designed with an inner radius of 13.5 µm and 4 µm walls. This was successful in eliciting a response from the PA14 QS cells. To see whether an increase in trap size might affect the signaling distance, a 10 and a 20 µm trap were also designed. Following a great deal of troubleshooting, it became necessary to adjust the radii of the structures to ensure effective micro 3D printing and structural integrity. The 10 pL traps were given an inner height (radius) of 20 µm, while the inner radius at the bottom, touching the surface of the coverslip, was 13.5 µm. The 20 pL structures also required a slight design change, with an inner height of 25 µm and inner radius at the coverslip of 17.5 µm. Both the 10 and 20 pL structures were able to maintain the 4 µm walls. All structures are presented in Figure 5.3.

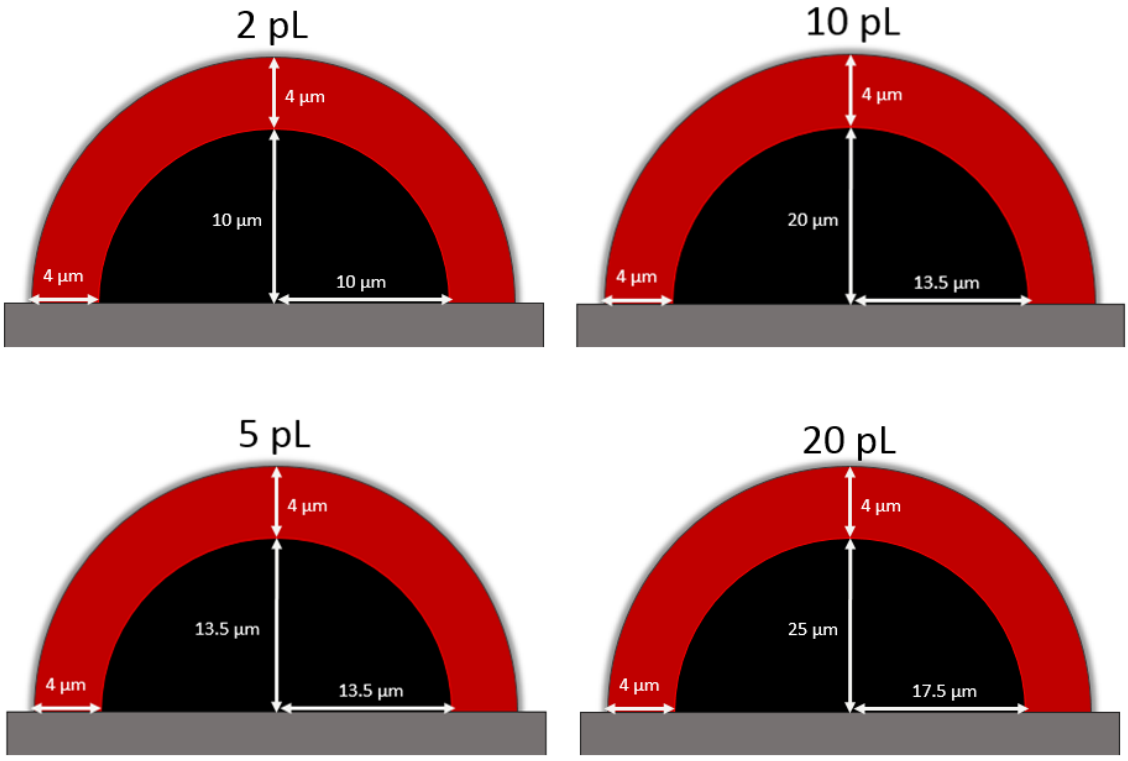

Figure 5.3: Dimensions for the four dome designs used in this study.

Imaging and Image Analysis

Imaging was performed by Dr. Sophie Darch using an LSM 710 Confocal combined with an Elyra S.1 Structured Illumination Super Resolution Microscope and a Plan-Apochromat 63x/1.4 oil/DIC M27 objective from Zeiss (Oberkochen, Germany). Collection was recorded and visualized using the standard Zeiss software, Zen. GFP measurements were made using a 488 nm excitation source and a collection window centered around 509 nm. MCherry measurements were made using a 587 nm excitation source and a collection window centered around 610 nm. Backgrounds were performed for GFP using SCFM2 with both reporter strains in the absence of exogenous signal, and for mCherry with un-inoculated SCFM2. Positive signal was counted as 1.5X the background.

Bitplane AG software Imaris (Zurich, Switzerland) was used to calculate all aggregate biomass and distances between trapped cells and aggregates within the SCFM2.

RESULTS AND DISCUSSION

Determination of the proximity of aggregates of PA14 QS to the trapped PA14 *wt* necessary to induce activation via 3OC12-HSL was investigated by measuring the percent of GFP-producing PA14 QS cells (percent biomass QS+) of the total biomass determined by the production of mCherry. Measurements were made in SCFM2 for all four trap sizes, and aggregate response was recorded in 60 µm intervals from the trap surface. The results are displayed in Figure 5.4. As mentioned previously, the initial design of the 2 pL traps of PA14 *wt* "producers" did not elicit a response in any of the PA14 QS "responder" aggregates, leading to the design of the subsequent trap sizes. For the 5, 10, and 20 pL structures, the distance between the trap and the aggregates resulted in significant differences in response distance. Significantly more cells responded in the 0 – 60 µm range than in the 121 – 180 µm range. Cells did not respond to signal from PA14 *wt* in any trap size in the 180 – 200 µm range, indicating that the trap size itself may not be a factor in "calling distance," despite mean response increasing with trap size.

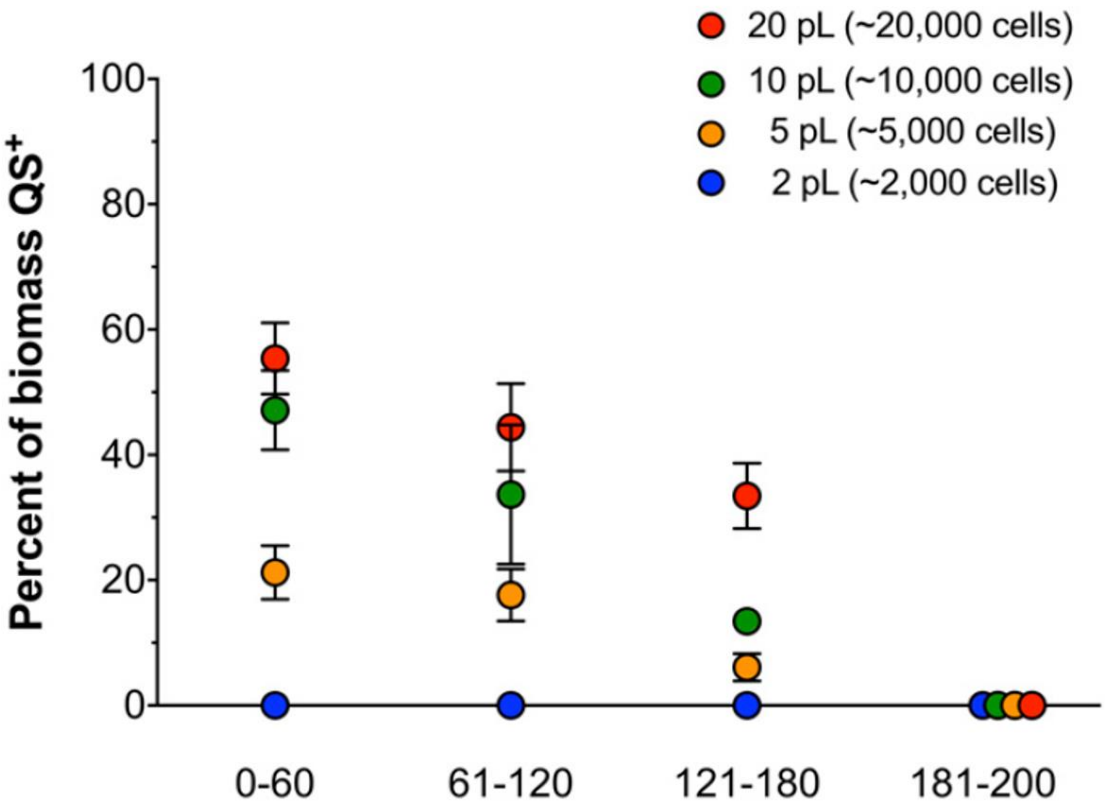

Figure 5.4: PA14 QS response to 3OC12-HSL secreted by PA14 *wt* at various distances from the trap walls, in intervals of 60 µm. Error bars are standard error of the mean. Image courtesy of Dr. Sophie Darch.

Subsequently, to determine what concentrations of signal might be present in each of these 60 µm intervals radiating from the structure surface, aggregates of PA14 QS were suspended in SCFM2, and exogenous 3OC12-HSL was added in concentrations ranging from 0.25 to 10 µM (Figure 5.5). A linear response with an R value of 0.93 was observed in the range between 0.25 and 5 µM, while at 10 µM the response dropped off significantly. This indicates that at this level (far above biological levels which range from 0.5 – 1.0 µM), signal acts to inhibit the response.

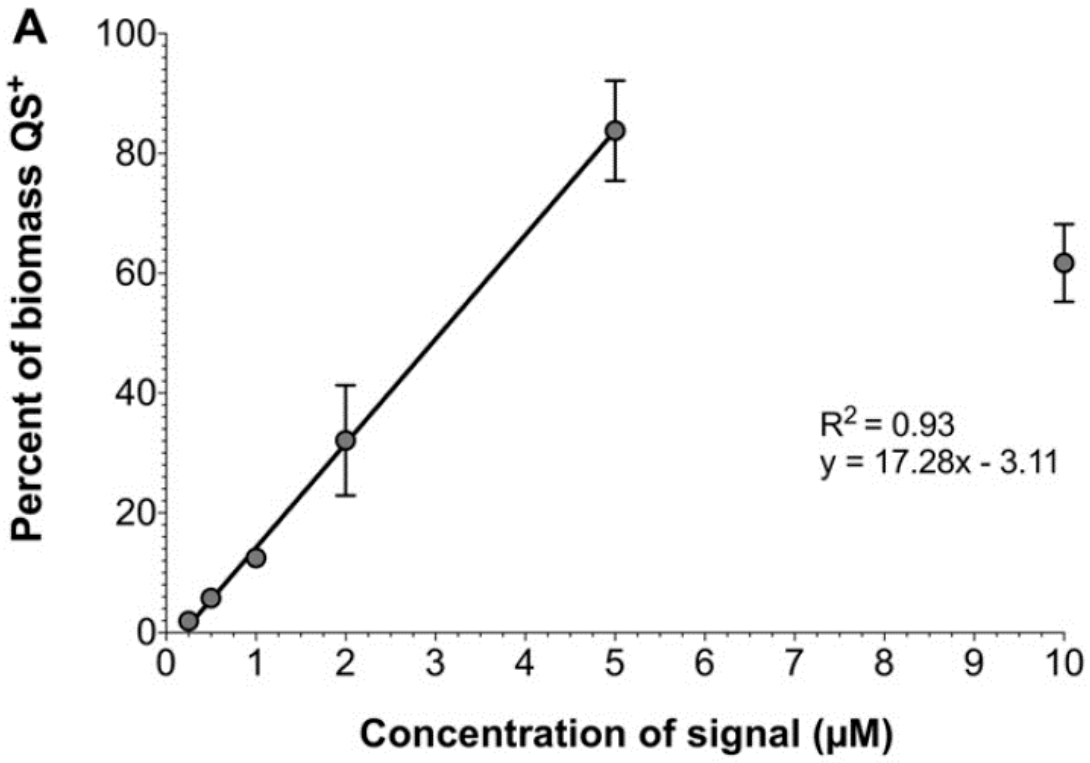

Figure 5.5: PA14 QS response to addition of exogenous 3OC12-HSL over a range of concentrations from 0.25 to 10 µM. Error bars are standard error of the mean. Image courtesy of Dr. Sophie Darch.

The linear response to increases in 3OC12-HSL concentration up to 5 µM (Figure 5.5), combined with the percent biomass response obtained at different distances for the three responding trap sizes (Figure 5.4), provided a means to approximate the 3OC12-HSL concentrations in the various 60 µm regions radiating from the structures. As shown in Figure 5.6, it appears an increasing amount of signal is produced by increasing trap sizes. An increase in cell number is likely the cause, as the 5 pL structures contain only ~5,000 cells, while the 20 pL contain ~20,000. Thus, in the innermost range of 0 – 60 µm, the 5 pL trap produces only ~1.0 µM signal on average, while the 20 pL produces approximately 3 times that amount on average. In the outermost 60 µm where response was detected, 121

– 180 µm, the 5 pL trap decreased to an average of ~0.2 µM, while the 20 pL decreased to only ~1.8 µM. The concentrations for the 2 pL traps were unable to be calculated due to a lack of detectable response. However, Figure 5.5 shows that even a 0.5 µM concentration can induce ~5 % response from PA14 QS aggregates, thus the concentration even in the innermost 60 µm must be below this value.

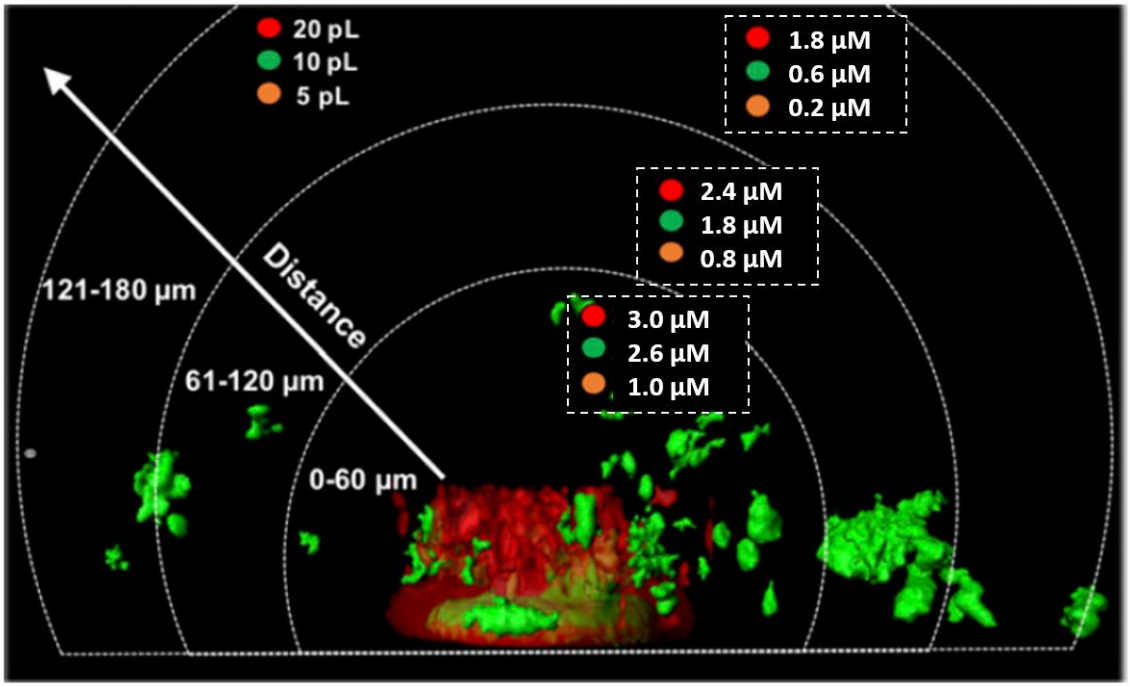

Figure 5.6: Approximate average concentrations of 3OC12-HSL produced by the three large traps of PA14 *wt* at various distances from the trap walls over intervals of 60 µm calculated from the data presented in Figure 5.5 are shown, as indicated by the red, green, and yellow dots. The legend is displayed on the top left. Confocal reconstruction of the trap is shown in red, surrounded by responding cell aggregates in green. Image courtesy of Dr. Sophie Darch.

Lastly, experiments were performed to determine if the 2 pL traps could be induced by an overexpression of *las*R, a gene that encodes the protein lasR, which must bind to 3OC12-HSL before it can bind to the promoter of the *rsa*L gene. Since in these studies,

GFP is also under the control of the promoter for *rsa*L, this would cause an increase in signal binding to lasR, thus manifesting in an increase in GFP production. Thus, using PA14 QS and PA14 QS2 (the variant that overexpresses *las*R) a comparison was made between the percent biomass response of these two "responder" strains to 3OC12-HSL produced by 2 pL structures filled with PA14 *wt*. Figure 5.7 (a) shows that the overexpression of *las*R does result in a response, 20 ± 10 %, from the PA14 QS2 aggregates, while there is still no detectable response from PA14 QS. Furthermore, if exogenous signal is added to an SCFM2 sample with no traps, but containing PA14 QS2, much lower concentrations produce a measurable response, Figure 5.7 (b). This graph correlates the response of PA14 QS2 to the signal produced by the PA14 *wt* 2 pL trap with that of PA14 QS2 in SCFM2 alone, showing that ~20 % response can be obtained from less than a 0.5 µM signal concentration in these aggregates.

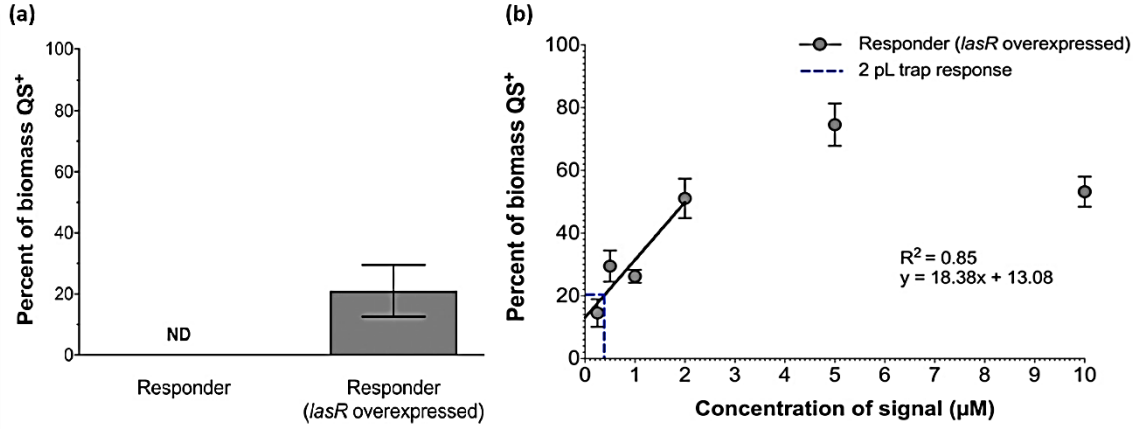

Figure 5.7: Comparison of response from PA14 QS (Responder) and PA14 QS2 (Responder *lasR* overexpressed) aggregates surrounding a 2 pL trap of PA14 *wt* (a). PA14 QS2 response to addition of exogenous 3OC12-HSL over a range of concentrations from 0.25 to 10 µM is shown in (b). The dashed line reflects the amount of response observed from PA14 QS2 in (a). Error bars are standard error of the mean. Image courtesy of Dr. Sophie Darch.

FURTHER STUDIES

Overview

Olja Simoska devised a novel experiment, using the same strains involved in the proximity studies, to detect pyocyanin production over time produced by the strains of bacteria involved in these studies using transparent carbon ultramicroelectrode arrays (T-CUAs) previously developed in the Stevenson lab [68], [69], [122]To complement the study, and to monitor the stages of growth over time, it was decided that the quantitative electrochemical measurements would be performed in tandem with optical density measurements of the cells. It is standard practice in microbiology to assess bacterial growth using a measure referred to as "OD_{600}," which refers to the ultraviolet – visible spectroscopy (UV-Vis) absorption value of a sample of cell culture measured at 600 nm. All trials were performed over the course of 48 hours, with t = 0 representing the two hour mark post-dilution from overnight stock. Cells were diluted in either Luria broth or tryptic soy broth, and on separate days, two of the strains used in the proximity studies were tested in triplicate using each technique, in each of two growth media. The following describes the data collection for the optical density of the cells at 600 nm using (UV-Vis).

Reagents

Tryptic soy broth (R455052), was purchased from Thermo Scientific (Waltham, MA). Tryptic soy agar (R455002) was acquired from Remel (San Diego, CA). Luria broth, Lennox (61272-5000) was purchased from Acros Organics (Geel, Belgium). Carbenicillin disodium salt (BP2648-1) was obtained from Fisher BioReagents (Fairlawn, NJ).

Bacterial Strains, Plasmids and Culture Conditions

The two strains used in these experiments were provided by the Whiteley lab. Both wild type *Pseudomonas aeruginosa* PA14 carrying the plasmid pMRP9-1 (PA14 *wt*), and PA14 *ΔlasIΔrhlI* containing the plasmid pSEDQS (PA14 QS) were used. PA14 *ΔlasIΔrhlI* pSEDQS contains a transcriptional fusion of rsaL:*gfp* and constitutively expresses mCherry while the pMRP9-1 plasmid in the wild type constitutively expresses green fluorescent protein GFP. All strains were grown from TSA plate culture containing 10 μg mL^{-1} to maintain the plasmids. Prior to use, cells were inoculated into a volume of 75 mL of either TSB or LB and shaken overnight at 37 °C at 188 rpm in upright 75 cm^2 CellTreat tissue culture flasks (229341) from Pepperell, MA. The following morning the OD_{600} was determined and dilutions into two fresh 250 mL flasks each of TSB and LB, respectively, was performed such that the resulting OD_{600} would be 0.15 initially with a final volume of 125 mL. These were allowed to shake at 37 °C at 188 rpm for two hours, the point which was designated t = 0, at mid-logarithmic phase. At this point, measurements began for both the electrochemical portion and the UV-Vis determinations.

UV-Vis Results and Discussion

All results obtained from the electrochemical portion of these experiments have been reported by Olja Simoska, et al [122]. OD_{600} values were obtained using an Agilent 8453 UV-Vis spectrophotometer (Santa Clara, CA).

The OD_{600} results over the period of 48 hours for PA14 *wt* in TSB and LB can be observed in Figure 5.8 and 5.9, and those for PA14 QS can be observed in Figure 5.10 and 5.11. It should be noted that typically OD values above 1.00 are not reported due to detector saturation [123]. However, in biological samples this is not always the case [124]. In all graphs presented here, the OD_{600} values follow a logarithmic scale to approximately 24

hours with R^2 values above 0.95. This is typical, considering in batch culture cells do not often reach a death phase very quickly due to plentiful nutrients. It is also observed that following approximately the 24 hour measurements the OD_{600} values, while replicable amongst the individual triplicate cuvettes, vary significantly. It is likely that this fluctuation is due to the nature of stationary phase cells, particularly *Pseudomonas aeruginosa*, which is known to excrete large amounts of extracellular matrix. This can cause cell clumping which can affect the spectrophotometric readings as well.

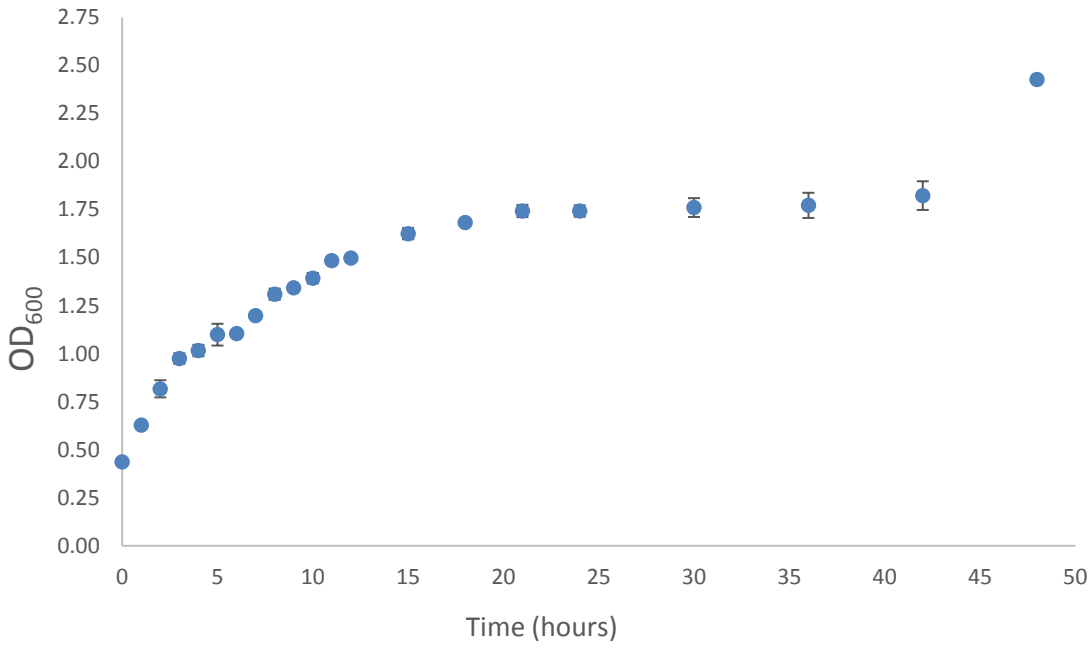

Figure 5.8: OD_{600} of PA14 *wt* in TSB over a 48 hour period. $R^2 = 0.99$ for a logarithmic fit up to 24 hours, $y = 0.42 \ln x + 0.37$. Error bars are standard deviation, n = 3.

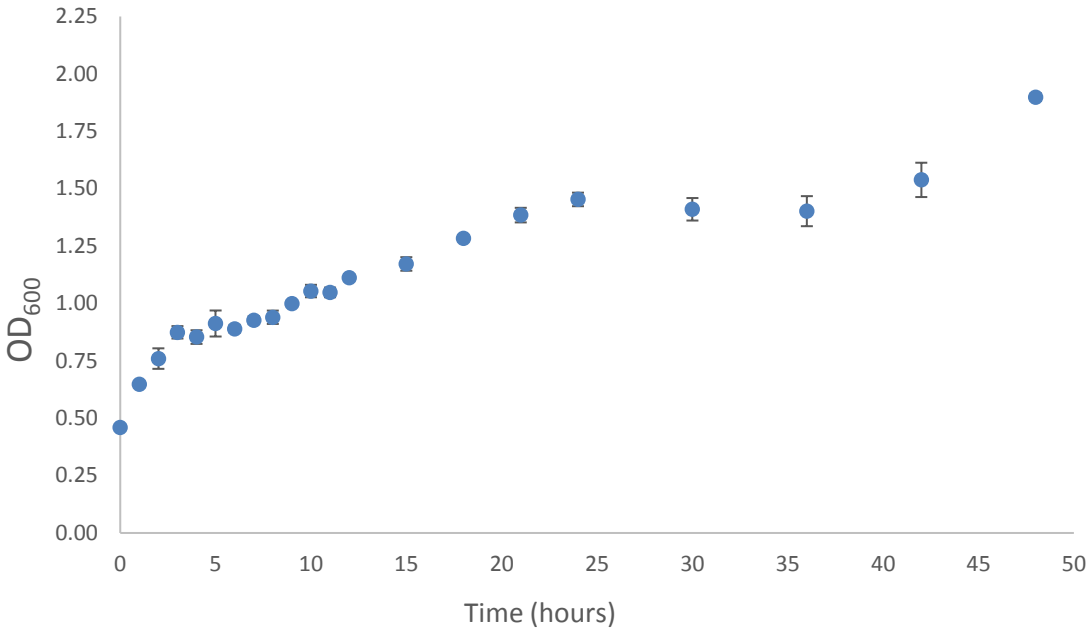

Figure 5.9: OD_{600} of PA14 *wt* in LB over a 48 hour period. $R^2 = 0.95$ for a logarithmic fit up to 24 hours, $y = 0.27 \ln x + 0.42$. Error bars are standard deviation, , n = 3.

The plotted OD_{600} values show that for PA14 *wt* in TSB and LB, both approach stationary phase below 2.0, with cells cultured in TSB plateauing around $OD_{600} = 1.74$ and in LB around $OD_{600} = 1.45$. Following the plateau both appear to jump somewhere between hours 40 and 48, but again it is difficult to discern if this is an artifact or a true representation given the extremely high OD_{600}.

The OD_{600} values for graphs 5.10 and 5.11 show that for PA14 QS in TSB and LB, both approach stationary phase closer to 2.0, with cells cultured in TSB plateauing around $OD_{600} = 1.95$ and in LB around $OD_{600} = 1.91$. Following their plateaus, the TSB cultured cells appear to rise slightly around hour 37 and then fall between 40 and 48, while the LB cultured cells appear to fall near hour 32 and then jump somewhere between hours 40 and 48. However, again, the OD_{600} values are not within an accurately measurable range, and thus may not reflect the true live cell density.

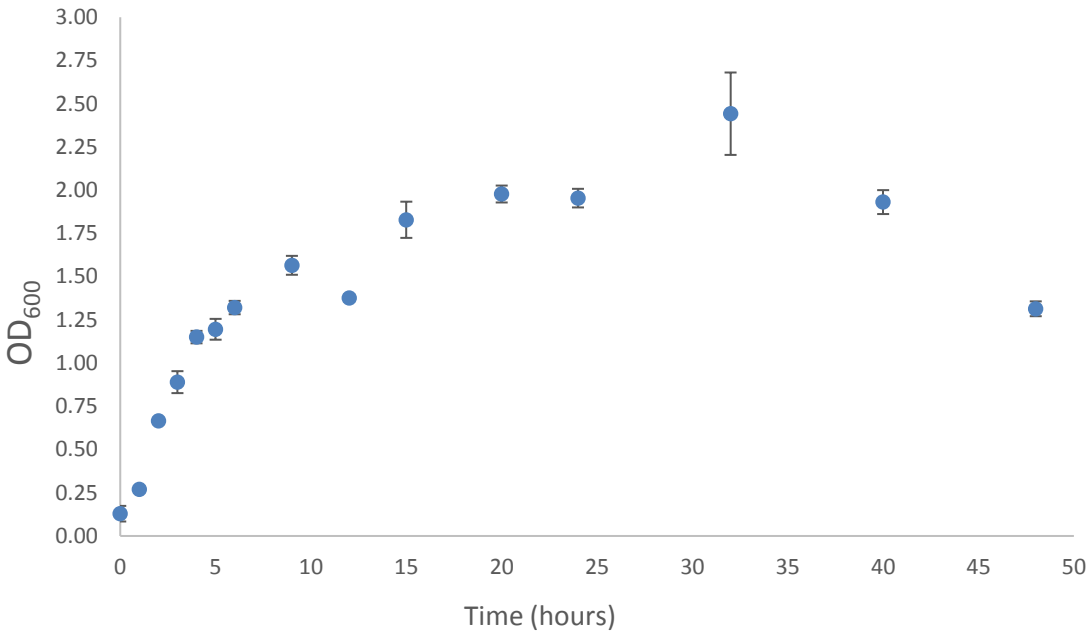

Figure 5.10: OD_{600} of PA14 QS in TSB over a 48 hour period. $R^2 = 0.96$ for a logarithmic fit up to 24 hours, $y = 0.70 \ln x - 0.03$. Error bars are standard deviation, n = 3.

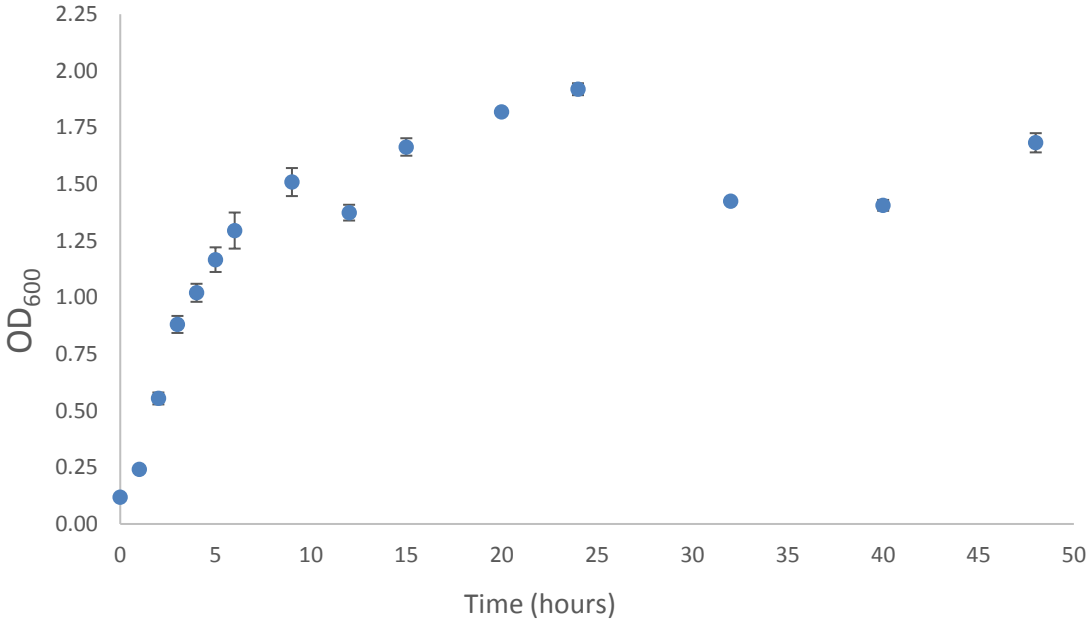

Figure 5.11: OD_{600} of PA14 QS in LB over a 48 hour period. $R^2 = 0.97$ for a logarithmic fit up to 24 hours, $y = 0.68 \ln x - 0.05$. Error bars are standard deviation, n = 3.

The discrepancy between the growth curves for PA14 *wt* and PA14 QS is noteworthy, as it was necessary to remove the autoinduction (signal amplification) loop in the PA14 QS cells for the spatial determination studies [32]. Although this theoretically should not affect cell growth, multiple experiments were performed comparing the two cell types and a clear difference became apparent. While the wild type cells had an initial slope of 0.42 in TSB and 0.27 in LB, the QS cells possessed a slope of 0.70 and 0.68, respectively, despite the *wt* cells plateauing at a lower value. This indicates that the PA14 QS grew significantly slower during the exponential phase than PA14 *wt*, but achieved a much higher final cell density in stationary phase. It is possible that the removal of the primary autoinduction loop caused the cells to remain in exponential phase longer with a slower metabolic rate due to the lack of activation of this loop. This metabolic change could

also explain how they managed to reach a much higher density than their wild type counterpart.

There is also a noticeable difference in the growth rates for the two types of media, with cells in LB initially growing at a faster rate than those in TSB, as evidenced by their lower slope values for both cell types. However, cells grown in TSB reach higher overall densities than those in LB. As mentioned previously, the cells plateaued in TSB at ~1.74 (*wt*) and ~1.95 (QS) and in LB at ~1.45 (*wt*) and ~1.91 (QS). This is likely due to the increased amount of available nutrients in TSB versus LB, and the cells' ability to metabolize them differently to maintain a higher steady state [125].

CONCLUSION

This chapter covered collaborative studies with Dr. Sophie Darch of the Whiteley group involving the determination of spatial organization and calling distance in *P. aeruginosa* using a synthetic sputum model and μ3D printing, along with a UV-Vis based monitor of growth stages to complement an electrochemical study designed by Olja Simoska of the Stevenson and Shear groups [32], [122]. Multiple trap designs from 2 to 20 pL volumes were created to mimic microbial populations of different sizes, and synthetic sputum containing naturally formed aggregates was deposited on top. Then, the QS knockout "responder" cells were monitored to determine at what distance they were from the trap "producers" to elicit a detectable response. No response was detected from aggregates with the smallest trap. For the larger three, it was determined that while more aggregates responded in the 0 – 60 μm range than in the 121 – 180 μm range, this was not sufficient to assert that increasing trap size meant a further calling distance, as the 181 – 200 μm range yielded no detectable results for any trap size. A response curve was then developed by adding successive amounts of external signal to the aggregates in the sputum,

and a linear relationship was found between 0.25 μM to 5 μM. This was subsequently used to calculate approximate concentrations of extracellular signal produced by the three largest traps over the 60 μm intervals, and it was extrapolated that the concentration of signal produced by the smallest trap must be less than 0.5 μM. Finally, an experiment was done to see if a response could be obtained from the 2 pL trap producers by increasing the ability of the aggregates in sputum to bind to the signal produced. This yielded a significant increase in response from the aggregates when exposed to signal produced by the small traps.

The OD_{600} values obtained alongside the electrochemical measurements revealed that the QS knockout, or responder, cells grew significantly slower during exponential phase than their wild type counterparts, but achieved a much higher final density. This indicates that there is at least a slight metabolic difference between the two strains. In addition, all cells grown in LB grew significantly faster initially but reached lower final densities than those grown in TSB, indicating that while LB may provide simpler more easily metabolized energy sources initially, TSB is richer in total energy sources and enables continued growth after cells in LB have expended the available nutrients. Both the spatial determination and growth phase monitoring studies provide important information about sociomicrobiology and biogeography. Cellular communication, spatial organization, and nutrient availability all contribute towards the development of cooperative microcolonies which can initiate biofilm formation and contribute to pathogenicity.

Chapter 6: DESI-MS Studies

INTRODUCTION

Intact biological samples have historically presented a host of issues with mass spectrometry (MS), but with the advent of techniques such as direct analysis in real time (DART) and desorption electrospray ionization (DESI), a shift has occurred [86], [87], [91], [126]. It is now possible to analyze even large molecules from biological samples, in a process called "ambient MS." Ambient MS eliminates the need for ionization under high vacuum pressure, instead enabling analysis directly from the sample in the open air of the laboratory. It also eliminates extensive sample prep which can distort results, and subsequently time consuming steps for the researcher [86], [127], [128]. The simplicity afforded by this technique however, does not come with a loss in analytical power. In fact, not only can these ionization techniques provide a relatively biological sample-friendly platform that operates on the "3 S Trademark of MS" (selectivity, sensitivity, and speed), but can also provide spatial information as well [129], [130]. DESI-MS is highly compatible with MS imaging, allowing for the pinpointing of sample regions where certain compounds are being detected, while also providing information with respect to their relative abundance [89]. These qualities make this technique very appealing for the study of bacterial colonies, especially in conjunction with μ3D printing. While μ3D printing of bacteria such as *P. aeruginosa* can afford precise spatial organization of colonies, DESI-MS imaging can analyze the cellular products, including metabolites and signaling molecules, with the benefit of showing their distribution in the sample. Previously, secondary ion mass spectrometry (SIMS) has been used to identify a number of signaling molecules in the *P. aeruginosa* quinolone based QS system [80], [131]. 2-heptyl-3-hydroxy-4-quinolone, commonly referred to as PQS, is chemically unique from the acyl

homoserine lactone (AHL) signals that bind to regulators such as LasR, mentioned in Chapter 5. PQS and its precursors, such as 2-heptyl-4-quinoline (HHQ) and others, and its derivatives can also be used as biomarkers for increased cell virulence and biofilm formation [36], [132], [133]. Using DESI-MS imaging, these molecules can not only be identified, but their abundance and spatial distribution can be analyzed as well. The studies presented here are a first step to integrating the spatial control of μ3D printing with the imaging capabilities of DESI-MS imaging in order to better understand the biogeography of *P. aeruginosa* communities.

EXPERIMENTAL DESIGN AND METHODS

All desorption electrospray ionization mass spectrometry imaging (DESI-MSI) measurements were carried out by Marta Sans of the Eberlin lab, and all spectra and DESI-MS images are used with her permission. DESI-MSI experiments were carried out using a Prosalia 2D Omni Spray (Indianapolis, IN) coupled to a Thermo Scientific LTQ-Orbitrap Elite (Waltham, MA). A hybrid mass spectrometer, which allows for tandem MS experiments using both collision-induced dissociation (CID) and higher-energy collision-induced dissociation (HCD) methods, was operated from *m/z* 100 to 1000 in both the negative and positive ion modes with high mass accuracy (<5 ppm mass error) and resolution (60,000 resolving power). Negative ion mode analysis was performed with a 1:1 (v/v) mixture of acetonitrile (ACN) and dimethylformamide (DMF), at a flow rate of 2 μL min^{-1}. For positive ion mode analysis pure ACN was used at a flow rate of 5 μL min^{-1}. The N_2 pressure was set to 185 psi. All ion images were assembled using Biomap software. Preliminary experiments were performed to ensure no interfering signal was present from the tryptic soy broth media or hydrogel traps.

Reagents

Bovine serum albumin (BAH64-1639) was purchased from Equitech-Bio (Kerrville, TX). Gelatin Type A from porcine, 60 Bloom (16560) was acquired from Electron Microscopy Sciences (Hatfield, PA). Rose bengal disodium salt (R323-25) and carbenicillin disodium salt (BP2648-1) were purchased from Fisher BioReagents (Fairlawn, NJ). Tryptic soy broth (R455052) was obtained from Thermo Scientific (Waltham, MA). Tryptic soy agar (R455002) was acquired from Remel (San Diego, CA).

Bacterial Strains, Plasmids, and Culture Conditions

Experiments were conducted using the constitutive green fluorescent protein (GFP) expressing *Pseudomonas aeruginosa* strain PA01 transfected with the *gfp* containing plasmid pMRP9-1 and a carbenicillin resistance marker. A concentration of 10 μg mL^{-1} carbenicillin was used to maintain the plasmid in both tryptic soy agar (TSA) and tryptic soy broth (TSB). Liquid cultures were grown in 4 mL of TSB in standard culture tubes started from plate culture. These tubes were aerated in a 37 °C incubator at a rate of 250 rpm overnight until stationary phase was reached. Cultures were then either used directly at this point without dilution, or 200 μL of this culture were diluted into 4 mL TSB and returned to the incubator shaker for two hours to reach mid-logarithmic phase. These logarithmic phase cells were either analyzed in their media or diluted at a 1:5 ratio into fabrication solution to be trapped.

Analysis of Cell Cultures on Slides

Preliminary experiments were performed analyzing cell droplets deposited onto glass slides. Approximately 10 – 20 μL of cells in TSB, either from overnight culture in stationary phase or in exponential phase after the two hour mark following dilution, were

deposited directly onto the glass slide and allowed to dry for 30 to 90 minutes in a fume hood. A schematic and image are shown in Figure 6.1.

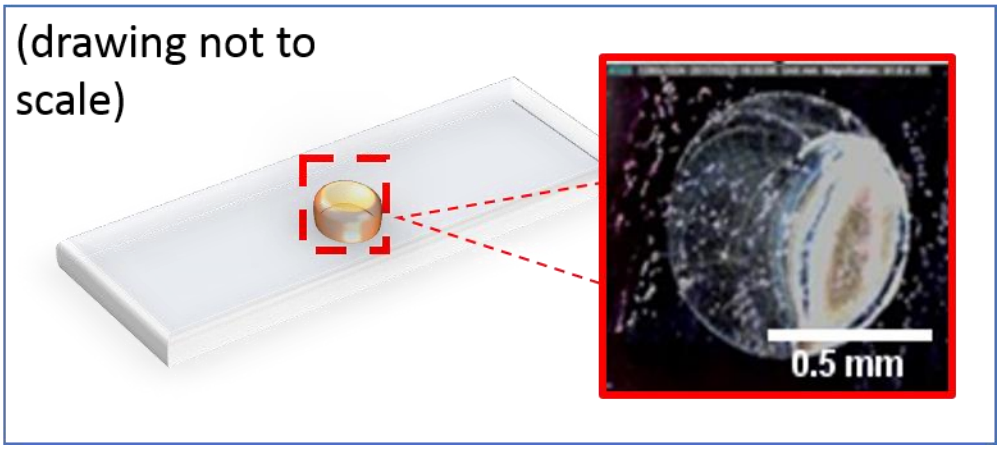

Figure 6.1: Illustration of the cell droplet placed on the glass slide, and a bright field image of the cells (inset) following the drying period.

Fabrication Conditions

The hydrogel fabrication solution was created by first solubilizing rose bengal (RB) into phosphate buffered saline (PBS) at a concentration of 5 mM in a heated sonicator for one hour at 60 ºC. Bovine serum albumin (BSA) and 60 Bloom gelatin Type A from porcine (gel60) were then added to 440 µL of this solution such that a subsequent addition of 60 µL would result in final concentrations of 40 mg mL^{-1} and 150 mg mL^{-1}, respectively. This was vortexed for a few seconds in a 1.5 mL Eppendorf tube and placed in an oven set to 60 ºC for thirty minutes and vortexed briefly again. The solution was then placed on a heated shaker at 37 ºC for three hours. At this point, 60 µL of exponential phase cells in TSB were added, the solution was vortexed to distribute the cells evenly, then returned to the heated shaker for ten minutes to allow the bubbles caused by vortexing to dissipate.

A 30 μL droplet was pipetted onto a #1 borosilicate coverslip secured in a Teflon sample well and allowed to cool ~22 ºC, to immobilize the cells. Cells were then located within the solution using an Olympus UPlanApo 100x/1.35 NA objective (Tokyo, Japan) on an inverted Zeiss Axiovert 100 microscope (Oberkochen, Germany). Free-standing protein microstructures were then created around cells as described in Chapter 1, using a step size of 0.5 μM and a laser power of ~35 mW at the back aperture. The well was then filled with TSB and heated to 37 ºC for 45 minutes before rinsing with fresh TSB. The cells were allowed to grow inside the structures at RT for approximately 18 hours or until the traps were full. Prior to analysis, the coverslip containing the structures filled with cells was placed on a glass slide and dried for 30 minutes.

Design of 3D Printed Traps

Initially, to best coordinate with the mass spectrometry parameters frequently used in the Eberlin lab, in particular a 200 μm spot size, a rectangular protein trap measuring 500 x 200 μm was designed, with an inner chamber 5 μm in height, and a roof thickness of 7 μm. This trap also included 3 μm posts to ensure stability. Due to the limited fabrication area determined by the objective and laser focal diameter, it was necessary to "stitch" this structure, quilting individual pieces together with slight overlap at the edges to facilitate structural integrity. Figure 6.2 illustrates the design of the inside of the trap, with lines delineating where individual pieces would be stitched together. The roof of all pieces was comprised of a solid square covering the entirety of the inner cavity.

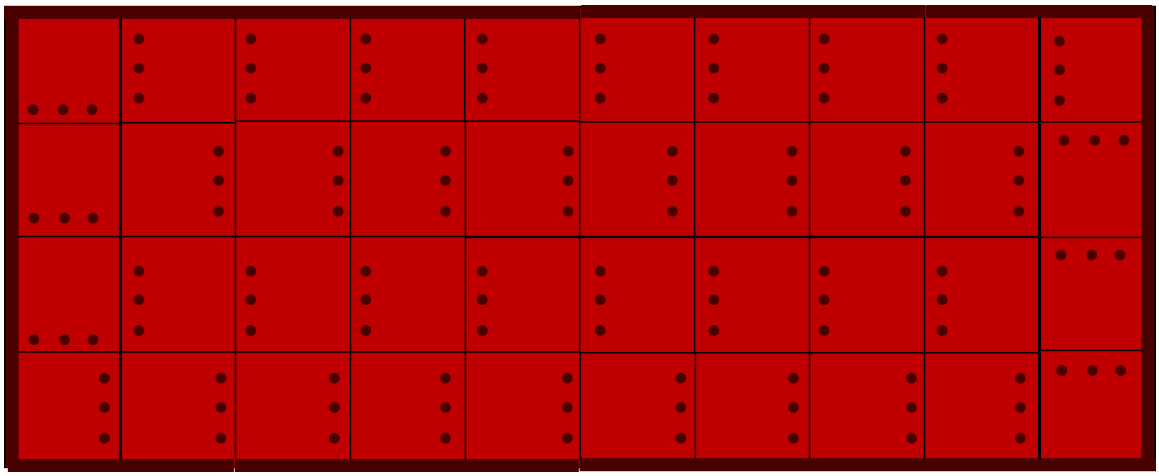

Figure 6.2: Preliminary design of trap interior for 500 x 200 µm structure, black lines indicate areas of stitching, darker red indicates posts and walls.

However, it soon became clear that this design was both time consuming and yielded poor results due to the amount of stitching necessary. All structures created from this design collapsed or ripped during rinsing due to stress on the seams, allowing cells to escape and thus negating the usefulness of their large size. Subsequently, a smaller stitched square structure design was adopted, measuring approximately 100 µm per side. These stitched squares were then fabricated in an array of two by five, yielding final dimensions of 200 x 500 µm, as seen in Figure 6.3.

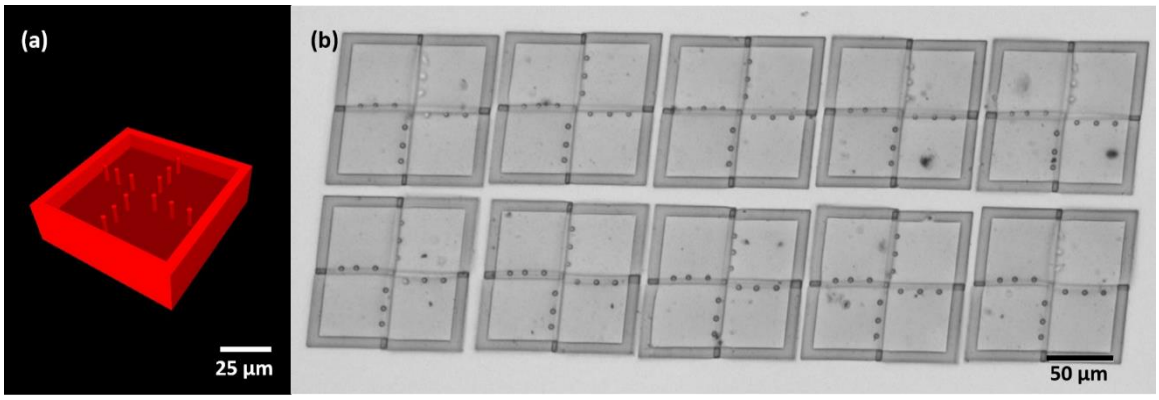

Figure 6.3: 3D rendering of the single stitched square design, inverted to show the interior (a) and a bright field image of the 200 x 500 µm array (b).

This array provided ample area for analysis while maintaining the structural integrity required to keep the cells contained. Subsequent designs will be discussed in the Proposed Future Studies section.

RESULTS AND DISCUSSION

Initial studies involving stationary phase cell droplets were performed in positive ion mode, and *Pseudomonas* quinolone signal (PQS) and many of its analogs were identified based on the respective *m/z* values, as delineated in Table 6.1.

Attribution	Molecular Formula	Detected m/z	Mass Error (ppm)	Exact Mass (daltons)
HHQ	$C_{16}H_{22}ON$	244.1686	4.1	244.1696
PQS/HQNO	$C_{16}H_{22}O_2N$	260.1637	3.1	360.1645
C9:1-NHQ	$C_{18}H_{24}ON$	270.1843	3.3	270.1852
NHQ	$C_{18}H_{26}ON$	272.2000	3.3	272.2009
C9:1-NQNO	$C_{18}H_{24}O_2N$	286.1793	3.1	286.1802
C9-PQS/C9-NQNO	$C_{18}H_{26}O_2N$	288.1948	3.5	288.1958
C11:1-UHQ	$C_20H_{28}ON$	298.2154	3.7	298.2165

Table 6.1: Molecules identified in stationary phase cell droplet in positive ion mode. Table adapted from data provided by Marta Sans.

Figure 6.4 provides a comparison of the dried droplet to an arbitrary DESI map of intensity for the same droplet for reference purposes. It can be observed that the molecule in question is concentrated significantly in the top left portion of the area indicated by the dashed red lines. Additionally, outside of the dashed red line in the bright field image, there are very few cells, and this is reflected in the signal obtained for the particular extracellular molecule in the DESI-MS image.

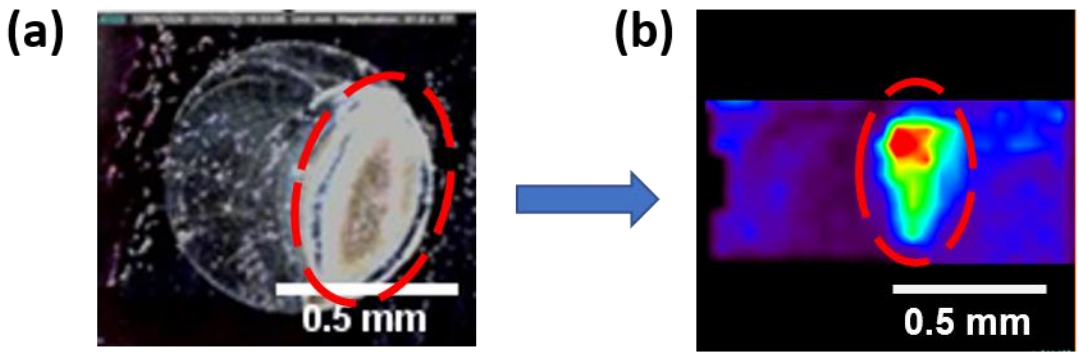

Figure 6.4: Bright field image of the dried cell droplet (a) and arbitrary intensity map from DESI-MS imaging of the same droplet (b). Dashed red line delineates edge of the cell clump and indicates how the image rotations correspond. Courtesy of Marta Sans.

Figure 6.5 presents an example of the spectra obtained alongside the DESI-MS images corresponding to the relative intensity and location of each identified molecule in the droplet. HHQ (*m/z* 244.168) can be seen in red, and PQS is shown in blue at *m/z* 260.137. Two variations of NHQ can be seen in green and purple at *m/z* 270.1843 and 272.200, respectively.

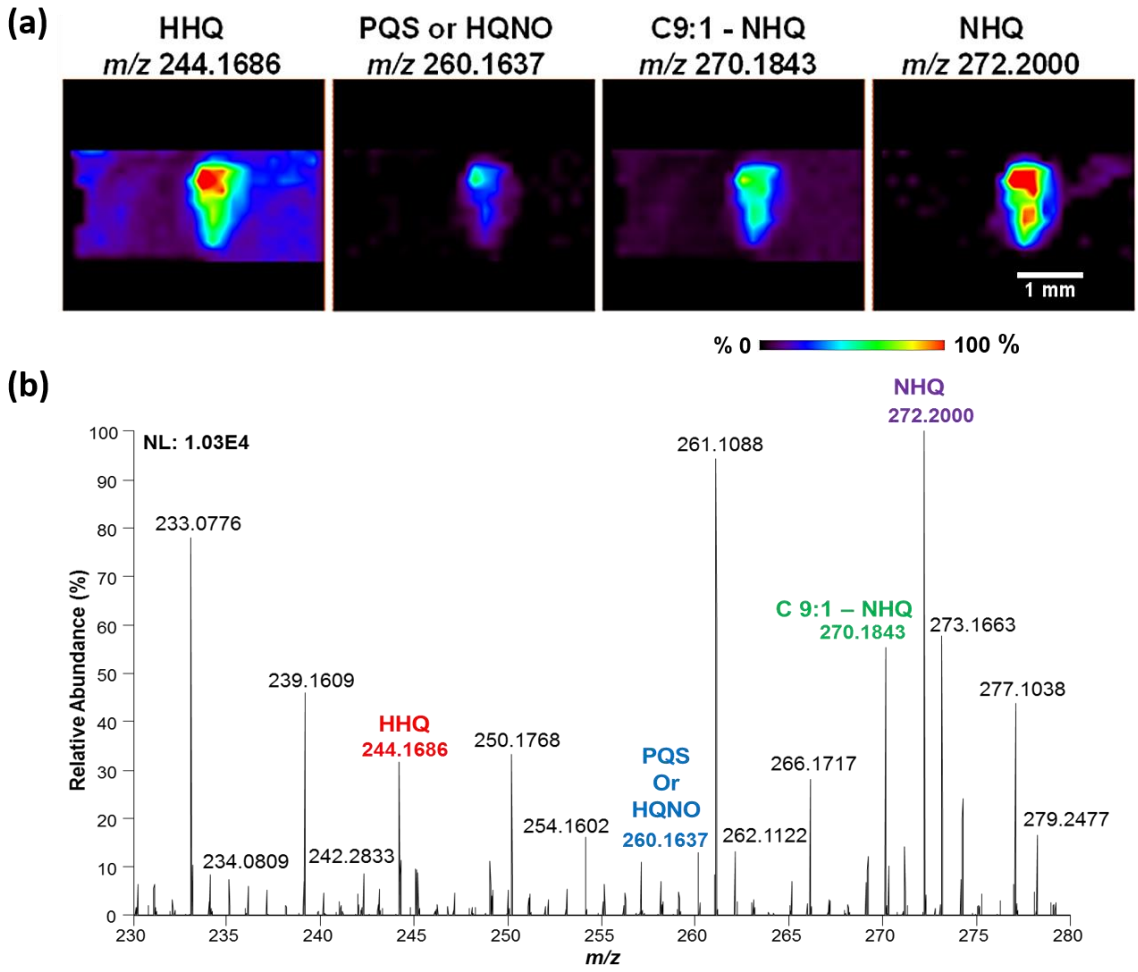

Figure 6.5: PQS analogs identified in positive ion mode in a stationary phase droplet. DESI-MS images are shown in the top row (a) with the relative intensities displayed from 0 – 100%. The mass spectrum obtained in (b) indicates the *m/z* of each identified molecule. Courtesy of Marta Sans.

Following successful identification of PQS and many of its analogs, further studies involving droplets of cells in both stationary and exponential phases were compared to determine if different molecules could be detected based on cellular growth phase. Figure 6.6 shows the spectra obtained from this experiment. In Figure 6.6 (a), the stationary phase cells are clearly producing PQS and the PQS analogs detected earlier, in the *m/z* range of ~230 to 300 indicated by the dashed outline labeled "signaling molecules." However, in

the exponential phase cells, these peaks are absent, and the choline, at *m/z* 104.1067 had the highest relative abundance. One peak that did appear in both spectra, located at *m/z* 254.1069, has yet to be identified, but its high relative abundance over this range in both samples indicates that it could be important in both stages of growth.

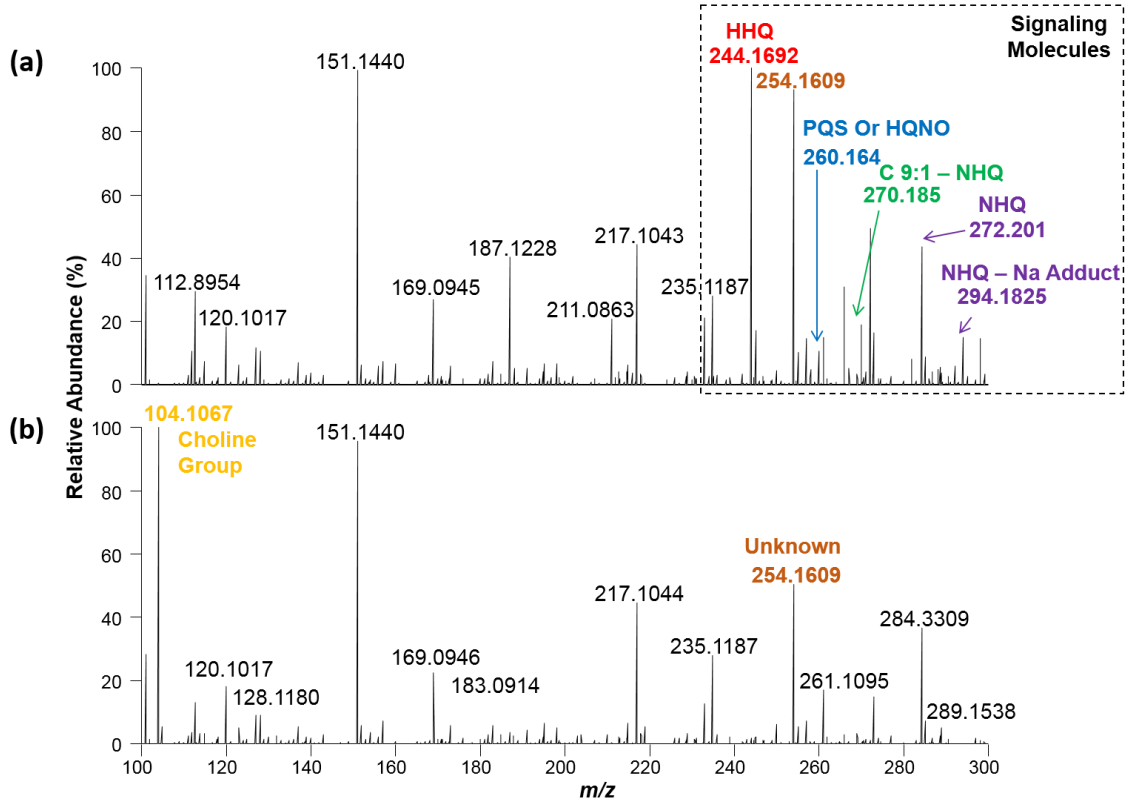

Figure 6.6: Mass spectra obtained from cell samples in stationary (a) vs. exponential (b) phase. Courtesy of Marta Sans.

A number of peaks were absent in either of the two stages, likely a result of differing genetic expression as a result of the sociomicrobiological environment. This discrepancy is illustrated in Figure 6.7, which depicts DESI-MS imaging of stationary vs. exponential phase droplets for choline (104.107 *m/z*) and PQS (260.164 *m/z*). While choline was detected at high levels in the exponential phase droplet, its stationary counterpart on the

same slide did not produce detectable levels, as shown in Figure 6.7 (a). Similarly, PQS was found at high levels in the stationary phase droplet, but not the corresponding exponential phase droplet on the same slide, Figure 6.7 (b).

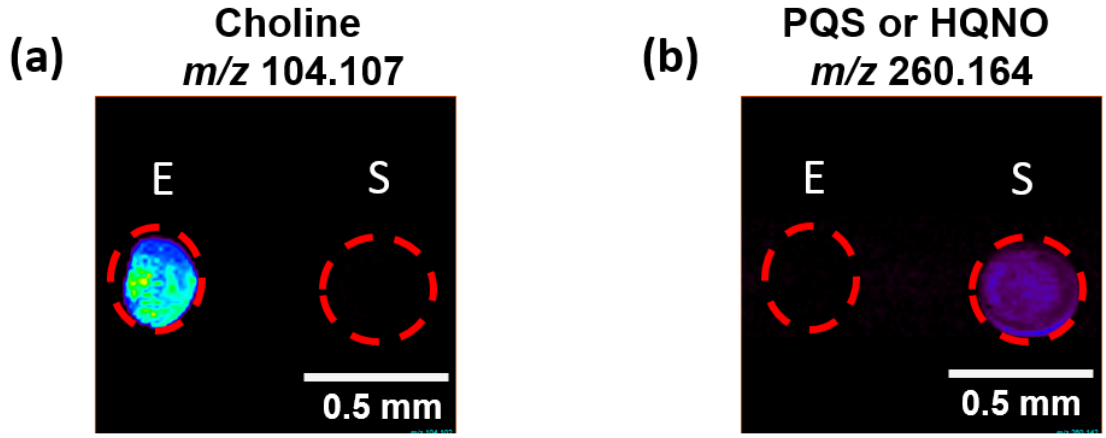

Figure 6.7: DESI-MS images of side by side exponential and stationary phase droplets for the choline (a) and PQS (b) peaks. Dashed red lines indicate droplet edges, and exponential phase droplets are on the left of each image, indicated by an "E" while stationary phase droplets are on the right, indicated by an "S." Courtesy of Marta Sans.

The next set of DESI-MSI experiments were performed on a droplet of cells in the stationary phase in negative ion mode, to compare which molecules could be identified based on a fragmentation pattern of the opposite charge. All PQS precursors and derivatives identified in positive ion mode shown in Table 6.1 were identified in their deprotonated state in the negative mode as shown in Figure 6.8. Using DESI-MS, all of the precursors and derivatives of PQS, identified in *Pseudomonas aeruginosa* previously only by a combination of capillary electrophoresis electrospray ionization (CE-ESI) MS, matrix assisted laser desorption ionization (MALDI) MS, and secondary ion (SI) MS, were observed in the stationary phase cells. These include HHQ, PQS, C 9:1 – NHQ, NHQ, C9:1 NQNO, C9-PQS, and C11:1-UHQ. While multiple techniques were necessary to identify

all these molecules in previous studies, they were all successfully identified on a single spectra with the current DESI-MS technique [131].

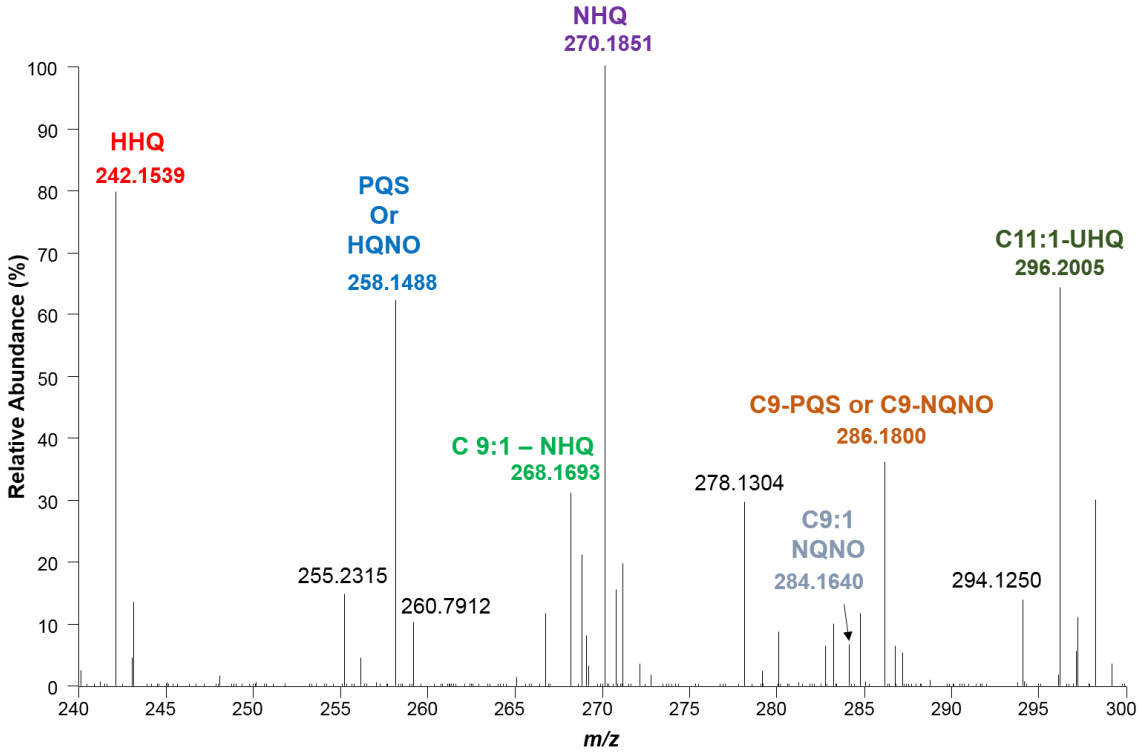

Figure 6.8: Mass spectrum of a stationary phase droplet in negative ion mode. Courtesy of Marta Sans.

While PQS and its analogs were identified in both modes for stationary cells, cellular metabolites were detected in exponential phase cells at much higher levels in negative ion mode. Table 6.2 lists a sampling of those metabolites, including a range of amino acids, sugars, and organic compounds. This likely reflects the cellular priorities, as exponential phase cells are rapidly dividing, placing emphasis on metabolic processes that encourage cellular growth.

Attribution	Molecular Formula	Detected m/z	Mass Error (ppm)	Exact Mass (daltons)
Glutamine	$C_5H_6O_3N$	128.0350	2.3	128.0353
Leucine/Isoleucine	$C_6H_{12}O_2N$	130.0870	3.1	130.0874
Aspartate	$C_4H_6O_4N$	132.0299	2.3	132.0302
Glutamate	$C_4H_6O_4N$	146.0456	2.1	146.0459
Citrate	$C_6H_7O_7$	191.0191	3.1	191.0197
Gluconate	$C_6H_{11}O_7$	195.0503	3.6	195.0510
Hexose	$C_6H_{12}ClO_6$	215.0320	3.7	215.0328
Glutamylleucine/Glutamylisoleucine	$C_{11}H_{19}O_5N_2$	259.1288	4.2	259.1299
Glutamylglutamate	$C_{10}H_{15}O_7N_2$	275.0872	3.6	275.0882
Phosphogluconate	$C_6H_{14}O_{10}P$	277.0319	4.0	277.0330
N-Acetylneuraminate	$C_{11}H_{18}O_9N$	308.0974	4.2	308.0987
Trehalose Phospahte	$C_{12}H_{24}O_{15}P$	439.0840	4.1	439.0858

Table 6.2: Sampling of metabolites detected in negative ion mode of exponential phase cells. Table adapted from data provided by Marta Sans.

Finally, using the structural array illustrated in Figure 6.3, DESI-MS was performed on cells in hydrogels fabricated in the Shear lab. Table 6.3 lists the peaks identified. Choline was present, as in rapidly dividing exponential phase cells, as were a number of unidentified compounds. Some PQS precursor molecules including HHQ and NHQ were present as well, although PQS itself was not detected.

Attribution	Molecular Formula	Detected m/z	Mass Error (ppm)	Exact Mass (daltons)
Choline Group	$C_5H_{14}ON$	104.1070	0.3	104.1070
M + N	$C_5H_{11}O_2NNa$	140.0685	-2.1	140.0682
M + K	$C_5H_{11}O_2NK$	156.0424	-1.9	156.0421
-	$C_{12}H_{11}N_2$	183.0918	-0.5	183.0917
-	$C_{10}H_{15}O_2N_2$	195.1130	-1.0	195.1128
-	$C_{11}H_{15}O_2N_4$	235.1192	-0.9	235.1190
HHQ	$C_{16}H_{22}ON$	244.1698	-0.8	244.1696
C9:1-NHQ	$C_{18}H_{24}ON$	270.1856	-1.5	270.1852
NHQ	$C_{18}H_{26}ON$	272.2012	-1.1	272.2009
-	?	371.2407	-	-

Table 6.3: Molecules detected in negative ion mode of trapped cells. Table adapted from data provided by Marta Sans.

It became clear upon comparison with results from previous experiments that the trapped cells were producing higher levels of molecules most similar to those identified in exponential phase. This is reasonable, since the cells in the traps were actively dividing, and it is likely they were all in a similar stage of growth. Figure 6.9 provides an example of this comparison. While the other molecules in Table 6.3 are present in the spectra, their relative abundance was low, rendering them unable to be observed in Figure 6.9. In this experiment, the unidentified 254.161 *m/z* peak is even more pronounced in the trapped cells (a), than in the exponential phase cell droplet (b).

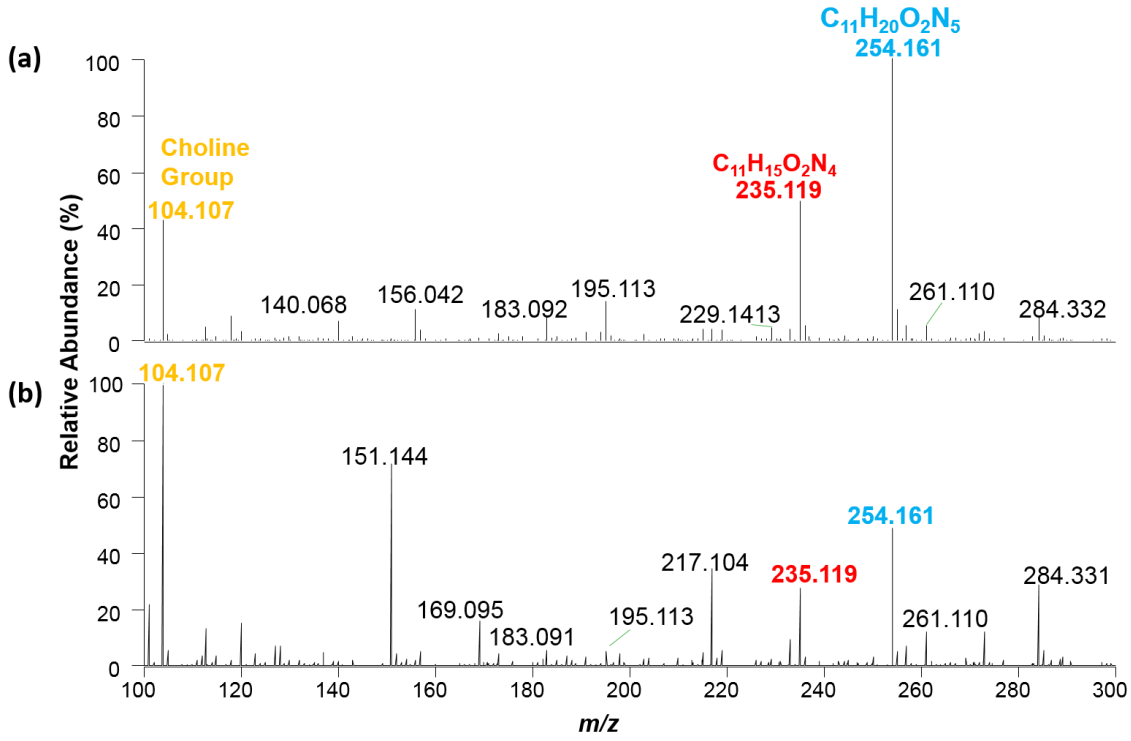

Figure 6.9: Comparison of negative ion mode analysis of cells trapped within a structure array (a) and exponential cell droplet (b). Courtesy of Marta Sans.

The spatial distribution of these molecules was also determined. In an experiment where only two of the ten traps in the array were filled with cells, the DESI-MS images reflected this discrepancy, as shown in Figure 6.10. The leftmost two traps were the only two that filled (b) and the relative intensities of the extracellular molecules detected (a) indicated they are more concentrated in this region.

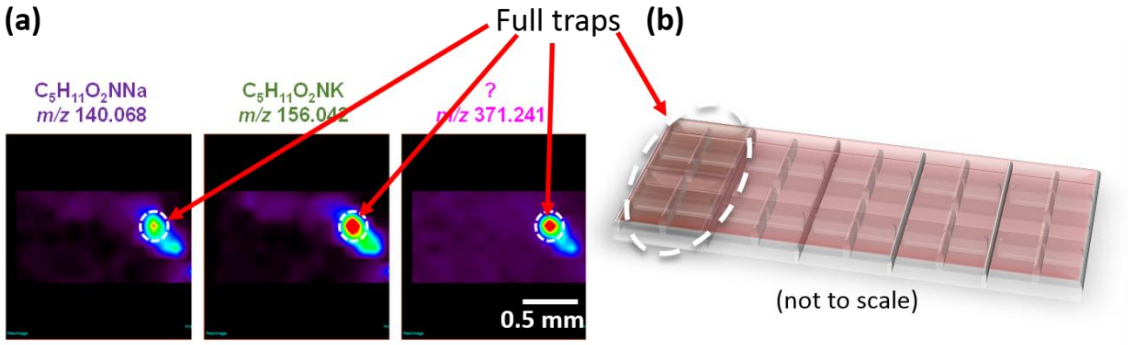

Figure 6.10: Comparison of DESI-MS imaging of traps in which only two of the array were filled, showing molecules identified in the images courtesy of Mart Sans (a) and an illustration of the traps (b). Full traps in all are indicated by a dashed white line.

However, despite the success in being able to identify these signaling molecules and metabolites from cells within the structures, post-analysis bright field images reveal the destruction caused by this technique, as shown in Figure 6.11. It is possible that the ACN and DMF solvents played a role in this structural damage, but it is likely the destruction was a result of the high pressure of the nitrogen gas jet designed to guide the electrospray towards the sample.

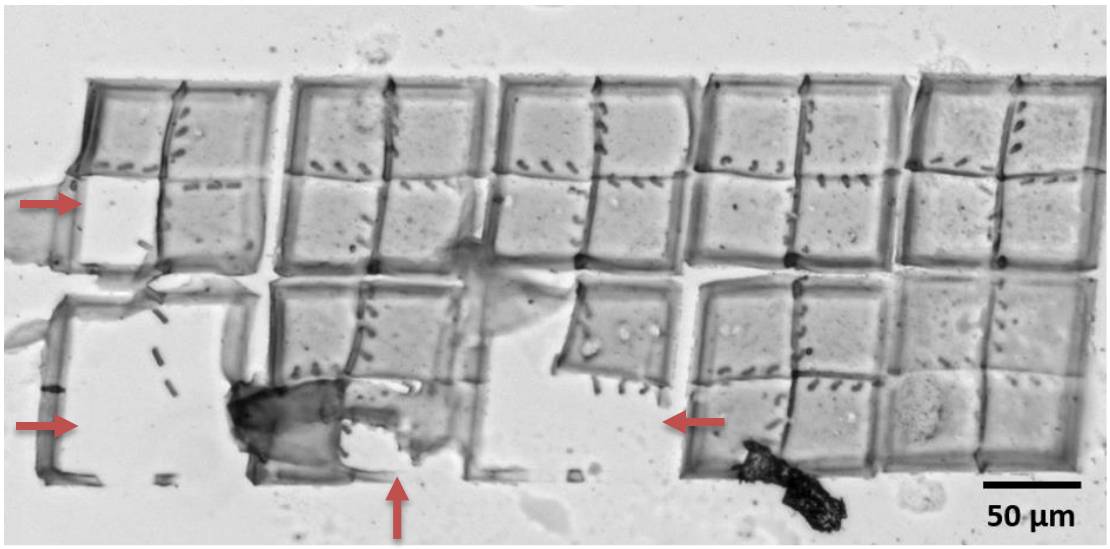

Figure 6.11: Bright field image of the traps post-analysis, showing marked destruction of the leftmost trap on the top row, and the first three on the bottom row, indicated by red arrows.

PROPOSED FUTURE STUDIES

As a result of identifying issues with the structural integrity of the hydrogels following DESI-MS, future studies are proposed involving individual stitched structures similar to the ones used in the array depicted in Figure 6.3. These structures could be fabricated all at one time, and individually sampled at various time points, and thus different stages of growth, to detect differences in cell signaling and metabolism over the course of the cells' life cycle. A slip device was conceived to protect the remaining structures and keep them hydrated and nourished with TSB while the structure in question is being analyzed. This is shown in Figure 6.12.

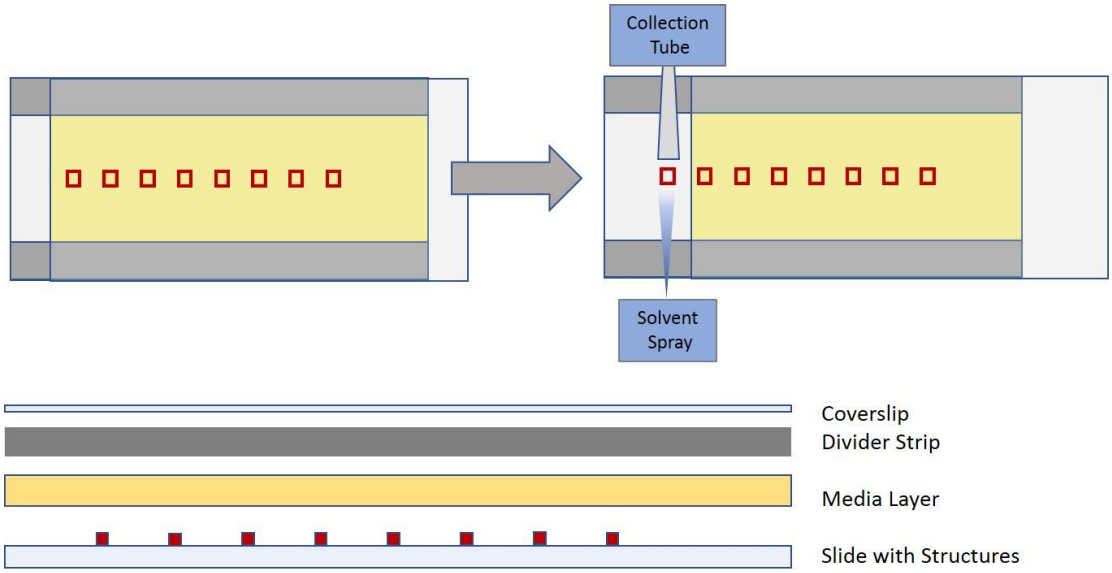

Figure 6.12: Schematic of the slip device enabling cell growth within traps while allowing analysis of one trap at a given time point. Following fabrication, all structures are bathed in media and contained between a coverslip and a slide (a). Analysis can be performed one structure at a time over the course of hours by sliding the top coverslip back to reveal an individual trap (b). The layers are depicted in (c), where the structures on the slide are at the bottom, followed by a layer of media, and two dividing strips are placed on either side of the slide before placing the coverslip on top.

CONCLUSION

This chapter covered a collaboration with Marta Sans of the Eberlin group involving the use of DESI-MS and DESI-MS imaging to observe extracellular signaling molecules and cellular metabolites of *Pseudomonas aeruginosa*, both from standard culture and those trapped and grown in µ3D printed structures. First, a droplet of cells in stationary phase was analyzed in positive ion mode and numerous PQS related compounds were identified. These included PQS itself, HHQ, NHQ and other analogs. Next, droplets of stationary and exponential phase cells were compared in positive ion mode, and while the stationary phase cells again produced high levels of signaling molecules, those in exponential phase did not, instead producing high levels of choline and an unidentified

peak around 254.1609 *m/z* that also was identified in the stationary phase cells. Next, stationary phase cells were analyzed in negative ion mode, and all PQS analogs that had previously been identified by a combination of CE-ESI MS, MALDI MS, and SIMS were identified using this technique. Negative ion mode of exponential phase cells, however, resulted in the detection of numerous peaks associated with cellular metabolites, such as amino acids and sugars. Finally, negative ion mode analysis of cells within the microstructures was performed, and the peaks of highest abundance corresponded with those of the exponential phase droplet, including choline and the unidentified 254.1609 *m/z* peak. It was noted that this technique, using the parameters outlined in the beginning of the chapter, was too harsh to enable multiple analyses of the same structure over time. However, it was proposed that creating a slip device for future studies that enables structures created at the same time to be analyzed over the course of hours, one at a time, could remedy this situation. This type of study would enable not only the ability to assess cellular communication at different stages of growth using a quantitative technique, but also give the ability to delve into the biogeography of these populations, imaging the spatial distribution of these important signaling molecules and metabolites.

Chapter 7: Contributions to MS Studies Involving Melittin Derivatives[3]

INTRODUCTION

Antimicrobial Peptides: Melittin

In recent years, a spike in the incidence of antibiotic resistant and multi-drug resistant infections has resulted in a heightened awareness of lack of alternative options available for the elimination of these types of microbial populations [1], [2], [5], [134]. Instead of focusing solely on antibiotic remedies, researchers have expanded their investigation into the realm of antimicrobial peptides. These oligopeptides target the lipopolysaccharide layer of the bacterial membrane, commonly referred to as the LPS in microbiology, as opposed to specific functional steps in cellular growth and development such as cell wall synthesis. In addition, because they target the stability of the cell membrane directly, they can quickly and efficiently cause death by membrane disruption, as opposed to simply slowing cell reproduction until the host immune system can overcome infection [112], [135]–[137].

Melittin itself has been studied intensely, as it belongs to a class of cytolytic peptides known to function as antimicrobials. Derived from bee venom, melittin has undergone a range of structural studies to elucidate the nature of its cytotoxicity and cytolytic properties [138], [139]. Ultraviolet Photodissociation (UVPD) mass spectrometry (MS), discussed in Chapter 1, offers a unique ability to study this antimicrobial peptide in complex with its LPS targets.

---

[3] C. Crittenden, L. Morrison, M. Fitzpatrick, A. Myers, E. Novelli, J. Rosenberg, L. Akin, V. Srinivasa, J. Shear and J. Brodbelt, "Towards mapping electrostatic interactions between Kdo2-lipid A and cationic antimicrobial peptides via ultraviolet photodissociation mass spectrometry," *Analyst*, vol. 143, no. 15, pp. 3607–3618, Jul. 2018.
Author performed cell culture, live/dead assays and all confocal microscopy.

Melittin and Kdo_2–Lipid A

Studying the melittin/LPS complex requires a model system which can be representative of the binding between the peptide and lipopolysaccharide present in the bacterial membrane. Research has suggested that the ability of melittin to cause cytolytic damage stems primarily from its association and binding with the Lipid A portion of LPS- a hydrophobic portion of the molecule that enables LPS anchoring to the membrane [140]. In an effort to elucidate the binding motif, Kdo_2–Lipid A (KLA), a truncated analog of LPS, was chosen by Dr. Chris Crittenden of the Brodbelt group to be the substrate for antimicrobial peptide analyses using UVPD-MS in conjunction with higher energy collisional dissociation (HCD) [78], [136]. Melittin itself was compared to three altered peptide sequences, in which the residues suspected of being responsible for assisting in binding to LPS was either moved along the sequence or eliminated. Table 7.1 displays these sequences.

Peptide Name	Sequence	Alteration from Native Sequence
Melittin	GIGAVLKVLTTGLPALISWIKRKRQQ	None
Melittin-RS	QQRIWSILAPLGTTLVKRKRLVAGIG	Reversed, KRKR motif place change, R-K substitution
Melittin-S	GIGAVLKVLTIGLKRKRWIPALISQQ	KRKR motif place change only
Melittin-NoKRKR	GRIGAVLKVLTIGLPRALISWIAAQQ	Complete omission of KRKR motif, two R additions

Table 7.1: Table displaying peptide and analog sequences and alterations from the native peptide, adapted from data provided by Dr. Chris Crittenden.

Following MS analysis, cell viability studies were performed to determine the effect of the melittin analogs on *P. aeruginosa* compared with melittin itself. These involved dosing exponential phase cells with varying concentrations of melittin and the analogs to determine kill rate using a constitutively expressed green fluorescent protein (GFP) reporter and propidium iodide, a cellular viability stain that indicates membrane

permeability and resultant cell death. Fluorescence from both fluorophores was analyzed using confocal laser scanning microscopy (CLSM).

Finally, in addition to identifying the binding sites within the complex using UVPD-MS and the cell viability studies using CLSM, circular dichroism was performed by Elisa Novelli of the Webb group to elucidate the ties between the cell viability and MS results [78].

EXPERIMENTAL DESIGN AND METHODS

Contributions by the author included determining the antimicrobial effects of the peptide melittin and three of its analogs on the model organism *Pseudomonas aeruginosa*. An experiment was designed to determine the kill rate of cells exposed to these peptides versus cells exposed only to tryptic soy broth. Controls were performed alongside all trials, in which cells were treated identically except for the administering of peptide.

Reagents

Tryptic soy broth (R455052) was acquired from Thermo Scientific (Waltham, MA). Tryptic soy agar (R455002) was obtained from Remel (San Diego, CA). Carbenicillin disodium salt (BP2648-1) was purchased from Fisher BioReagents (Fairlawn, NJ). Propidium iodide (440300250) was obtained from Acros Organics (Geel. Belgium). Melittin from honey bee venom 85% (M2272) was acquired from Sigma-Aldrich (St Louis, MO). Melittin-RS, melittin-S, and melittin NoKRKR were purchased from United Biosystems Inc. (Herndon, VA) using their Custom Peptide Synthesis Service.

Bacterial Strains, Plasmids, and Culture Conditions

All experiments were conducted using *Pseudomonas aeruginosa* strain PA01, which expresses green fluorescent protein (GFP) constitutively through transfection with

the *gfp* containing plasmid pMRP9-1. This plasmid also contains a carbenicillin resistance marker, which was maintained using a carbenicillin concentration of 10 μg mL^{-1} in both the tryptic soy agar (TSA) and tryptic soy broth (TSB). Liquid cultures used in all experiments were started from TSA plates and grown in glass culture tubes containing 4 mL TSB. The tubes were subjected to constant aeration on a shaker at a rate of 250 rpm in a 37 °C incubator overnight until stationary phase was reached. 200 μL of this culture were then diluted into TSB to reach a total volume of 4 Ml, and the tube was returned to the incubator shaker for 1.25 hours. Cell cultures at t = 1.25 hours were consistently in logarithmic phase and averaged an optical density (OD) of approximately 0.2 at 600 nm.

Growth Conditions and Antimicrobial Dosing

Experiments were performed in a Labtek 8 well chambered #1 borosilicate coverslip measuring 25 x 57 mm (134534) from Thermo Fisher (Waltham, MA). 200 μL of cell culture at t = 1.25 hours were pipetted into each of the eight wells and returned to 37 °C without shaking for three hours. Each well was then rinsed with fresh 1/3 strength TSB diluted with deionized water to remove unattached cells. This solution was then removed from all wells and the peptides: melittin (MEL), melittin-RS (MEL RS), melittin-S (MEL S), and melittin-NoKRKR (MEL NoKRKR), were each solubilized in 1/3 strength TSB and administered. Figure 7.2 illustrates this distribution. The chambered coverslip was then left at ~22 °C, for two hours. The liquid was then removed from all wells and replaced with a 30 μM solution of a propidium iodide (PI) cell viability stain in phosphate buffered saline (PBS). The wells were incubated at RT for fifteen minutes. They were then imaged using confocal microscopy. This procedure was carried out using three different concentrations of the various peptides: 50.0 μg mL^{-1}, 25.0 μg mL^{-1}, and 12.5 μg mL^{-1}. Controls contained only 1/3 strength TSB during the dosing period.

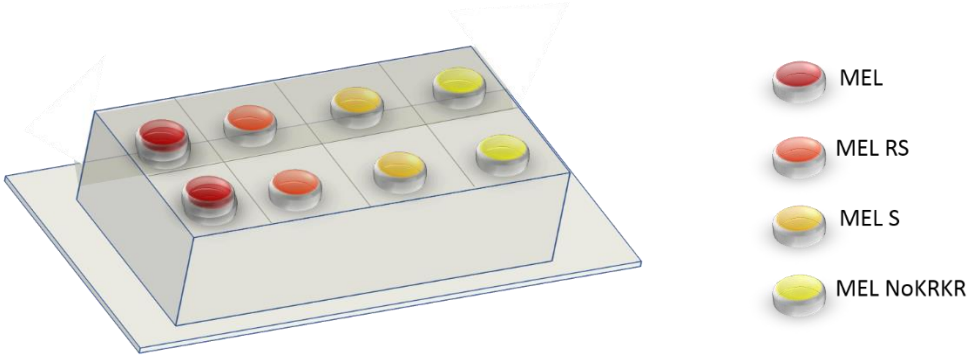

Figure 7.1: Peptide distribution in the 8 well chambered coverslip.

Imaging and Data Analysis

Imaging was performed using an LSM 710 Confocal combined with an Elyra S.1 Structured Illumination Super Resolution Microscope and a Plan-Apochromat 63x/1.4 oil/DIC M27 objective from Zeiss (Oberkochen, Germany). Collection was recorded and visualized using standard Zeiss software, Zen. A 488 nm excitation source was employed at 2 % and collection filtration for the GFP and PI channels were set at 493 – 572 nm and 622 – 719 nm, respectively. To ensure thorough sample acquisition, 40 slices at an interval of 0.25 µm were collected.

Data analysis was performed using ImageJ software from the National Institute of Health (Bethesda, MD). Cell death was calculated by reducing the images to binary and taking the ratio of the white pixels in the PI channel to the total white pixel count contained in the PI and GFP channels.

RESULTS AND DISCUSSION

The effectiveness of melittin and the three analogs as antimicrobials was gauged as a measure of cell death compared to control populations. A graph depicting the mortality rates produced by each peptide at the three concentrations compared to a control can be

seen in Figure 7.3. Representative confocal images from all concentrations used for each of the four peptides are shown in Figures 7.4 – 7.6.

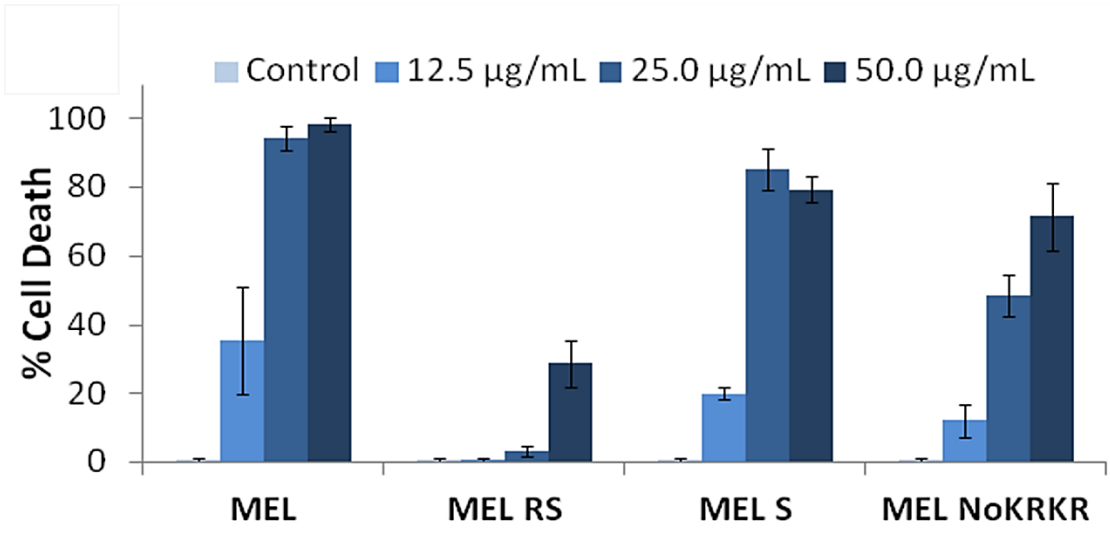

Figure 7.2: Graph displaying the mortality rates of cells treated with the four peptides at three concentrations compared to controls. Error bars represent standard deviation, n = 5. Courtesy of Chris Crittenden.

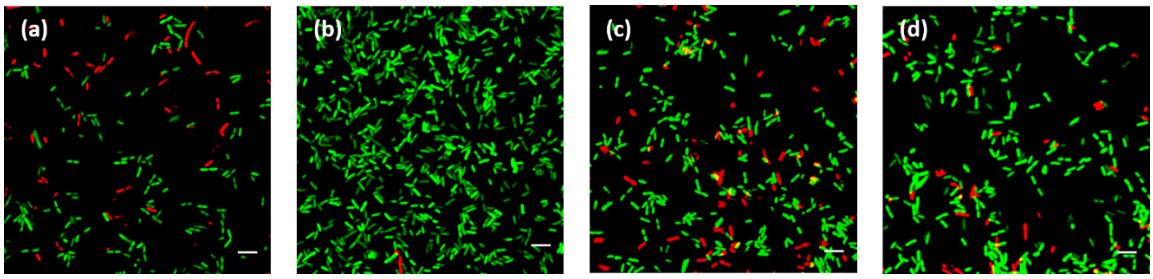

Figure 7.3: Confocal images of cells dosed with 12.5 µg mL^{-1} of each of the four peptides. GFP indicates the presence of live cells (green) and PI indicates the presence of dead cells (red). Cells were dosed with MEL (a), MEL RS (b), MEL S (c) and MEL NoKRKR (d). Scale bars are 5 µm.

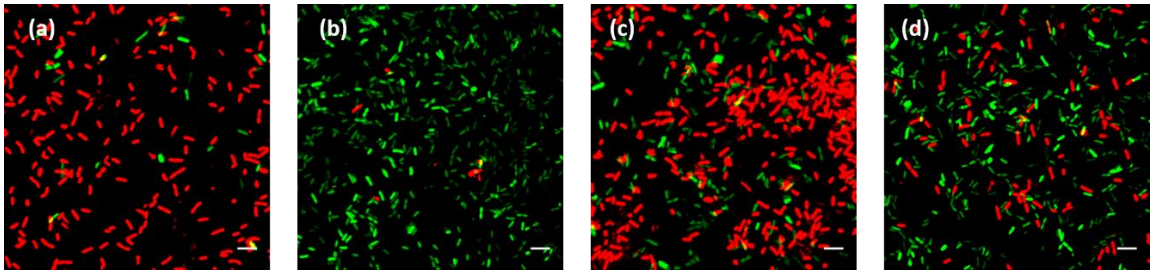

Figure 7.4: Confocal images of cells dosed with 25 μg mL^{-1} of each of the four peptides. GFP indicates the presence of live cells (green) and PI indicates the presence of dead cells (red). Cells were dosed with MEL (a), MEL RS (b), MEL S (c) and MEL NoKRKR (d). Scale bars 5 are μm.

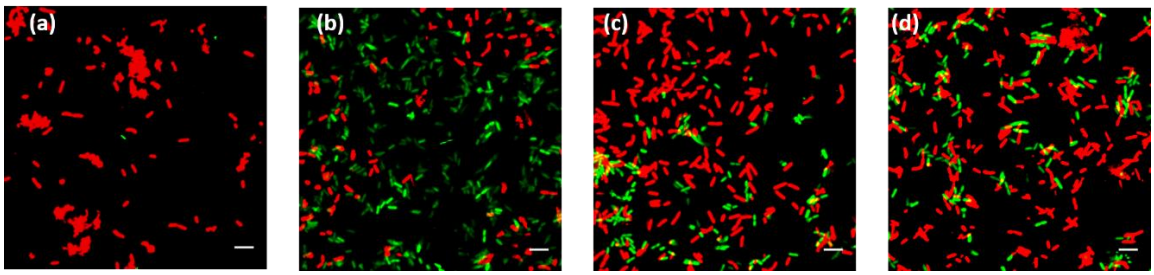

Figure 7.5: Confocal images of cells dosed with 50 μg mL^{-1} of each of the four peptides. GFP indicates the presence of live cells (green) and PI indicates the presence of dead cells (red). Cells were dosed with MEL (a), MEL RS (b), MEL S (c) and MEL NoKRKR (d). Scale bars are 5 μm.

It is clear from both Figure 7.3 and Figures 7.4 – 7.6 (a) that melittin, a known antimicrobial peptide resulted in high levels of growth inhibition at very low concentrations, and proceeded to cause high levels of cell death as the concentration increased [139]. While the 12.5 μg mL^{-1} dose resulted in a kill rate of 35 ± 2 x 10^1 % as seen in Figure 7.3, it is clear from the representative image in Figure 7.4 (a) that the overall cell growth has been inhibited. Furthermore, as aforementioned, the percentage of cell death in Figure 7.3 for 25 and 50 μg mL^{-1} are 94 ± 3 %, and 98 ± 2 %, respectively.

MEL S had the second highest efficiency in producing cell death, as evidenced in Figure 7.3 and Figures 7.4 – 7.6 (c). The 12.5 μg mL^{-1} dose resulted in a kill rate of 20 ± 2

%, while the median and maximum of 25 μg mL^{-1} and 50 μg mL^{-1} resulted in statistically similar results of 85 ± 6 % and 80 ± 4 %, respectively.

Interestingly, MEL NoKRKR was less effective than both MEL and MEL S at low concentrations but neared the death rates reached by MEL S at the maximum concentration tested. This can be observed quantitatively in Figure 7.3 and qualitatively in Figure 7.4 – 7.6 (d). At 12.5 μg mL^{-1} and 25 μg mL^{-1} the cell death rate was 12 ± 5 % and 48 ± 6 %, respectively, however at 50 μg mL^{-1} it reached 72 ± 1 x 10^1 %, statistically similar to that of MEL S at the same concentration.

It was also observed that at a concentration of 50 μg mL^{-1} trials involving MEL, MEL RS, and MEL NoKRKR resulted in increased levels of cell degradation shown in Figure 7.7. It is likely that the interactions of these peptides caused a destabilization of the cellular membrane leading to lysis, which has been previously reported with melittin [138].

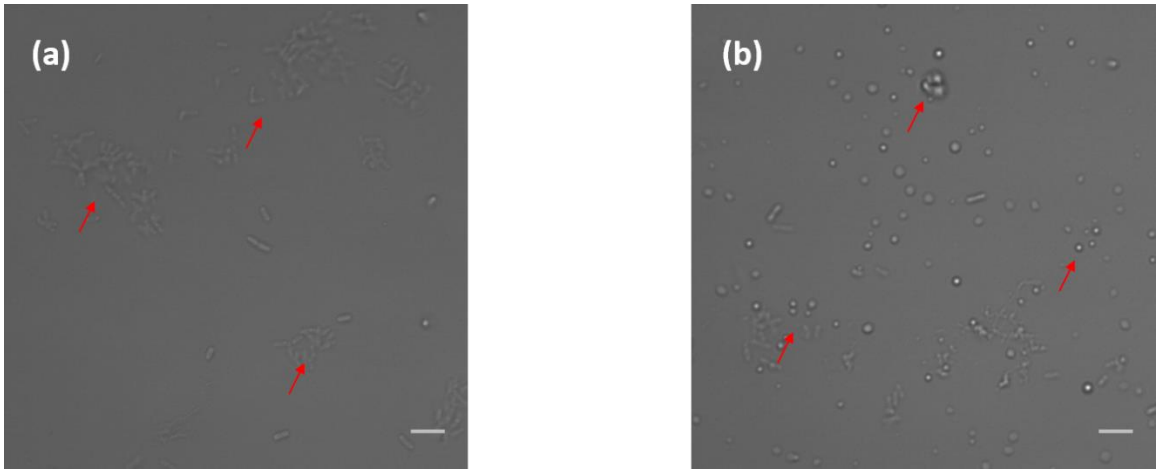

Figure 7.6: Bright field images showing the results of PA01 dosed with 50 μg mL^{-1} MEL. Images show clusters of lysed cells (a) and debris from lysed cells on the coverslip (b). Scale bars are 5 μM.

MEL RS was the least effective at causing cell death and failed to cause significant levels of cell growth inhibition even at the most concentrated level of peptide. Figures 7.4

– 7.6 (b) demonstrate this trend, and the kill rates as shown in Figure 7.3 at 12.5 μg mL^{-1}, 25 μg mL^{-1}, and 50 μg mL^{-1} are 1 ± 4 %, 3 ± 2 %, and 29 ± 7 %, respectively.

Considering only the cell viability results presented here, and the sequence alterations delineated in Table 7.1, some of these results appear counterintuitive initially. Hypothesizing that the KRKR motif and its placement in the melittin peptide sequence are the major binding factors, and thus indicate the effectiveness of the peptide as an antimicrobial, some issues come to light. The first is that the efficacy of MEL RS is much lower than any of the other peptides. While the reversal of the peptide should affect binding affinity to KLA, the continued proximity to the C-terminus could have still resulted in effective binding. However, the kill rates suggest otherwise. Similarly, shifting this motif closer to the middle of the peptide as in MEL S could drastically reduce the binding efficiency upon folding, but again this is not suggested by the mortality rates. Finally, removing the KRKR motif completely, as is the case in MEL NoKRKR should cause the interaction between peptide and lipid to decrease drastically. Remarkably, while this does result in a much lower cell death rate at low and medium concentrations of peptide, at high concentrations, it is observed to be close to MEL-S in efficiency.

The data obtained using mass spectrometry and circular dichroism by Crittenden et al. must also be taken into account to address these issues [78]. The researchers found that MEL and MEL S have the most similar secondary structures when bound to KLA, namely an increase in β-sheets, while MEL RS differs significantly; binding of MEL RS causes an increase in helical formations. This discrepancy could greatly affect the binding affinity of the peptide for the lipid A substrate. In addition, it was found that MEL NoKRKR binding results in an even greater number of helical formations. While these observations could explain the cell death results obtained with respect to MEL, MEL S, and MEL RS, those obtained for MEL NoKRKR still prove puzzling. It has been hypothesized that at very high

concentrations, an equilibrium shift may occur, allowing the peptide to bind and undergo a restructuring, resulting in increased β-sheet structures and eventually cell death [78]

CONCLUSION

This chapter covered the analysis of melittin and 3 analogs, using live dead assays and confocal microcopy to supplement mass spectrometry studies performed by Dr. Chris Crittenden of the Brodbelt group. Comparing a range of antimicrobial peptide concentrations near those found in biological systems, the efficacy in killing *Pseudomonas aeruginosa* was compared using propidium iodide staining and confocal imaging of cells that constitutively produced GFP. It was determined melittin , as expected, produced high levels of cell death at the two higher concentrations, 25 and 50 μg mL^{-1}, and significantly hindered growth at the lowest concentration, 12.5 μg mL^{-1}. Its kill rate efficiency was trailed by MEL S, and then MEL NoKRKR, which performed poorly at low rates, nearly matched the kill rate of MEL S at the maximum concentration. MEL RS was the least effective, and failed to produce high rates of cell death even at the maximum concentration. It was also observed that at high concentrations, melittin caused extreme cases of cell lysis, visible in bright field images depicting cellular debris strew across the coverslip.

The results of the cell viability alone, and the cell viability and mass spectrometry were difficult to interpret, but by combining mass spectrometry, cell viability and circular dichroism together, a clearer picture emerged. Though the KRKR motif and it's placement within the melittin sequence has been hypothesized to be the major binding factors, MEL RS was found to have a significantly different secondary structure when bound to KLA, explaining the poor cell kill rates. While this does not explain the success of MEL NoKRKR at the maximum concentration, it could be that at very high concentrations an equilibrium shift occurs causing a restructuring of the peptide allowing it to bind

effectively. This would explain the pattern witnessed in the cell viability experiments. Together, this highlights the necessity for integrating multiple analytical techniques in the search for answers to difficult questions about the sociomicrobiology of cells.

Works Cited

[1] S. Angeletti *et al.*, "Multi-drug resistant Pseudomonas aeruginosa nosocomial strains: Molecular epidemiology and evolution," *Microb. Pathog.*, vol. 123, pp. 233–241, Oct. 2018.

[2] G. Sotgiu and G. B. Migliori, "Facing multi-drug resistant tuberculosis," *Pulm. Pharmacol. Ther.*, vol. 32, pp. 144–148, Jun. 2015.

[3] S. Lax and J. A. Gilbert, "Hospital-associated microbiota and implications for nosocomial infections," *Trends Mol. Med.*, vol. 21, no. 7, pp. 427–432, Jul. 2015.

[4] T. Bjarnsholt *et al.*, "The in vivo biofilm," *Trends Microbiol.*, vol. 21, no. 9, pp. 466–474, Sep. 2013.

[5] K. Lewis, "Riddle of biofilm resistance," *Antimicrob. Agents Chemother.*, vol. 45, no. 4, pp. 999–1007, Apr. 2001.

[6] L. R. Mulcahy, V. M. Isabella, and K. Lewis, "Pseudomonas aeruginosa Biofilms in Disease," *Microb. Ecol.*, vol. 68, no. 1, pp. 1–12, Jul. 2014.

[7] "Role of Multicellular Aggregates in Biofilm Formation | mBio." [Online]. Available: https://mbio.asm.org/content/7/2/e00237-16. [Accessed: 04-Nov-2018].

[8] C. B. Ibberson *et al.*, "Co-infecting microorganisms dramatically alter pathogen gene essentiality during polymicrobial infection," *Nat. Microbiol.*, vol. 2, p. 17079, May 2017.

[9] J. L. Murray, J. L. Connell, A. Stacy, K. H. Turner, and M. Whiteley, "Mechanisms of synergy in polymicrobial infections," *J. Microbiol. Seoul Korea*, vol. 52, no. 3, pp. 188–199, Mar. 2014.

[10] A. Stacy, L. McNally, S. E. Darch, S. P. Brown, and M. Whiteley, "The biogeography of polymicrobial infection," *Nat. Rev. Microbiol.*, vol. 14, no. 2, pp. 93–105, Feb. 2016.

[11] A. R. Stacy, S. P. Diggle, and M. Whiteley, "Rules of engagement: defining bacterial communication," *Curr. Opin. Microbiol.*, vol. 15, no. 2, pp. 155–161, Apr. 2012.

[12] S. P. Diggle, A. S. Griffin, G. S. Campbell, and S. A. West, "Cooperation and conflict in quorum-sensing bacterial populations," *Nature*, vol. 450, no. 7168, pp. 411–414, Nov. 2007.

[13] K. L. Michie, D. M. Cornforth, and M. Whiteley, "Bacterial tweets and podcasts #signaling#eavesdropping#microbialfightclub," *Mol. Biochem. Parasitol.*, vol. 208, no. 1, pp. 41–48, Jul. 2016.

[14] J. W. Larkin *et al.*, "Signal Percolation within a Bacterial Community," *Cell Syst.*, vol. 7, no. 2, pp. 137-145.e3, Aug. 2018.

[15] A. K. Wessel, L. Hmelo, M. R. Parsek, and M. Whiteley, "Going local: technologies for exploring bacterial microenvironments," *Nat. Rev. Microbiol.*, vol. 11, no. 5, pp. 337–348, May 2013.

[16] R. Nielson, B. Kaehr, and J. B. Shear, "Microreplication and Design of Biological Architectures Using Dynamic-Mask Multiphoton Lithography," *Small*, vol. 5, no. 1, pp. 120–125, Jan. 2009.

[17] E. C. Spivey, E. T. Ritschdorff, J. L. Connell, C. A. McLennon, C. E. Schmidt, and J. B. Shear, "Multiphoton Lithography of Unconstrained Three-Dimensional Protein Microstructures," *Adv. Funct. Mater.*, vol. 23, no. 3, pp. 333–339, Jan. 2013.
[18] B. Kaehr and J. B. Shear, "Mask-Directed Multiphoton Lithography," *J. Am. Chem. Soc.*, vol. 129, no. 7, pp. 1904–1905, Feb. 2007.
[19] J. L. Connell, A. K. Wessel, M. R. Parsek, A. D. Ellington, M. Whiteley, and J. B. Shear, "Probing Prokaryotic Social Behaviors with Bacterial 'Lobster Traps,'" *mBio*, vol. 1, no. 4, Oct. 2010.
[20] J. L. Connell, E. T. Ritschdorff, M. Whiteley, and J. B. Shear, "3D printing of microscopic bacterial communities," *Proc. Natl. Acad. Sci. U. S. A.*, vol. 110, no. 46, pp. 18380–18385, 2013.
[21] J. L. Connell, E. T. Ritschdorff, and J. B. Shear, "Three-Dimensional Printing of Photoresponsive Biomaterials for Control of Bacterial Microenvironments," *Anal. Chem.*, vol. 88, no. 24, pp. 12264–12271, Dec. 2016.
[22] J. L. Connell, J. Kim, J. B. Shear, A. J. Bard, and M. Whiteley, "Real-time monitoring of quorum sensing in 3D-printed bacterial aggregates using scanning electrochemical microscopy," *Proc. Natl. Acad. Sci. U. S. A.*, vol. 111, no. 51, pp. 18255–18260, 2014.
[23] M. B. Miller and B. L. Bassler, "Quorum sensing in bacteria," *Annu. Rev. Microbiol.*, vol. 55, pp. 165–199, 2001.
[24] W. C. Fuqua, S. C. Winans, and E. P. Greenberg, "Quorum sensing in bacteria: the LuxR-LuxI family of cell density-responsive transcriptional regulators.," *J. Bacteriol.*, vol. 176, no. 2, pp. 269–275, Jan. 1994.
[25] M. Whiteley, S. P. Diggle, and E. P. Greenberg, "Progress in and promise of bacterial quorum sensing research," *Nature*, vol. 551, no. 7680, pp. 313–320, 15 2017.
[26] J. M. Yarwood, D. J. Bartels, E. M. Volper, and E. P. Greenberg, "Quorum Sensing in Staphylococcus aureus Biofilms," *J. Bacteriol.*, vol. 186, no. 6, pp. 1838–1850, Mar. 2004.
[27] M. R. Parsek and E. P. Greenberg, "Sociomicrobiology: the connections between quorum sensing and biofilms," *Trends Microbiol.*, vol. 13, no. 1, pp. 27–33, Jan. 2005.
[28] H. L. Barr *et al.*, "Pseudomonas aeruginosa quorum sensing molecules correlate with clinical status in cystic fibrosis," *Eur. Respir. J.*, vol. 46, no. 4, pp. 1046–1054, Oct. 2015.
[29] S. T. Rutherford and B. L. Bassler, "Bacterial Quorum Sensing: Its Role in Virulence and Possibilities for Its Control," *Cold Spring Harb. Perspect. Med.*, vol. 2, no. 11, Nov. 2012.
[30] M. Gao *et al.*, "A crucial role for spatial distribution in bacterial quorum sensing," *Sci. Rep.*, vol. 6, no. 1, Dec. 2016.
[31] H. J. Kim, J. Q. Boedicker, J. W. Choi, and R. F. Ismagilov, "Defined Spatial Structure Stabilizes a Synthetic Multispecies Bacterial Community," *Proc. Natl. Acad. Sci. U. S. A.*, vol. 105, no. 47, pp. 18188–18193, 2008.

[32] S. E. Darch *et al.*, "Spatial determinants of quorum signaling in a *Pseudomonas aeruginosa* infection model," *Proc. Natl. Acad. Sci.*, p. 201719317, Apr. 2018.
[33] B. J. Staudinger *et al.*, "Conditions Associated with the Cystic Fibrosis Defect Promote Chronic Pseudomonas aeruginosa Infection," *Am. J. Respir. Crit. Care Med.*, vol. 189, no. 7, pp. 812–824, Apr. 2014.
[34] W. K. Kwong and N. A. Moran, "Cultivation and characterization of the gut symbionts of honey bees and bumble bees: description of Snodgrassella alvi gen. nov., sp. nov., a member of the family Neisseriaceae of the Betaproteobacteria, and Gilliamella apicola gen. nov., sp. nov., a member of Orbaceae fam. nov., Orbales ord. nov., a sister taxon to the order 'Enterobacteriales' of the Gammaproteobacteria," *Int. J. Syst. Evol. Microbiol.*, vol. 63, no. Pt 6, pp. 2008–2018, Jun. 2013.
[35] J. Lee and L. Zhang, "The hierarchy quorum sensing network in Pseudomonas aeruginosa," *Protein Cell*, vol. 6, no. 1, pp. 26–41, Jan. 2015.
[36] K. Kim *et al.*, "HHQ and PQS, two Pseudomonas aeruginosa quorum-sensing molecules, down-regulate the innate immune responses through the nuclear factor-κB pathway," *Immunology*, vol. 129, no. 4, pp. 578–588, Apr. 2010.
[37] M. Asif and M. Acharya, "Quorum sensing: A nobel target for antibacterial agents," *Avicenna J. Med.*, vol. 2, no. 4, pp. 97–99, 2012.
[38] T. H. Jakobsen, T. Bjarnsholt, P. Ø. Jensen, M. Givskov, and N. Høiby, "Targeting quorum sensing in Pseudomonas aeruginosa biofilms: current and emerging inhibitors," *Future Microbiol.*, vol. 8, no. 7, pp. 901–921, Jul. 2013.
[39] H. Wu, C. Moser, H.-Z. Wang, N. Høiby, and Z.-J. Song, "Strategies for combating bacterial biofilm infections," *Int. J. Oral Sci.*, vol. 7, no. 1, pp. 1–7, Mar. 2015.
[40] L. A. Novotny, J. A. Jurcisek, S. D. Goodman, and L. O. Bakaletz, "Monoclonal antibodies against DNA-binding tips of DNABII proteins disrupt biofilms in vitro and induce bacterial clearance in vivo," *EBioMedicine*, vol. 10, pp. 33–44, Aug. 2016.
[41] E. J. Stewart, "Growing Unculturable Bacteria," *J. Bacteriol.*, vol. 194, no. 16, pp. 4151–4160, Aug. 2012.
[42] M. Cassler *et al.*, "Use of Real-Time qPCR to Quantify Members of the Unculturable Heterotrophic Bacterial Community in a Deep Sea Marine Sponge, Vetulina sp," *Microb. Ecol.*, vol. 55, no. 3, pp. 384–394, Apr. 2008.
[43] V. de Jager and R. J. Siezen, "Single-cell genomics: unravelling the genomes of unculturable microorganisms: Genomics update," *Microb. Biotechnol.*, vol. 4, no. 4, pp. 431–437, Jul. 2011.
[44] P. D. Schloss and J. Handelsman, "Metagenomics for studying unculturable microorganisms: cutting the Gordian knot," *Genome Biol.*, p. 4, 2005.
[45] S. R. Vartoukian, R. M. Palmer, and W. G. Wade, "Strategies for culture of 'unculturable' bacteria," *FEMS Microbiol. Lett.*, vol. 309, no. 1, pp. 1–7, Aug. 2010.
[46] K. L. Visick, K. M. Hodge-Hanson, A. H. Tischler, A. K. Bennett, and V. Mastrodomenico, "Tools for rapid genetic engineering of Vibrio fischeri," *Appl Env. Microbiol*, p. AEM.00850-18, May 2018.

[47] J. D. Spikes, H. R. Shen, P. Kopecková, and J. Kopecek, “Photodynamic crosslinking of proteins. III. Kinetics of the FMN- and rose bengal-sensitized photooxidation and intermolecular crosslinking of model tyrosine-containing N-(2-hydroxypropyl)methacrylamide copolymers,” *Photochem. Photobiol.*, vol. 70, no. 2, pp. 130–137, Aug. 1999.
[48] J. D. Spikes, H. R. Shen, P. Kopecková, and J. Kopecek, “Photodynamic crosslinking of proteins. III. Kinetics of the FMN- and rose bengal-sensitized photooxidation and intermolecular crosslinking of model tyrosine-containing N-(2-hydroxypropyl)methacrylamide copolymers,” *Photochem. Photobiol.*, vol. 70, no. 2, pp. 130–137, Aug. 1999.
[49] H. R. Shen, J. D. Spikes, P. Kopeceková, and J. Kopecek, “Photodynamic crosslinking of proteins. I. Model studies using histidine- and lysine-containing N-(2-hydroxypropyl)methacrylamide copolymers,” *J. Photochem. Photobiol. B*, vol. 34, no. 2–3, pp. 203–210, Jul. 1996.
[50] C. N. LaFratta, J. T. Fourkas, T. Baldacchini, and R. A. Farrer, “Multiphoton Fabrication,” *Angew. Chem. Int. Ed.*, vol. 46, no. 33, pp. 6238–6258, Aug. 2007.
[51] A. Grzybowski and K. Pietrzak, “Maria Goeppert-Mayer (1906–1972): Two-photon effect on dermatology,” *Clin. Dermatol.*, vol. 31, no. 2, pp. 221–225, Mar. 2013.
[52] J. B. Shear, “Peer Reviewed: Multiphoton-Excited Fluorescence in Bioanalytical Chemistry.,” *Anal. Chem.*, vol. 71, no. 17, pp. 598A-605A, Sep. 1999.
[53] E. T. Ritschdorff, R. Nielson, and J. B. Shear, “Multi-focal multiphoton lithography,” *Lab. Chip*, vol. 12, no. 5, pp. 867–871, Feb. 2012.
[54] “Antonie van Leeuwenhoek | Biography, Discoveries, & Facts,” *Encyclopedia Britannica*. [Online]. Available: https://www.britannica.com/biography/Antonie-van-Leeuwenhoek. [Accessed: 12-Nov-2018].
[55] P. A. Levin, “6 Light microscopy techniques for bacterial cell biology,” in *Methods in Microbiology*, vol. 31, Academic Press, 2002, pp. 115–132.
[56] J. Walker-Daniels, “Live Cell Imaging Methods Review,” *Mater. Methods*, Oct. 2018.
[57] A. Ettinger and T. Wittmann, “Fluorescence live cell imaging,” *Methods Cell Biol.*, vol. 123, pp. 77–94, 2014.
[58] E. P. Diamandis, “Fluorescence Spectroscopy,” *Anal. Chem.*, vol. 65, no. 12, pp. 454–459, Jun. 1993.
[59] “Introduction to Fluorescence Microscopy,” *Nikon’s MicroscopyU*. [Online]. Available: https://www.microscopyu.com/techniques/fluorescence/introduction-to-fluorescence-microscopy. [Accessed: 12-Nov-2018].
[60] E. A. Specht, E. Braselmann, and A. E. Palmer, “A Critical and Comparative Review of Fluorescent Tools for Live-Cell Imaging,” *Annu. Rev. Physiol.*, vol. 79, no. 1, pp. 93–117, Feb. 2017.
[61] *Cell Biological Applications of Confocal Microscopy*. Academic Press, 1993.
[62] “Confocal Microscopy,” *Nikon’s MicroscopyU*. [Online]. Available: https://www.microscopyu.com/techniques/confocal. [Accessed: 12-Nov-2018].

[63] "Live-cell microscopy – tips and tools | Journal of Cell Science." [Online]. Available: http://jcs.biologists.org/content/122/6/753. [Accessed: 12-Nov-2018].
[64] A. Stacy, J. Everett, P. Jorth, U. Trivedi, K. P. Rumbaugh, and M. Whiteley, "Bacterial fight-and-flight responses enhance virulence in a polymicrobial infection," *Proc. Natl. Acad. Sci. U. S. A.*, vol. 111, no. 21, pp. 7819–7824, May 2014.
[65] S. Hall *et al.*, "Cellular Effects of Pyocyanin, a Secreted Virulence Factor of Pseudomonas aeruginosa," *Toxins*, vol. 8, no. 8, Aug. 2016.
[66] A. Moayedi, J. Nowroozi, and A. Akhavan Sepahy, "Cytotoxic effect of pyocyanin on human pancreatic cancer cell line (Panc-1)," *Iran. J. Basic Med. Sci.*, vol. 21, no. 8, pp. 794–799, Aug. 2018.
[67] G. W. Lau, D. J. Hassett, H. Ran, and F. Kong, "The role of pyocyanin in Pseudomonas aeruginosa infection," *Trends Mol. Med.*, vol. 10, no. 12, pp. 599–606, Dec. 2004.
[68] J. Elliott, O. Simoska, S. Karasik, J. B. Shear, and K. J. Stevenson, "Transparent Carbon Ultramicroelectrode Arrays for the Electrochemical Detection of a Bacterial Warfare Toxin, Pyocyanin," *Anal. Chem.*, vol. 89, no. 12, pp. 6285–6289, Jun. 2017.
[69] J. Elliott, J. Duay, O. Simoska, J. B. Shear, and K. J. Stevenson, "Gold Nanoparticle Modified Transparent Carbon Ultramicroelectrode Arrays for the Selective and Sensitive Electroanalytical Detection of Nitric Oxide," *Anal. Chem.*, vol. 89, no. 2, pp. 1267–1274, Jan. 2017.
[70] M. L. Vestal, "The Future of Biological Mass Spectrometry," *J. Am. Soc. Mass Spectrom.*, vol. 22, no. 6, pp. 953–959, Jun. 2011.
[71] M. Baker, "Mass spectrometry for biologists," *Nat. Methods*, vol. 7, pp. 157–161, Feb. 2010.
[72] J. D. Watrous and P. C. Dorrestein, "Imaging mass spectrometry in microbiology," *Nat. Rev. Microbiol.*, vol. 9, no. 9, pp. 683–694, Sep. 2011.
[73] J. Abian, *JOURNAL OF MASS SPECTROMETRY J. Mass Spectrom. 34, 157È168 (1999) SPECIAL FEATURE: HISTORICAL The Coupling of Gas and Liquid Chromatography with Mass Spectrometry¤*. .
[74] W. M. A. Niessen, "MS–MS and MSn," in *Encyclopedia of Spectroscopy and Spectrometry (Second Edition)*, J. C. Lindon, Ed. Oxford: Academic Press, 1999, pp. 1675–1681.
[75] S. Editors, "A New Mass Spectrometry Method for Protein Analysis." [Online]. Available: http://www.spectroscopyonline.com/new-mass-spectrometry-method-protein-analysis. [Accessed: 08-Nov-2018].
[76] A. H. Smits and M. Vermeulen, "Characterizing Protein-Protein Interactions Using Mass Spectrometry: Challenges and Opportunities," *Trends Biotechnol.*, vol. 34, no. 10, pp. 825–834, 2016.
[77] M. B. Cammarata and J. S. Brodbelt, "Structural characterization of holo- and apo-myoglobin in the gas phase by ultraviolet photodissociation mass spectrometry," *Chem. Sci.*, vol. 6, no. 2, pp. 1324–1333, Jan. 2015.

[78] C. M. Crittenden *et al.*, "Towards mapping electrostatic interactions between Kdo2-lipid A and cationic antimicrobial peptides via ultraviolet photodissociation mass spectrometry," *Analyst*, vol. 143, no. 15, pp. 3607–3618, Jul. 2018.
[79] A. J. R. Heck, "Native mass spectrometry: a bridge between interactomics and structural biology," *Nat. Methods*, vol. 5, no. 11, pp. 927–933, Nov. 2008.
[80] G. M. Pumphrey, B. T. Hanson, S. Chandra, and E. L. Madsen, "Dynamic secondary ion mass spectrometry (SIMS) imaging of microbial populations utilizing 13C-labeled substrates in pure culture and in soil," *Environ. Microbiol.*, vol. 11, no. 1, pp. 220–229, Jan. 2009.
[81] J. Latimer *et al.*, "A novel method for exploring elemental composition of microbial communities: laser ablation-inductively coupled plasma-mass spectrometry of intact bacterial colonies," *J. Microbiol. Methods*, vol. 79, no. 3, pp. 329–335, Dec. 2009.
[82] J. B. Shaw *et al.*, "Complete protein characterization using top-down mass spectrometry and ultraviolet photodissociation," *J. Am. Chem. Soc.*, vol. 135, no. 34, pp. 12646–12651, Aug. 2013.
[83] J. P. O'Brien, W. Li, Y. Zhang, and J. S. Brodbelt, "Characterization of native protein complexes using ultraviolet photodissociation mass spectrometry," *J. Am. Chem. Soc.*, vol. 136, no. 37, pp. 12920–12928, Sep. 2014.
[84] L. J. Morrison and J. S. Brodbelt, "Charge site assignment in native proteins by ultraviolet photodissociation (UVPD) mass spectrometry," *The Analyst*, vol. 141, no. 1, pp. 166–176, Jan. 2016.
[85] J. S. Brodbelt, "Photodissociation mass spectrometry: new tools for characterization of biological molecules," *Chem. Soc. Rev.*, vol. 43, no. 8, pp. 2757–2783, Mar. 2014.
[86] R. M. Alberici *et al.*, "Ambient mass spectrometry: bringing MS into the 'real world,'" *Anal. Bioanal. Chem.*, vol. 398, no. 1, pp. 265–294, Sep. 2010.
[87] D. R. Ifa, C. Wu, Z. Ouyang, and R. G. Cooks, "Desorption electrospray ionization and other ambient ionization methods: current progress and preview," *The Analyst*, vol. 135, no. 4, pp. 669–681, Apr. 2010.
[88] Z. Takáts, J. M. Wiseman, B. Gologan, and R. G. Cooks, "Mass spectrometry sampling under ambient conditions with desorption electrospray ionization," *Science*, vol. 306, no. 5695, pp. 471–473, Oct. 2004.
[89] L. S. Eberlin, C. R. Ferreira, A. L. Dill, D. R. Ifa, and R. G. Cooks, "Desorption electrospray ionization mass spectrometry for lipid characterization and biological tissue imaging," *Biochim. Biophys. Acta BBA - Mol. Cell Biol. Lipids*, vol. 1811, no. 11, pp. 946–960, Nov. 2011.
[90] J. Watrous, N. Hendricks, M. Meehan, and P. C. Dorrestein, "Capturing Bacterial Metabolic Exchange Using Thin Film Desorption Electrospray Ionization-Imaging Mass Spectrometry," *Anal. Chem.*, vol. 82, no. 5, pp. 1598–1600, Mar. 2010.
[91] M. Manikandan *et al.*, "Biological Desorption Electrospray Ionization Mass Spectrometry (DESI MS) – unequivocal role of crucial ionization factors, solvent system and substrates," *TrAC Trends Anal. Chem.*, vol. 78, pp. 109–119, Apr. 2016.

[92] P. D. Edirisinghe *et al.*, "Detection of In Situ Derivatized Peptides in Microbial Biofilms by Laser Desorption 7.87 eV Postionizaton Mass Spectrometry," *Anal. Chem.*, vol. 79, no. 2, pp. 508–514, Jan. 2007.
[93] S. G. Boxer, M. L. Kraft, and P. K. Weber, "Advances in imaging secondary ion mass spectrometry for biological samples," *Annu. Rev. Biophys.*, vol. 38, pp. 53–74, 2009.
[94] C. LaFratta and T. Baldacchini, "Two-Photon Polymerization Metrology: Characterization Methods of Mechanisms and Microstructures," *Micromachines*, vol. 8, no. 4, p. 101, Mar. 2017.
[95] H. N. Chia and B. M. Wu, "Recent advances in 3D printing of biomaterials," *J. Biol. Eng.*, vol. 9, no. 1, Dec. 2015.
[96] M. Guvendiren, J. Molde, R. M. D. Soares, and J. Kohn, "Designing Biomaterials for 3D Printing," *ACS Biomater. Sci. Eng.*, vol. 2, no. 10, pp. 1679–1693, Oct. 2016.
[97] L. Li and J. T. Fourkas, "Multiphoton polymerization," *Mater. Today*, vol. 10, no. 6, pp. 30–37, Jun. 2007.
[98] "Overview of Crosslinking and Protein Modification - US." [Online]. Available: https://www.thermofisher.com/us/en/home/life-science/protein-biology/protein-biology-learning-center/protein-biology-resource-library/pierce-protein-methods/overview-crosslinking-protein-modification.html. [Accessed: 12-Nov-2018].
[99] "DLP Getting Started | DLP Products | TI.com." [Online]. Available: http://www.ti.com/dlp-chip/getting-started.html. [Accessed: 12-Nov-2018].
[100] R. Y. Nielson, "Nonlinear laser microfabrication in biological environments," Thesis, 2007.
[101] A. León Robles, E. Acedo Félix, B. Gomez-Gil, E. I. Quiñones Ramírez, M. Nevárez-Martínez, and L. Noriega-Orozco, "Relationship of aquatic environmental factors with the abundance of Vibrio cholerae, Vibrio parahaemolyticus, Vibrio mimicus and Vibrio vulnificus in the coastal area of Guaymas, Sonora, Mexico," *J. Water Health*, vol. 11, no. 4, pp. 700–712, Dec. 2013.
[102] T. Miyashiro and E. G. Ruby, "Shedding light on bioluminescence regulation in Vibrio fischeri: Shedding light on bioluminescence regulation in Vibrio fischeri," *Mol. Microbiol.*, vol. 84, no. 5, pp. 795–806, Jun. 2012.
[103] S. Scheerer, F. Gomez, and D. Lloyd, "Bioluminescence of Vibrio fischeri in continuous culture: Optimal conditions for stability and intensity of photoemission," *J. Microbiol. Methods*, vol. 67, no. 2, pp. 321–329, Nov. 2006.
[104] H. Urbanczyk, J. C. Ast, M. J. Higgins, J. Carson, and P. V. Dunlap, "Reclassification of Vibrio fischeri, Vibrio logei, Vibrio salmonicida and Vibrio wodanis as Aliivibrio fischeri gen. nov., comb. nov., Aliivibrio logei comb. nov., Aliivibrio salmonicida comb. nov. and Aliivibrio wodanis comb. nov.," *Int. J. Syst. Evol. Microbiol.*, vol. 57, no. 12, pp. 2823–2829, 2007.
[105] "Impact of Salt and Nutrient Content on Biofilm Formation by Vibrio fischeri." [Online]. Available:

https://journals.plos.org/plosone/article?id=10.1371/journal.pone.0169521. [Accessed: 12-Nov-2018].
[106] L. Li, C. Kato, and K. Horikoshi, “Bacterial diversity in deep-sea sediments from di erent depths,” p. 19.
[107] J. D. Wang and P. A. Levin, “Metabolism, cell growth and the bacterial cell cycle,” *Nat. Rev. Microbiol.*, vol. 7, no. 11, pp. 822–827, Nov. 2009.
[108] P. D. Schloss and J. Handelsman, “Status of the Microbial Census,” *Microbiol. Mol. Biol. Rev.*, vol. 68, no. 4, pp. 686–691, Dec. 2004.
[109] T. J. Hoppe, “Laser-based techniques for manipulating the single-cell environment,” Thesis, 2013.
[110] D. S. Hernandez, E. T. Ritschdorff, S. K. Seidlits, C. E. Schmidt, and J. B. Shear, “Functionalizing micro-3D-printed protein hydrogels for cell adhesion and patterning,” *J. Mater. Chem. B*, vol. 4, no. 10, pp. 1818–1826, 2016.
[111] T. Nakae, “Outer-membrane permeability of bacteria,” *Crit. Rev. Microbiol.*, vol. 13, no. 1, pp. 1–62, 1986.
[112] R. Yin and M. R. Hamblin, “Antimicrobial Photosensitizers: Drug Discovery Under the Spotlight,” *Curr. Med. Chem.*, vol. 22, no. 18, pp. 2159–2185, 2015.
[113] “Amine-Reactive Probe Labeling Protocol - US.” [Online]. Available: https://www.thermofisher.com/us/en/home/references/protocols/cell-and-tissue-analysis/labeling-chemistry-protocols/amine-reactive-probe-labeling-protocol.html. [Accessed: 09-Nov-2018].
[114] Q. Shi, Y. Zhou, and Y. Sun, “Influence of pH and Ionic Strength on the Steric Mass-Action Model Parameters around the Isoelectric Point of Protein,” *Biotechnol. Prog.*, vol. 21, no. 2, pp. 516–523, Sep. 2008.
[115] D. I. Hitchcock, “THE ISOELECTRIC POINT OF A STANDARD GELATIN PREPARATION,” *J. Gen. Physiol.*, vol. 14, no. 6, pp. 685–699, Jul. 1931.
[116] B. Kaehr and J. B. Shear, “Multiphoton fabrication of chemically responsive protein hydrogels for microactuation,” *Proc. Natl. Acad. Sci.*, vol. 105, no. 26, pp. 8850–8854, Jul. 2008.
[117] M. Ali, “Dynamic micro-3D-printed substrates for characterizing cellular responses to topography,” Thesis, 2014.
[118] J. L. Connell, “Characterization and microfabrication of environmentally sensitive materials for studying bacterial group behaviors,” Aug. 2012.
[119] K. H. Turner, A. K. Wessel, G. C. Palmer, J. L. Murray, and M. Whiteley, “Essential genome of Pseudomonas aeruginosa in cystic fibrosis sputum,” *Proc. Natl. Acad. Sci. U. S. A.*, vol. 112, no. 13, pp. 4110–4115, Mar. 2015.
[120] K. L. Palmer, L. M. Aye, and M. Whiteley, “Nutritional cues control Pseudomonas aeruginosa multicellular behavior in cystic fibrosis sputum,” *J. Bacteriol.*, vol. 189, no. 22, pp. 8079–8087, Nov. 2007.
[121] L. E. P. Dietrich, A. Price-Whelan, A. Petersen, M. Whiteley, and D. K. Newman, “The phenazine pyocyanin is a terminal signalling factor in the quorum sensing network of Pseudomonas aeruginosa,” *Mol. Microbiol.*, vol. 61, no. 5, pp. 1308–1321, Sep. 2006.

[122] Simoska, Olja; Sans, Marta; Fitzpatrick, Mignon; Crittenden, Christopher; Eberlin, Livia; Schear, Jason; Stevenson, Keith, "Real-time Electrochemical Detection of <i>Pseudomonas aeruginosa<i> Phenazine Metabolites using Transparent Carbon Ultramicroelectrode Arrays," *ACS Sensors*, Oct. 2018.
[123] "Accuracy of Spectrophotometer Readings." [Online]. Available: http://www5.csudh.edu/oliver/che230/labmanual/accucolo.htm. [Accessed: 12-Nov-2018].
[124] B. G. Hall, H. Acar, A. Nandipati, and M. Barlow, "Growth Rates Made Easy," *Mol. Biol. Evol.*, vol. 31, no. 1, pp. 232–238, Jan. 2014.
[125] "The Limitations of LB Medium," *Small Things Considered*. [Online]. Available: https://schaechter.asmblog.org/schaechter/2009/11/the-limitations-of-lb-medium.html. [Accessed: 12-Nov-2018].
[126] J. R. Yates III, "A century of mass spectrometry: from atoms to proteomes," *Nat. Methods*, vol. 8, no. 8, pp. 633–637, Aug. 2011.
[127] E. R. Amstalden van Hove, D. F. Smith, and R. M. A. Heeren, "A concise review of mass spectrometry imaging," *J. Chromatogr. A*, vol. 1217, no. 25, pp. 3946–3954, Jun. 2010.
[128] J. M. Wiseman, D. R. Ifa, A. Venter, and R. G. Cooks, "Ambient molecular imaging by desorption electrospray ionization mass spectrometry," *Nat. Protoc.*, vol. 3, no. 3, pp. 517–524, 2008.
[129] Q. Zheng and H. Chen, "Development and Applications of Liquid Sample Desorption Electrospray Ionization Mass Spectrometry," *Annu. Rev. Anal. Chem.*, vol. 9, no. 1, pp. 411–448, 2016.
[130] J. Tillner *et al.*, "Faster, More Reproducible DESI-MS for Biological Tissue Imaging," *J. Am. Soc. Mass Spectrom.*, vol. 28, no. 10, pp. 2090–2098, 2017.
[131] E. J. Lanni *et al.*, "MALDI-guided SIMS: Multiscale Imaging of Metabolites in Bacterial Biofilms," *Anal. Chem.*, vol. 86, no. 18, pp. 9139–9145, Sep. 2014.
[132] S. Häussler and T. Becker, "The Pseudomonas Quinolone Signal (PQS) Balances Life and Death in Pseudomonas aeruginosa Populations," *PLOS Pathog.*, vol. 4, no. 9, p. e1000166, Sep. 2008.
[133] J. Lin, J. Cheng, Y. Wang, and X. Shen, "The Pseudomonas Quinolone Signal (PQS): Not Just for Quorum Sensing Anymore," *Front. Cell. Infect. Microbiol.*, vol. 8, 2018.
[134] J. M. A. Blair, M. A. Webber, A. J. Baylay, D. O. Ogbolu, and L. J. V. Piddock, "Molecular mechanisms of antibiotic resistance," *Nat. Rev. Microbiol.*, vol. 13, no. 1, pp. 42–51, Jan. 2015.
[135] A. A. Bahar and D. Ren, "Antimicrobial peptides," *Pharm. Basel Switz.*, vol. 6, no. 12, pp. 1543–1575, Nov. 2013.
[136] D. Gaspar, A. S. Veiga, and M. A. R. B. Castanho, "From antimicrobial to anticancer peptides. A review," *Front. Microbiol.*, vol. 4, p. 294, Oct. 2013.
[137] R. E. Hancock, "Cationic peptides: effectors in innate immunity and novel antimicrobials," *Lancet Infect. Dis.*, vol. 1, no. 3, pp. 156–164, Oct. 2001.

[138] N. Asthana, S. P. Yadav, and J. K. Ghosh, “Dissection of Antibacterial and Toxic Activity of Melittin A LEUCINE ZIPPER MOTIF PLAYS A CRUCIAL ROLE IN DETERMINING ITS HEMOLYTIC ACTIVITY BUT NOT ANTIBACTERIAL ACTIVITY,” *J. Biol. Chem.*, vol. 279, no. 53, pp. 55042–55050, Dec. 2004.
[139] J. H. CHOI *et al.*, “Melittin, a honeybee venom-derived antimicrobial peptide, may target methicillin-resistant Staphylococcus aureus,” *Mol. Med. Rep.*, vol. 12, no. 5, pp. 6483–6490, Nov. 2015.
[140] H. Sasaki and S. H. White, “Aggregation Behavior of an Ultra-Pure Lipopolysaccharide that Stimulates TLR-4 Receptors,” *Biophys. J.*, vol. 95, no. 2, pp. 986–993, Jul. 2008.
[141] C. R. H. Raetz *et al.*, “Kdo2-Lipid A of Escherichia coli, a defined endotoxin that activates macrophages via TLR-4,” *J. Lipid Res.*, vol. 47, no. 5, pp. 1097–1111, May 2006.